

Sol-Gel Derived Tantalum Oxide

Thin Films

by

Lee Arnold Silverman

Submitted to the Department of  
Materials Science and Engineering  
in partial fulfillment of the requirements  
for the degree of

Doctor of Philosophy

at the

Massachusetts Institute of Technology

June, 1987

© Massachusetts Institute of Technology

Signature of Author \_\_\_\_\_

Department of Materials Science and Engineering  
May 1, 1987

Certified by \_\_\_\_\_

Donald R. Uhlmann  
Cabot Professor of Materials  
Thesis Supervisor

Accepted by \_\_\_\_\_

Samuel M. Allen  
Chairman, Departmental Committee on Graduate Students

MASSACHUSETTS INSTITUTE  
OF TECHNOLOGY

Archives JUN 22 1987

LIBRARIES

## Sol-Gel Derived Tantalum Oxide Thin Films

by

Lee Arnold Silverman

Submitted to the Department of Materials Science and Engineering on May 1, 1987, in partial fulfillment of the requirements for the degree of Doctor of Philosophy.

### ABSTRACT

The formation of thin tantalum oxide films using the sol-gel method was investigated. These films were evaluated for their potential use as a dielectric layer for very large scale integrated circuit (VLSI) applications. The dielectric constant was measured to be 30, with a loss factor of 0.032 at 1 megahertz for films fired at 800 C. The leakage current was also measured, and was found to be slightly higher than that reported for tantalum oxide made by other processes.

The solution chemistry of the precursors was examined, and the Flory Gelation Model was applied to tantalum ethoxide. Using this information combined with NMR results, the structure of the species in the coating solution was elucidated.

The spin coating behavior of these solutions was studied, and they were found to obey many of the same rules as the more widely known polymeric photoresists. It was also observed, however, that coating must be carried out in a dry environment to prevent precipitation of particles.

The films were studied using transmission electron microscopy. They were found to be uniform in texture, containing no macroscopic porosity before or after firing. The densification behavior of both the films and of pellets formed from powders was studied and compared. It was found that films and precipitated powders are appreciably different in terms of their porosity before firing.

Thermal analysis, including differential thermal analysis, thermogravimetric analysis, and fourier transform infrared spectroscopy were used to elucidate processes that occur in powders during densification. Tantalum oxide powders containing up to 50% of another cation were compared and found to behave similarly to those that were undoped.

Thesis supervisor: D.R. Uhlmann

Title: Cabot Professor of Materials

## Acknowledgements

First and foremost, I thank my advisor, Prof. D.R. Uhlmann, for his support and creativity throughout this work. In addition, Prof. G.E. Wnek was invaluable for getting me to see that understanding the chemistry behind the solution parts of sol-gel processing may, in large part, determine the usefulness of what comes out of the process. I also thank Prof. H. Tuller, with whom I had many fruitful discussions, and who also allowed me to use his equipment for electronic characterization of my materials.

My gratitude goes to the Air Force Office of Scientific Research and to the International Partners in Glass Research for funding this project. I thank the International Business Machine Corporation for supplying some of the silicon substrates used in this study.

I must also thank a host of fellow graduate students. The members of the Prof. Uhlmann's Sol-Gel group are first on the list because of both the technical and social interactions that we had. Among these are Brian Zelinski, Carol Parkhurst, Brian Fabes, Sachi Singh, Bill Doyle and Michele Andersen. I also must thank Gimtong Teowee, who first directed me through the semiconductor processing part of this work, and Peter Moon and Gyeong-Man Choi, not only for the amazing programming job done on their equipment for their own applications, but also their help with some of my own programming applications. I must acknowledge the help of Gary Ditmer, without whom the semiconductor processing facilities would have been incomprehensible.

For her help with the administrative aspects of my MIT career, my heartfelt thanks must go to Linda Sayegh. She brought much needed organization into the MIT bureaucratic maze.

I thank my friends at Corning Glass Works, from where I have been on educational leave of absence for the past three and a half years. My experience there taught me much about industry and myself, and helped me see that I needed to go back to school.

I thank my parents and brothers for being there and providing me with the self-confidence and attitude of perseverance that makes long term commitments such as this feasible.

Last and perhaps most importantly, I would like to thank my wife and best friend, Gail St. Amand. Without her encouragement, support, and honesty, the trial-by-fire that is MIT would not have been possible, let alone enjoyable. Mere words are not enough, but will have to suffice.

Thank you all.

## Table of Contents

Title page	1
Abstract	2
Acknowledgements	3
List of tables	5
List of figures	6
Chapter 1: Introduction	9
Chapter 2: Literature Survey	
2.1: Tantalum oxide	12
2.2. Chemical processing	20
2.3. Drying gels	41
2.4. Densification of gels	48
2.5. Electronic characterization	50
2.6. Gel-derived tantala	53
Chapter 3. Experimental Procedure	58
Chapter 4. Results and Discussion	
4.1. Coating solutions	72
4.2. Coating application	95
4.3. Densification of films	114
4.4. Electronic characterization	126
4.5. Chemical passivation	143
4.6. Powder characterization	144
4.7. Sintering of pellets	167
Chapter 5. Conclusions	179
Chapter 6. Future Work	181
References	183
Biographical Data	186

## List of Tables

Table	Description	Page
2.1.1	Literature values for the refractive index of tantala for several formation conditions	13
2.1.2	Literature values for the dielectric consants of several forms of tantala	17
2.2.1	Boiling and melting points for several tantalum alkoxides	21
2.2.2	Molecular complexities of normal tantalum alkoxides in various solvents	26
2.2.3	Molecular complexities of several tantalum alkoxides at various degrees of hydrolysis	36
3.1	RCA cleaning procedure	60
3.2	Typical recipe for tantalum oxide ethoxide coating solution	61
3.3	Pan etch formulation	67
4.1.1	Hydrolysis simulation results for varying degrees of hydrolysis	79
4.1.2	Condensation simulation results for the addition of the ethoxide to water	81
4.1.3	Condensation simulation results for the addition of the water to ethoxide	90
4.2.1	Thickness of undensified coatings as a function of spin speed	104
4.2.2	Thickness of undensified coatings as a function of oligomer concentration in coating solution	104
4.6.1	DTA crystallization exotherm temperatures	156
4.6.2	TGA data on weight loss and the temperatures at which they occur	158

## List of Figures

Fig.	Description	Page
2.1.1	Structure of beta tantala	15
2.1.2a	Phase diagram - tantala-magnesia	16
2.1.2b	Phase diagram - tantala-zirconia	16
2.1.2c	Phase diagram - tantala-alumina	16
2.1.2d	Phase diagram - tantala-titania	16
2.2.1	Structure of magnesium ethoxide	24
2.2.2	Structure of titanium ethoxide	24
2.2.3	Structure of tantalum ethoxide dimer	25
2.2.4	Structure of tantalum ethoxide monomer	25
2.2.5	Structure of activated tantalum ethoxide complex	29
2.2.6	Structure of tantalum diethoxide triacetylacetonate	31
2.2.7	Billinear chain model for tantalum oxide ethoxide	37
2.3.1	Pore model for drying stresses	43
2.3.2	Model of sandwich seal	47
2.5.1	Energy band representations of bias conditions for MOS capacitors	52
2.6.1	TGA results on sol-derived tantala	56
3.1	Schematic of spin-coating apparatus	64
3.2	Schematic of section of gate electrode pattern	66
3.3	Schematic of transmission electron microscope sample	69
3.4	Schematic of effluent gas analysis system using the FTIR	71
4.1.1	Methylene portion of NMR spectrum of tantalum ethoxide at 235 K	73
4.1.2	Structure of titanium diethoxide diacetylacetonate	76
4.1.3	Simulation of development of species during the hydrolysis of tantalum ethoxide	78
4.1.4	Simulation of polymerization - development of weight average degree of polymerization for the addition of the ethoxide to water	82
4.1.5	Simulation of polymerization - development of number average degree of polymerization for the addition of the ethoxide to water	83
4.1.6	Development of number average degree of polymerization for the polyesterification of succinic acid and tricarballylic acid	85
4.1.7	Simulation of polymerization - molecular weight distribution resulting from the addition of the ethoxide to water	86
4.1.8	Simulation of polymerization - development of weight average degree of polymerization for the addition of the water to the ethoxide	87
4.1.9	Simulation of polymerization - development of number average degree of polymerization for the addition of the water to the ethoxide	88
4.1.10	Simulation of polymerization - molecular weight distribution resulting from the addition of the water to the ethoxide	89

## List of Figures (cont.)

Fig.	Description	Page
4.1.11	Simulation of polymerization - number and weight average degrees of polymerization resulting from simulations compared with predictions of Flory's model	91
4.1.12	Methylene portion of NMR spectrum of tantalum oxide ethoxide at 204 K	94
4.2.1	TEM micrograph of film on carbon substrate dried in dry atmosphere	97
4.2.2	TEM micrograph of film on carbon substrate dried in humid atmosphere	98
4.2.3	Schematic of the development of uniform and precipitate-containing films	100
4.2.4a	Thickness of undensified films as function of substrate spin speed	101
4.2.4b	Thickness of undensified films as function of square root of the reciprocal spin speed	102
4.2.5	Thickness of undensified films as function of oligomer concentration of the coating solution	103
4.2.6	STEM micrograph of shadowed replica of pinhole	105
4.2.7	Thickness of undensified films as function of the number of layers when applied in a slightly humid atmosphere	107
4.2.8	Thickness of undensified films as function of the number of layers when applied in a very dry atmosphere	108
4.3.1	Thickness of densified films as function of firing time	115
4.3.2	Thickness of densified films as function of firing temperature	116
4.3.3	Index of refraction of densified films as function of firing temperature	118
4.3.4	TEM micrograph of film on silicon substrate fired for 1 hour at 1000 C	120
4.3.5	TEM micrograph of ion milled undensified film on silicon substrate	121
4.3.6	Electron diffraction patterns from films on silicon substrates fired for 1 hour at 600 and 700 C	122
4.3.7	Reflection high energy electron diffraction patterns from films on silicon substrates fired for 1 hour at 600 and 700 C	124
4.3.8	TEM micrograph of film on carbon substrate fired for 1 hour at 800 C	125
4.3.9	Schematic of microstructure formation during the firing of films for varying degrees of adhesion to substrate	127
4.4.1	Dielectric constant of densified films as function of firing temperature	129
4.4.2	Frequency dependence of loss coefficient	130
4.4.3	Measured capacitance of densified films as function of firing temperature	131
4.4.4	Model of measured capacitance as function of degree of densification	134
4.4.5	Fraction of MIS devices that broke down as function of firing temperature	136

## List of Figures (cont.)

Fig.	Description	Page
4.4.6	Capacitance as function of bias voltage exhibiting breakdown	137
4.4.7	Leakage current as function of bias voltage exhibiting breakdown	138
4.4.8	Leakage current as function of bias voltage not exhibiting breakdown	139
4.4.9	Normalized dielectric constant as function of firing temperature for doped and undoped films	141
4.4.10	Measured capacitance as function of firing temperature for titania and zirconia containing films	142
4.6.1	SEM micrograph of unfired powder	145
4.6.2	TGA scan in oxygen of undoped films	147
4.6.3	DTA scans in oxygen and nitrogen of undoped films	147
4.6.4	Absorption of C-H stretch in effluent gases as function of sample firing temperature	148
4.6.5	Absorption of H <sub>2</sub> O in effluent gases as function of sample firing temperature	149
4.6.6	Absorption plot of effluent gases for sample temperature of 200 C	150
4.6.7	Absorption plot of effluent gases for sample temperature of 300 C	151
4.6.8	Absorption of CO <sub>2</sub> in effluent gases as function of firing temperature	153
4.6.9	X-ray diffraction patterns of powders of various compositions and firing conditions	155
4.6.10	DTA crystallization exotherms for powders of various composition	157
4.6.11	Model of diffusion controlled reaction in spherical particle	161
4.6.12	Model of amount of reaction product in effluent gas based on diffusion controlled reaction in spherical particle	162
4.6.13	Correlation of DTA crystallization exotherm temperatures and TGA high temperature weight loss	164
4.7.1	Densification behavior of pressed pellet	169
4.7.2	SEM micrograph of fracture surface of pellet fired to 1000 C	170



## Chapter 1. Introduction

The production of high value added specialty ceramics from gels using a solution chemistry approach has recently come into vogue in the materials science community. The reasons for this are as varied as the applications themselves, but center around several basic notions. This approach has the capability of producing ceramics of high chemical homogeneity. The gels are generally considered to be made up of exceedingly small particles. Due to the large surface to volume ratio and other considerations, gel-derived ceramics can be produced at relatively low processing temperatures. Finally, compositions with microstructures never before synthesized can be produced with this low temperature method.

This is not to say that the production of materials from gels is without its problems. Chemical inhomogeneity may result from poor selection of precursor materials and/or reaction conditions. The formation of monolithic pieces is made difficult by stresses that arise during the drying of gels. These are only two in a host of problems that can occur during the production of ceramics from gels.

With these problems in mind, most of the work done here was on a single component system. This course was intentionally followed to bypass the issue of chemical homogeneity of the gels. In addition, most of this work centered on the thin film geometry specifically to eliminate the complication of monolith formation mentioned above. Finally, the system selected has precursors with a relatively simple solution behavior so as to eliminate certain complications that can and

do arise during the initial stages of processing.

Sol-gel derived tantalum oxide was brought to our attention in a poster session at the fall MRS meeting of 1984 [1]. Data presented that tantalum thin film gels were relatively dense without a high temperature densification step. This was contrary to the current wisdom about gel structures, and therefore became a point of interest.

In addition, tantalum oxide has long been known as an excellent dielectric material, and gained much popularity in the 1950's as a capacitor dielectric. This is primarily due to the ease of fabrication of the oxide by anodization of tantalum metal in an acidic medium. The resulting oxide is amorphous and has a dielectric constant greater than 20. More recently, tantalum has been used as a dielectric by depositing thin films onto a variety of substrate materials, the most popular being silicon. The justification for these last works is straightforward. If tantalum oxide can replace silica as the dielectric layer in very large scale integrated circuits (VLSI), the roughly eightfold increase in dielectric constant will lead to a corresponding decrease in the area of the metal-insulator-silicon (MIS) capacitor elements. This means an increase in the number of these circuits that can be placed in a given area.

The combination of these two ideas - that a high dielectric constant material could be produced without an extended high temperature processing step using a sol-gel approach captured our collective imaginations. The work that is presented herein is directed at describing the processes that occur during the formation of tantalum oxide from gels made by solution processing of alkoxide precursors. The oxide films and powders were then characterized in terms of their

densification and crystallization behaviors, and their optical and electronic properties.

## Chapter 2. Literature Survey

The primary reason for this work is to investigate whether gel-derived tantala is a good material for a dielectric layer in VLSI devices. In order to understand the way the dielectric constant develops, we must understand all of the processes leading up to the point where the dielectric constant is measured. Because it is possible for any process prior to the dielectric constant measurement to effect the value that is measured, some attention must be paid to the solution phase of the process in addition to the solid state processes. With this in mind, the following discussion will go into some detail for most of the process that may occur during the production of dense tantala films using a gel process.

### 2.1. Tantalum Oxide

Tantalum oxide exists in two crystal structures, alpha and beta, corresponding to low and high temperature phases respectively. The transformation between these phases takes place sluggishly at 1360 C, and the high temperature phase is reported to melt at 1887 C. For amorphous tantala, the glass transition temperature is quoted as 1400 K [2], but this value may have been calculated as two thirds of the melting point.

The refractive index of tantala has been reported over a fairly wide range. Many literature values are presented, ranging from 1.96 to 2.42 with the average being just above 2.2 (Table 2.1.1). This is true

for the crystalline and amorphous phases regardless of preparation conditions, with no appreciable change in refractive index noted during crystallization. The imaginary part of the refractive index for the amorphous phase is generally assumed to be zero [3]. A value of the imaginary part for crystalline tantala deposited by the pyrolysis of tantalum dichloride diethoxide acetylacetonate has been given as between 0 and -0.044i. The Cauchy formula for the refractive index is

$$n = 2.033 + \frac{8.74 \times 10^6}{\lambda^2} \quad (2.1.1)$$

If this calculation is performed for the helium-neon laser ( $\lambda = 632 \text{ nm}$ ), the resulting value is 2.25.

Table 2.1.1.

Literature values for the refractive index at 632 nm  
for several formation conditions.

n	k'	material	reference
2.21		amor. - plasma oxidation	3
2.42		amor. - anodized	4
1.96		amor. - CVD of halide-organic, 300 C	5
2.31		amor. - CVD of halide-organic, 500 C	5
2.20	0-.044i	cryst. - CVD from halide, 900 C	6
2.25		calculated from Cauchy formula	7,8

Tantalum oxide is chemically very stable. It is attacked by only one acid - hydrofluoric, and is reduced to the metal only by molten aluminum or calcium, or intimately mixed graphite [9]. It is attacked by concentrated metal fluorides and hydroxides, hydrogen peroxide, and a few chlorides at elevated temperatures. It is therefore attractive as a passivating layer for less durable substrates.

The crystal structure of the low temperature phase was described by Stephenson and Roth [10], and is composed of long strings of edge and

corner sharing distorted octahedra and pentagonal bipyramids (fig. 2.1.1). The regularity of the unit cell is interrupted by defect planes, which serve as places where oxygen sites are only partially occupied so as to maintain the stoichiometry of the overall structure. The density of defect planes in the crystal is a function of both the thermal history and the amount and types of impurities in the sample.

The crystal structure is very different from that of most other oxide ceramics except niobium oxide. This limits its solubility in other oxides and vice versa. The phase diagrams of binary systems of tantalum and magnesia, titania, zirconia, alumina (fig. 2.1.2) [11], as well as many other oxides show very little solid solubility in the low temperature phase. The notable exception to this is lithia, which has been dissolved in beta tantalum up to 5%. Lithia stabilizes the low temperature form to its melting point of greater than 1800 C, completely bypassing the beta to alpha phase transformation. In systems other than this, the addition of small amounts of a second oxide generally results in the formation of an intermediate tantalate compound. For example, minute amounts of titania will precipitate out of the solution as a titanium tantalate. The phase diagrams indicate that for small additions of the second component, the specific phase that will precipitate may differ in its tantalum to second-cation ratio. The dotted lines in the phase diagrams represent phases that are derivatives of the beta tantalum phase, and can be characterized as having a beta tantalum superstructure. They are distinguished by measuring the intensity of a specific line in their diffraction patterns. The high temperature phase has been shown to dissolve readily additions of magnesia and scandia. These dopants serve to stabilize the alpha phases

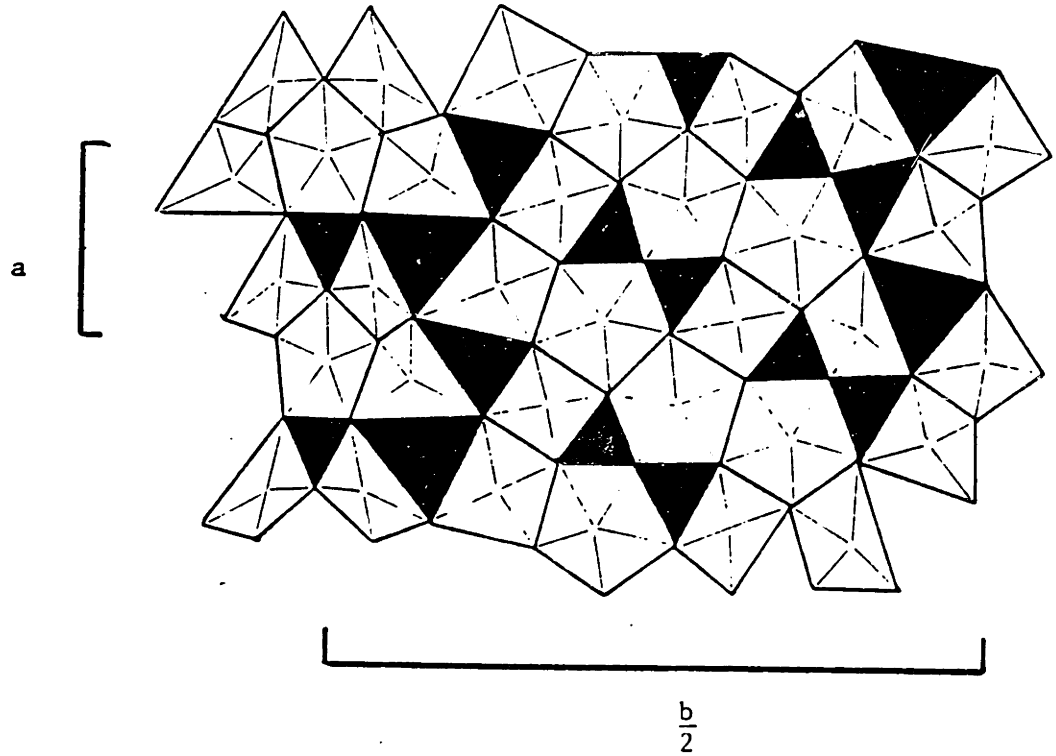


Figure 2.1.1  
Structure of one half of the unit cell of beta tantalum  
showing the edge-sharing polyhedra. Light lines indicate  
the edges of the polyhedra faces above the plane of the paper.  
Dimensions a and b show the size of the unit cell (after [10]).

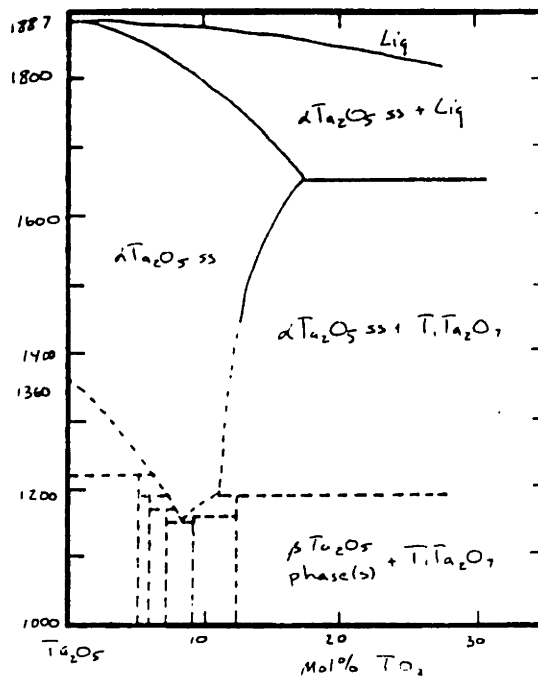
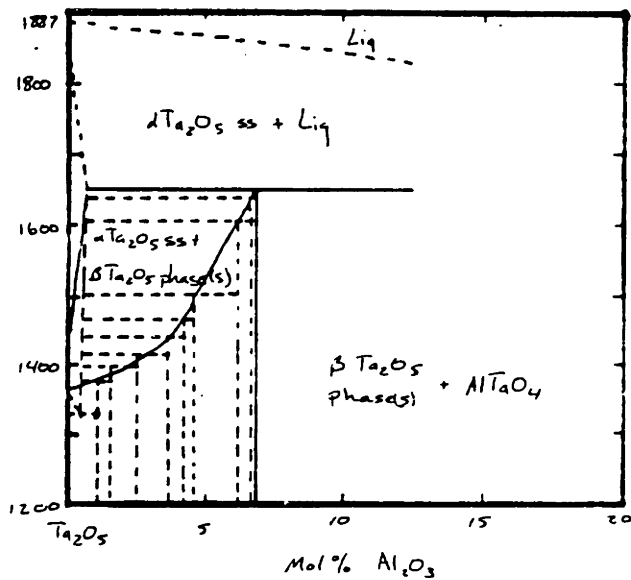
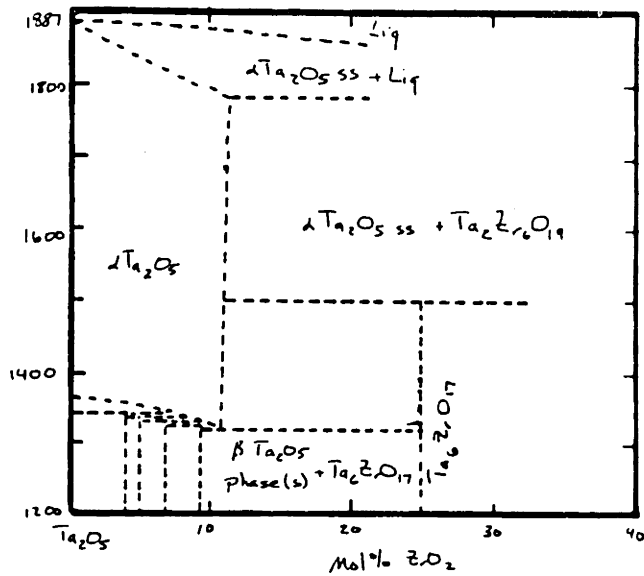
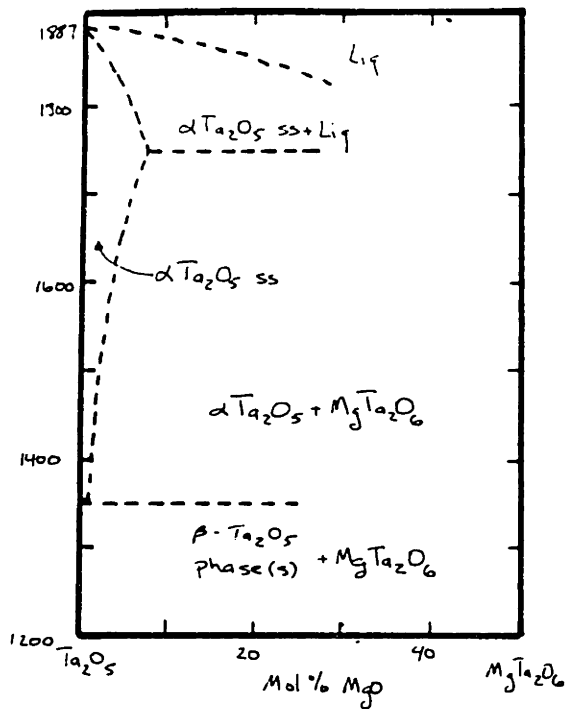


Figure 2.1.2  
Binary phase diagrams for tantalum rich regions of tantalum and (a) magnesia, (b) zirconia (c) alumina, and (d) titania (after [11]).



against the alpha to beta transformation that usually occurs upon cooling the sample [12,13]. This has technological importance because this transition usually results in the disintegration of the sample.

The structures of both phases of tantalum are responsible for giving it some interesting properties. The high ionic mobilities give the material utility as a solid oxygen electrolyte at elevated temperatures because of channels that exist between the coordination polyhedra [12,13]. In addition, the 7-fold coordination around some of the tantalum ions is greater than the 6-fold coordination predicted by Pauling's Rules. This increase in coordination number defines a space larger than is occupied by the ion, enabling vibration of the heavy pentavalent ion within the allocated space. This gives rise to a dielectric constant of between 20 and 30, with a value of 44 also reported (table 2.1.2). As with the refractive index data, there are many values, each corresponding to different conditions of formation and crystallinity. The loss tangent of crystalline tantalum has been reported to be less than .01 [14].

Table 2.1.2.

Literature values of the relative dielectric constant of amorphous and beta tantalum.

k'	phase	reference
25	amorphous	15
25	amorphous	16
21.7	amorphous	17
22	amorphous	18
24.1 ;	beta	19
22-30	beta	20
44	beta	6

The combination of these two properties, a high mobility of oxygen

with a high dielectric constant, has made tantalum oxide a commercially useful material. It is quite commonly used as a dielectric in precision capacitors, and is easily formed by the anodization of tantalum metal in an acidic medium.

The anodization process is responsible for the oxidation of the metal, and in most cases produces an amorphous coating that is quite uniform in thickness. The rate limiting step during anodization is the diffusion of oxygen through the oxide to the oxide/metal interface [12]. The thickness of the anodized layer follows a square root dependence on time at long times, indicative of diffusion being the limiting step [8]. The reason that uniform layers are grown is that if there is a spot on the film which happens to grow thicker than the surrounding material, the diffusion in this region will slow due to the increase in the length of the diffusion path. Therefore growth in this area will slow compared to that in the surrounding region. As might be expected in a process such as this, the resulting film has a gradient in the oxygen/tantalum ratio making the film a p-type semiconductor at the solution/oxide interface, and an n-type semiconductor at the metal/oxide interface [21]. The central part of the film is insulating.

In addition to the anodization process not requiring high temperatures, a further reason for its popularity is that it is reported to be 98% efficient in terms of the current passed resulting in oxide grown [22]. Another positive point is that the oxide formed in this manner is dense without any high temperature sintering steps. The end result is a dense oxide film whose thickness is precisely controllable by the amount of current passed through the anodization bath. This makes the production of precision capacitors fairly easy.

Annealing of the anodized films causes some structural changes, and has been shown to decrease the rate at which the amorphous film will etch in hydrofluoric acid [23]. When an annealed film is reanodized, the etch rate of the annealed material has been shown to increase back to its initial, as-anodized value. Anodized films have been shown to crystallize at temperatures below 800 C [5,18]. Reactively sputtered films have been shown to densify at 600 C, where shrinkage led to pinhole formation in films on silicon nitride substrates [24]. These films were shown to crystallize between 650 and 700 C.

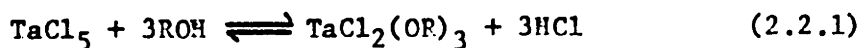
Another way to make tantalum is to expose tantalum metal to an oxidizing atmosphere at an elevated temperature. If the temperature is below 300 C, the oxide produced is amorphous and adheres well to the metal, forming a protective coating [25]. The thickness will continue to increase as long as the growing conditions are maintained. Above 400 C, the oxide produced is crystalline and tends to spall, leaving the metal unprotected [26].

This method, called thermal oxidation, has been reported to have been used on sputtered tantalum metal layers to generate MIS capacitors on silicon for the evaluation of the insulator as a dielectric in VLSI devices [16,20,27]. Other methods used to form these structures include chemical vapor deposition from organometallic and metal alkoxide species [5], and reactive sputtering of tantalum metal in a slightly oxidizing atmosphere [24]. Conductivity and dielectric data from all of these processes indicated that the leakage current is low and the dielectric constant is high. In addition, the dielectric loss factor has been reported to be less than .01 [14]. This makes the material attractive as a potential VLSI dielectric layer.

## 2.2. Chemical Processing

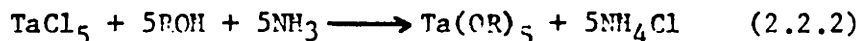
The bulk of this work concerns the production and characterization of tantalum oxide films from a sol-gel route. Since many properties of gel-derived products are dependent on the chemical and thermal histories of the gels, much must be understood about the processes that can occur, starting at from the synthesis of the alkoxides and continuing through to the densification and crystallization of the resulting amorphous films.

Tantalum alkoxides, like those of many other metals, are formed by the action of alcohol on the metal chloride [28,29]. As in most cases, great care must be taken to insure that the system is scrupulously dry, including the glassware and the reagents. Anhydrous tantalum chloride is slowly added to anhydrous alcohol while stirring. During the reaction, hydrogen chloride gas is liberated in copious amounts. The reaction, however, does not go to completion under these conditions, as only an average of three of the five original chloride groups are reacted. This forms the dichloride trialkoxide.



In order to drive the reaction to completion, the solution is subsequently saturated with anhydrous ammonia. This reacts with the HCl dissolved in solution producing ammonium chloride. The ammonium salt precipitates out of solution due to its low solubility in alcohol, thus shifting the equilibrium of the alkoxide formation reaction toward the products. Upon completion the salt is removed by filtering the solution

through a dry fritted glass disk. The entire reaction may be simplistically written out as



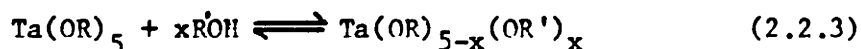
If further purification is necessary, many of the tantalum alkoxides are volatile and may be distilled. Most are colorless, mobile liquids at room temperature, and dissolve readily in their parent alcohols. The melting and boiling points of several tantalum alkoxides are presented in table 2.2.1.

Table 2.2.1.

Boiling and melting points for several alkoxides of tantalum after references 29 and 30.

R in Ta(OR) <sub>5</sub>	Boiling Point (C)	Melting Point (C)
Me	130 @ 0.2mm	50
Et	147 "	
Pr <sup>n</sup>	184 "	
Bu <sup>n</sup>	217 "	
	242 @ 5.5 mm	
Me <sub>2</sub> CH CH <sub>2</sub>	210 "	
Me CH <sub>2</sub> CH Me	156 "	157
Me <sub>3</sub> C	149.5 "	110

Another feature common to alkoxides of many metals is that they readily undergo alcohol exchange reactions [31]. For example, if tantalum methoxide is put into propanol, the methoxy groups will exchange with the alcohol solvent. This generally produces a mixed alkoxide



This reaction, as does the synthesis reaction, reaches an equilibrium after a fraction of the exchangeable alkoxy groups have reacted [29]. The number of groups exchanged is a function of the alkoxide and alcohol

used, as well as their concentrations. These mixed alkoxides are frequently separable by distillation, allowing a pure tantalum monomethoxide tetrabutoxide to be isolated, for example. The alcohol exchange reaction is useful in the synthesis of higher and branched alkoxides of tantalum. Most frequently this is accomplished by adding tantalum methoxide to a higher alcohol and bringing the solution to a temperature above the boiling point of methanol. Methanol will preferentially concentrate in the vapor, and therefore can be removed by distillation. This causes the concentration of the lower boiling alcohol in the refluxing vessel to be reduced, driving the reaction toward the completely exchanged alkoxide.

An additional feature of tantalum alkoxides that is common to alkoxides of many other metals is their tendency to form complexes with available nucleophiles [28,30,32,33,34]. Complexation is the term used to describe the situation when an atom attains a coordination number that is greater than the number of covalent bonds that it can form. It arises from interactions of the electrically charged dipoles formed by the polarized metal-oxygen bond. For example, magnesium can chemically bond to two alkoxy groups, each one having a negative 1 charge. However, magnesium prefers to be coordinated by 4 oxygens in solution. In the absence of a solvent, the alkoxide complexes with itself, forming long "polymeric" chains as depicted in fig. 2.2.1 [34]. The relatively highly polar Mg-O bond favors these complexed structures over the solvated molecules. The result is that magnesium ethoxide, and indeed most other unbranched alkaline earth alkoxides, is insoluble in its parent alcohol.

A similar situation occurs with aluminum, titanium and zirconium

alkoxides, but to a lesser extent [34]. These alkoxides form complexes with themselves that involve up to four alkoxide molecules. Aluminum is trivalent but prefers to be sixfold coordinated. The isopropoxide has been characterized as being trimeric upon quenching the distilled liquid. However, upon waiting for a period up to several days (depending on the temperature) the trimers slowly convert to tetramers. Aluminum ethoxide is also tetrameric in its solid form. Titanium also prefers to be sixfold coordinated in solution, and the ethoxide forms trimers (fig. 2.2.2). Zirconium isopropoxide also increases its coordination from four to five, forming dimers.

One of the more studied alkoxide systems is that of tantalum. Tantalum is pentavalent, and prefers to be coordinated with six oxygens. If the alkoxide groups do not sterically hinder it, and in the absence of a solvent, the alkoxide monomers will complex with themselves forming dimers (fig. 2.2.3). The dimer is the only structure that can form because there is only one vacancy in the coordination shell. In a non-nucleophilic solvent, the dimer predominates as is evidenced by ebullioscopic [28,29,32] and NMR experiments [35-38].

Many solvents tend to break up these complexes. These same studies indicate that if the solvent has some nucleophilic character, some fraction of the dimers will be split into solvated monomers (fig. 2.2.4). In this case, the solvent takes the place of the second alkoxide molecule in the dimer. The solvation reaction, i.e., the breakup of the dimers, proceeds to equilibrium. The extent of solvation depends on the size of and branching in the alkoxy group, and the nucleophilicity, dielectric constant and temperature of the solvent. This is illustrated in table 2.2.2 [33], where the molecular

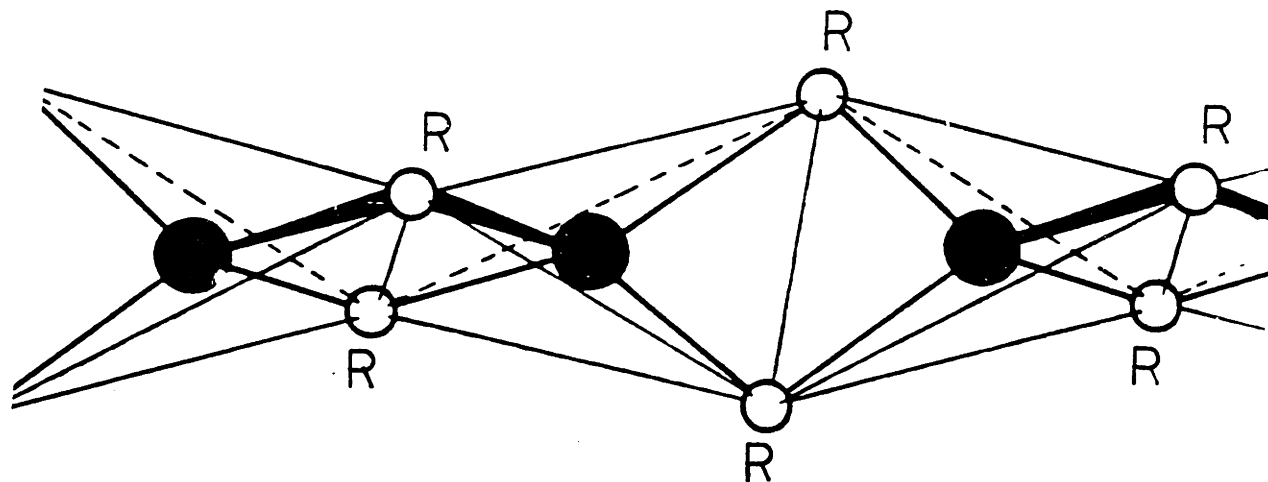


Figure 2.2.1  
Several units of the structure of magnesium ethoxide complexed with itself. Each magnesium atom is tetrahedrally coordinated with oxygen and shares an edge with two adjacent tetrahedra (after [34]).

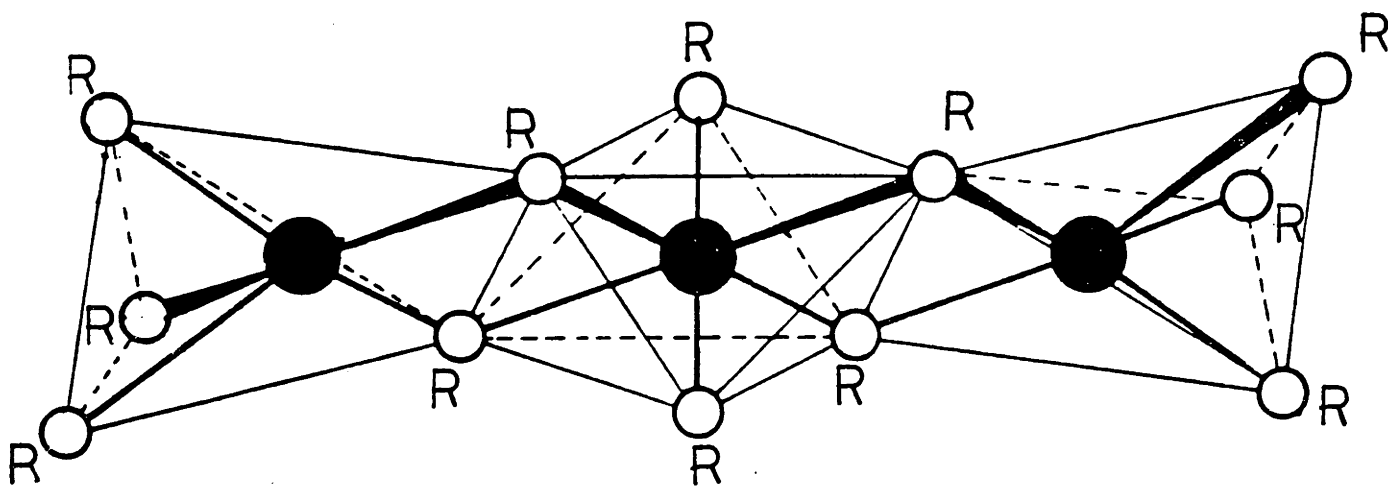


Figure 2.2.2  
Structure of titanium ethoxide trimer (after [34]).



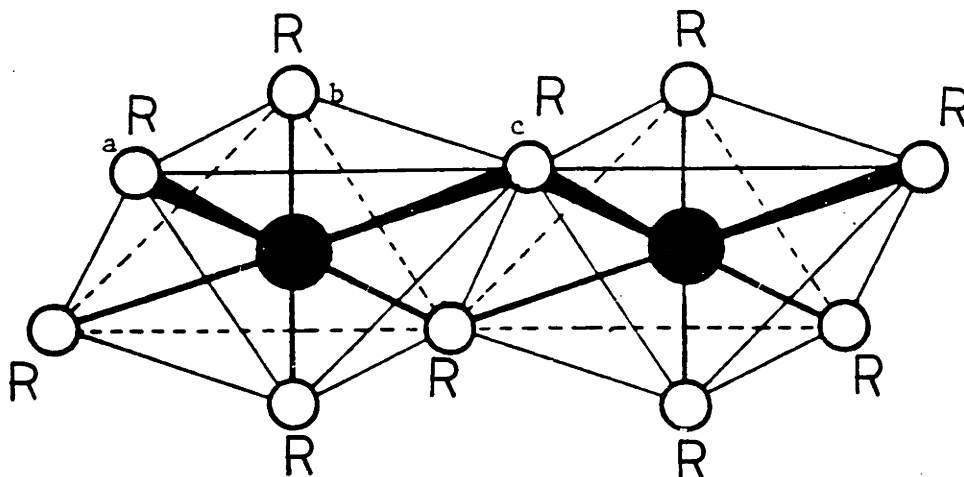


Figure 2.2.3  
Structure of tantalum ethoxide dimer showing the three NMR distinguishable ethoxy groups: (a) non-bridging equatorial, (b) non-bridging axial, and (c) bridging (after [35]).

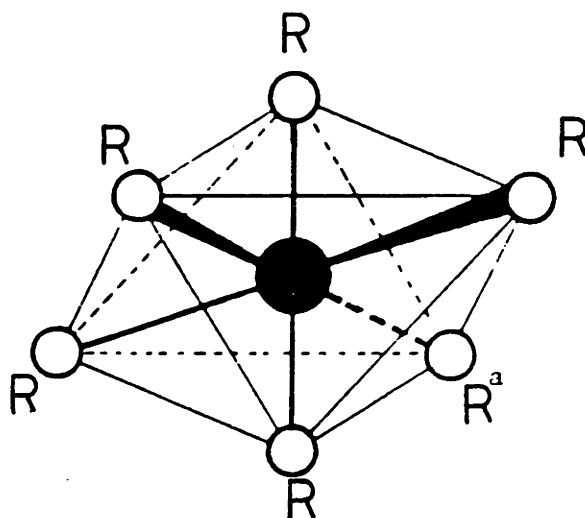


Figure 2.2.4  
Structure of solvated tantalum ethoxide monomer showing (a) the complexed solvent molecule (after [34]).

complexities of several tantalum alkoxides are reported in several solvents at their boiling points. Molecular complexity is defined as the average number of tantalum atoms per alkoxide complex. A value of one indicates that the alkoxide is completely uncomplexed and exists entirely as the solvated monomer in solution. A value of two indicates that the alkoxide exists entirely as the dimer, with the monomers completely complexed with themselves. Values between these two extremes indicate that there is a dynamic equilibrium between monomers and dimers, resulting in the non-integer value.

Table 2.2.2.

Molecular complexities of normal tantalum alkoxides in several solvents after references 32 and 33.

R in Ta(OR) <sub>5</sub>	Solvent					
	Benzene	Toluene	MeCN	Pyridine	Pr <sub>2</sub> <sup>i</sup> O	ROH
Me	1.98	1.83	1.50	1.01	1.75	1.76
Et	1.98	1.83	1.50	0.99	1.84	1.78
Pr <sup>n</sup>	1.95	1.83	1.50	0.99	1.84	1.70
Bu <sup>n</sup>	2.02	1.83	1.48	0.99	1.84	1.40

If the alkoxy group gets too large or branched, it will sterically hinder the approach of another molecule, resulting in no dimer formation. This is the case for the secondary and tertiary butoxides of tantalum, but not the normal or iso-butoxide as measured in benzene [30]. The nucleophilicity of the solvent is also key. If the solvent complexes with the alkoxide much more readily than another alkoxide molecule does, only solvated monomers will exist in solution. This is the case for all documented tantalum alkoxides in pyridine. The very nucleophilic free electron pair on the pyridine nitrogen complexes quite

readily with the alkoxide, resulting in a molecular complexity of one. The dielectric constant of the solvent determines how easy it is for the partially polarized alkoxides to be separated by the solvent, in the same way that it affects the degree of separation of ion pairs in organic solvents. This should be illustrated by the differences in the molecular complexity of the alkoxides in acetonitrile and pyridine. However, the donor power of the solvent seems to overshadow the dielectric constant effect. The temperature of the solution also comes into play because the complexation reaction has an activation energy of roughly 40 kilocalories per mole associated with it. Toluene boils at a temperature 30 degrees Centigrade higher than benzene, while both have almost identical dielectric constants and nucleophilicities. The molecular complexity is seen to decrease from benzene to toluene, as one would expect with the increased boiling temperature. The molecular complexity of each alkoxide in its parent alcohol is seen to vary considerably with the species examined. The ethoxide has the highest average molecular complexity at 1.78, indicating that almost 90 percent of the alkoxide exists in the dimer form.

The structure of tantalum methoxide, ethoxide and normal propoxide have been investigated using proton nuclear magnetic resonance [35,36,37] and electron spin resonance spectroscopy [34]. The spectra are shown to change drastically with temperature, exhibiting two coalescence temperatures. At very low temperatures for the ethoxide, e.g., the spectrum is made up of three distinct triplet-quartet pairs, indicative of three structurally different ethoxy groups. These structurally different groups are named for their positions in the dimer. There are two distinct non-bridging sites, in axial and

equatorial positions. The last distinct group is in the bridging position between the two metal atoms. As the temperature is raised past -30 C, two of the three methylene triplets coalesce into one triplet. As the temperature rises further, the remaining two triplets combine into one pair at 20 C.

The explanation for this phenomenon is based upon the theory that the ethoxy groups exchange positions within the ethoxide dimer. The structural isomerization reaction is an activated process. Therefore, at very low temperatures the process proceeds slowly. The sampling rate for NMR spectroscopy is about 1 millisecond [37]. If the exchange reaction occurs more slowly than this, the NMR spectrum will contain one peak for each magnetic environment of the nucleus being probed. However, if the exchange rate is much faster than this, the NMR spectrum will reflect an average position for the environment of the nuclei in question. At intermediate temperatures, the spectrum indicates a broad indistinct peak. This is defined as the coalescence temperature. For example, the rotation around a nitrogen single bond can lead to this phenomenon, as is the case in dimethyl formamide. At low temperatures, one can clearly distinguish the two isomers, but at higher temperatures only one is distinguishable.

In the case of tantalum ethoxide, the positions of the individual ethoxy group peaks are distinguishable at temperatures below -30 C. However, as the temperature is increased, the exchange rate of two of the three groups becomes appreciable. These two positions are the non-bridging sites, on the equatorial and axial positions of the dimer. They are assumed to rotate around the tantalum atom passing through an activated complex as depicted in figure 2.2.5. Below 20 C, the exchange

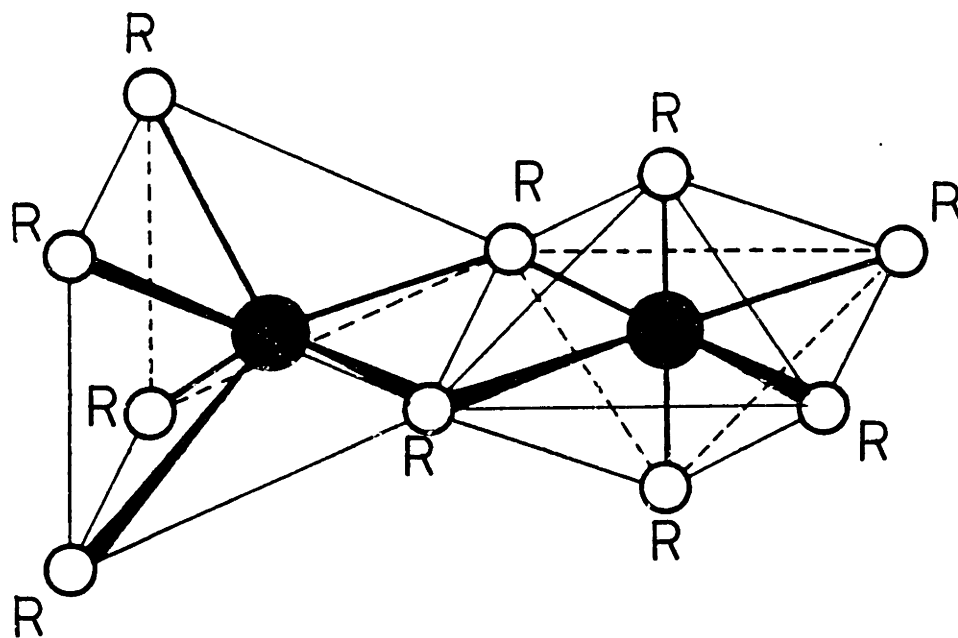
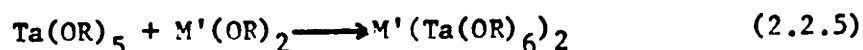
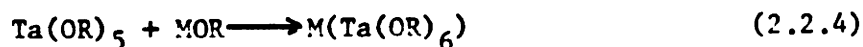


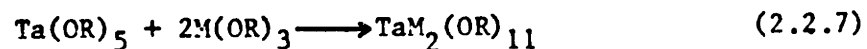
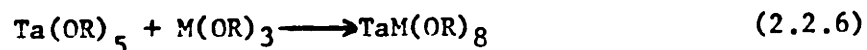
Figure 2.2.5  
Structure of activated tantalum ethoxide dimer during  
terminal-terminal exchange (after [35]).

rate of bridging for non-bridging groups is still small because the latter reaction has a higher activation energy than the terminal-terminal exchange. As the temperature is raised past 20 C, the latter exchange also becomes rapid. The result is that only one triplet-quartet pair is seen in the NMR spectrum at room temperature.

In addition to tantalum alkoxides complexing with themselves in solution, they have been shown to complex with alkoxides of other metals as well. Tantalum alkoxides have been shown to react stoichiometrically with alkoxides of alkali and alkaline earth metals, forming the complexes shown in the following equations, where M can be Li, Na, and K, and M' can be Mg, Ca, Sr and Ba.



The isopropoxide of tantalum has also been shown to react with aluminum and gallium isopropoxides in two ratios, forming the complexes listed in the following equations, where M in this case may represent Al and Ga.



Many of the complexes listed above are thermally stable, and may be separated by distillation under reduced pressure.

Tantalum alkoxides also react with chelating molecules such as 2,4-pentanedione and acetic acid. The case of the diketone has been well documented [34,39], and has been proven to attain the structure depicted in figure 2.2.6. Because the chelating molecule is bidentate, i.e. it is attached to the central metal atom in two places, it occupies both a covalent bond and the extra coordinating site. One might expect that because tantalum prefers to be sixfold-coordinated by oxygen, and has a

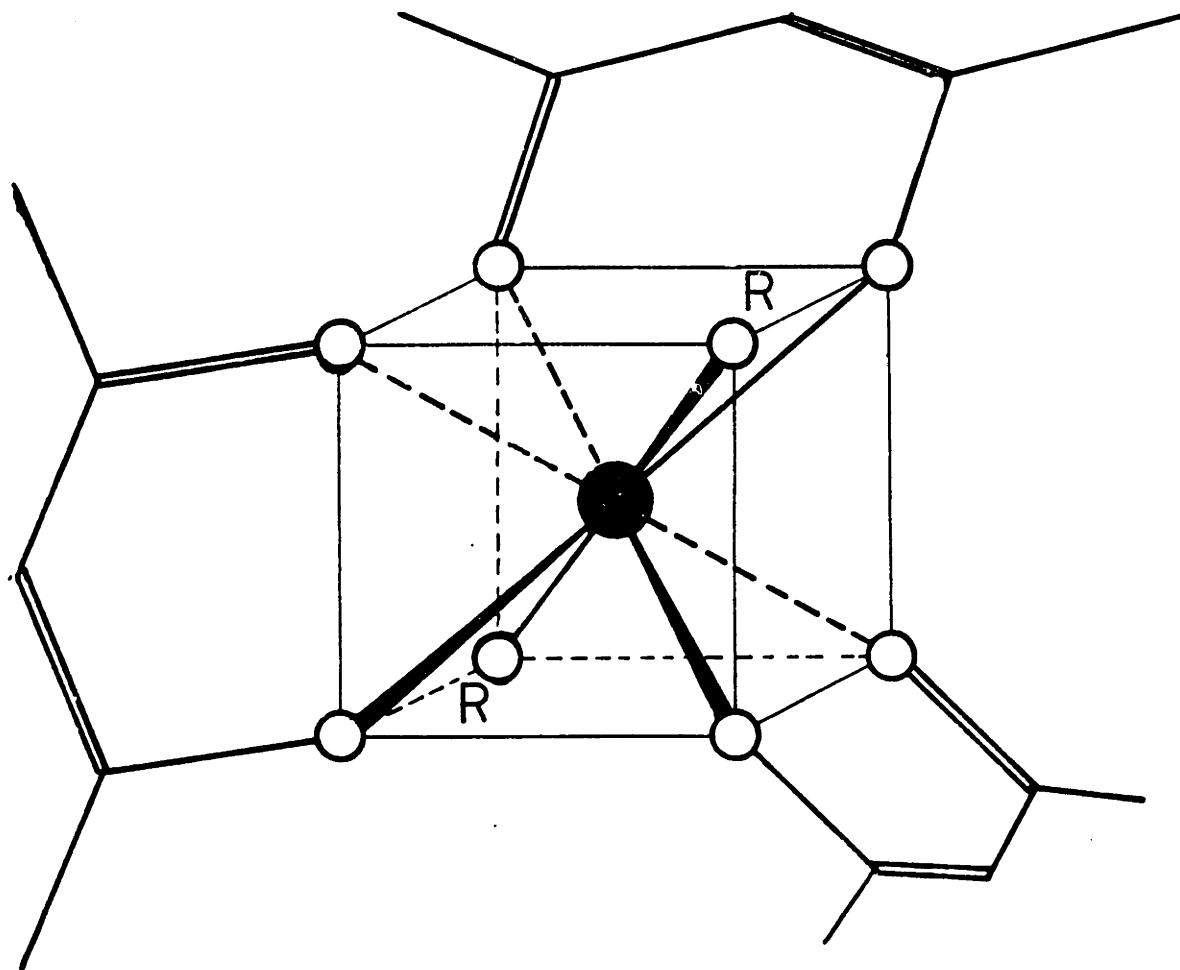


Figure 2.2.6  
A possible structure of tantalum diethoxide  
triacetylacetonate showing the central tantalum  
in eightfold coordination (after [39]).

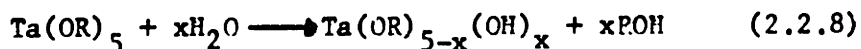
valence of five, that only one diketone would react with each tantalum atom. It has been documented, however, that for the case of acetylacetonone, the central metal atom can become up to eightfold-coordinated, yielding a diethoxide triacetylacetonate. The reaction between these two species is much like an alcohol exchange reaction. But in order for this reaction to be possible, the acetylacetonate molecule must first undergo a keto-enol tautomerization. The mobile hydrogen atom in this case is located on the methylene group between the ketone groups, being quite acidic due to resonances of the carbon-oxygen double bonds on either side. The resulting enol then undergoes the alcohol exchange reaction with the alkoxide monomer.

At this point we must remember that the solvation reaction is in a dynamic equilibrium. The solvent molecules are constantly replacing each other on the monomer. The acetylacetonate molecule already covalently bonded to the tantalum has the capability of occupying the coordination site as well with the oxygen of its remaining ketone group. If this were to occur, the resulting ring would be six-membered. This is quite favorable in organic chemistry, where five and six membered rings often form by intramolecular reactions to the exclusion of intermolecular reactions. This is most often explained in terms of the lack of strain in a six-membered ring allowing proximity of the two ends of the ring-forming molecule. In this case, the "back end" of the diketone molecule swings around and fills the coordination site. The resulting structure is further stabilized by the two resonance forms that can occur.

Another chemical reaction which occurs in tantalum alkoxides, also common to many other metal alkoxides, is hydrolysis. It is the first



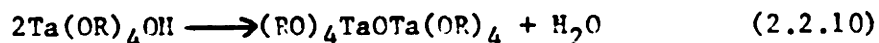
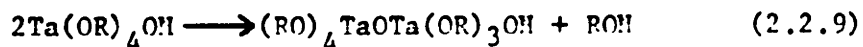
step in one of the possible polymerization processes of alkoxide molecules [28,32]. This reaction is characterized by a water molecule reacting with the alkoxide to form a hydroxide-alkoxide, giving off an alcohol molecule, as in



If enough water were present, tantalum ethoxide would hydrolyse completely, i.e., until none of the original ethoxy groups remained and the tantalum was surrounded with 5 hydroxyl groups. Hydrolysis is reported to be fast for alkoxides with small alkoxy groups in refluxing alcohol. Although the mechanism of this reaction is as yet undetermined, in optically active silanes it has been shown to be predominantly  $\text{S}_{\text{N}}2$  backside attack through a five coordinated activated intermediate, independent of the size and branched character of the alkoxy groups [40]. Several suggestions have been made, however, that the actual reaction mechanism ( $\text{S}_{\text{N}}1$  vs.  $\text{S}_{\text{N}}2$ ) depends on the acidity of the solutions [41, e.g.], where it is theorized that systems catalysed with acid hydrolyse via an  $\text{S}_{\text{N}}2$  backside attack while base catalysed systems hydrolyse via an  $\text{S}_{\text{N}}1$  frontside attack mechanism. It must be noted that before January 1987, there has been no evidence for an  $\text{S}_{\text{N}}1$  reaction mechanism in silanes. The  $\text{Si}^{+1}$  ion necessary in the  $\text{S}_{\text{N}}1$  process [41a] has only recently been determined to exist in certain limited reactions that do not include the hydrolysis and condensation of silicon alkoxides. Unlike many silane systems [42,43,44], however, tantalum alkoxides hydrolyse readily without the presence of catalysts, and the actual mechanism has not been determined.

The second step used in forming inorganic polymers is condensation [28,32]. During this reaction two partially hydrolysed molecules

combine to form a metal-oxygen-metal bridge (an oxide-alkoxide), giving off either alcohol or water



depending upon the relative kinetics of both reactions. In tetramethoxy silane, the rate of the water generating reaction is roughly five times faster than the alcohol generating reaction [45]. No such data are available for tantalum alkoxide systems.

In terms of an equilibrium process, the end result of either reaction would be the same because any water that is liberated by condensation is fed back into the system to hydrolyse as yet unreacted alkoxy groups. In reality, however, the structures that develop during these processes may be different depending on the relative rates of hydrolysis and condensation. Like hydrolysis, condensation proceeds quickly and to completion for tantalum ethoxide and propoxide at the boiling point of the parent alcohol [128,132]. Work on the molecular complexity of small alkoxides as a function of degree of hydrolysis has shown that the molecular complexity changes rapidly after the addition of water, then remains invariant. This indicates that equilibrium is very quickly approached. In addition, infrared spectroscopy does not reveal any residual hydroxyl groups present after hydrolysis and condensation using limited amounts of water for the ethoxide. Ebulliometry points to condensation also rapidly going to completion. Thus both hydrolysis and condensation go to completion under the conditions studied.

The rates of hydrolysis and condensation are functions of the size and branched nature of the alkoxy group. Generally, as the alkoxy group

gets larger or more sterically hindering, the rates of hydrolysis and condensation decrease [34]. However, the metal atom at the center of the alkoxide strongly impacts the rates of these reactions. From the data presented earlier, tantalum alkoxides generally react quickly, as do titanium, aluminum, magnesium and zirconium [34]. Silicon, on the other hand reacts relatively slowly [46,47]. Works on multicomponent silicates indicate that adding water to a solution of silicon and titanium ethoxides, e.g., results in the preferential reaction of the titanium species, forming a precipitate that is predominantly titania and leaving most of the silane unreacted in the solvent phase.

This has led to the adoption of reaction schemes such as prehydrolysing the silane under conditions where condensation is slow, and subsequently adding it to the faster reacting alkoxide. The abundance of silanol groups onto which the second alkoxide can condense insures a modest amount of chemical homogeneity in the resulting oligomers [46,47]. Some work has been done on in-situ water generation [48]. The results show that using the reaction of acetic acid and the ethanol solvent to generate the water needed for hydrolysis in a silicon and titanium ethoxide solution results in oligomers that do not precipitate after the subsequent addition of a large amount of water. This suggests the titanium species is reacting with the silane, and not only with itself.

The size of the product tantalum oxide-alkoxide oligomers is a function of the degree of hydrolysis as well as the particular alkoxide used [28,32]. Data indicate that in their boiling alcohols, the controlled addition of water causes tantalum alkoxides to polymerize into oxide-alkoxides of reproducible sizes. It has been shown

ebullioscopically that the molecular complexity increases as the degree of hydrolysis increases. The derivative of the molecular complexity with respect to the degree of hydrolysis indicated that an average of just over three water molecules react to link two ethoxide molecules. Based on these data, a model of the structure, the so-called bilinear chain, was proposed (fig. 2.2.7). Precipitation of the oxide-ethoxide occurs when the degree of hydrolysis exceeds 1.6. No precipitation was observed in the cases of the methoxide, n-propoxide, or n- or sec-butoxides. In the case of the methoxide, this was reportedly due to condensation not having gone to completion, leaving stable hydroxyl groups on the oligomers formed. However, the latter two alkoxides hydrolysed so slowly that the ebulliometry experiments showed the molecular complexity still increasing after 45 to 90 minutes. The methoxide was shown to produce the largest oligomers of the alkoxides at a given degree of hydrolysis (table 2.2.3).

Table 2.2.3.

Molecular complexities of several tantalum alkoxides at several degrees of hydrolysis. After refs. 28 and 32.

R in Ta(OR) <sub>5</sub>	h=0	h=0.5	h=1.0	h=1.5
Me	1.76	2.75	5.81	18.1
Et	1.85	2.71	4.91	9.16
Pr <sup>n</sup>	1.59	2.25	4.14	6.90
Bu <sup>n</sup>	1.36	1.53	2.07	3.23
Bu <sup>s</sup>	1.07	1.63	2.77	8.28

It should be stressed that condensation is not a process limited to inorganic systems. The word "condensation" comes from organic systems, many of which are biological, where the formation of a molecule from two smaller ones is accompanied by the production of a water molecule. Many organic polymers of commercial importance are synthesized via this

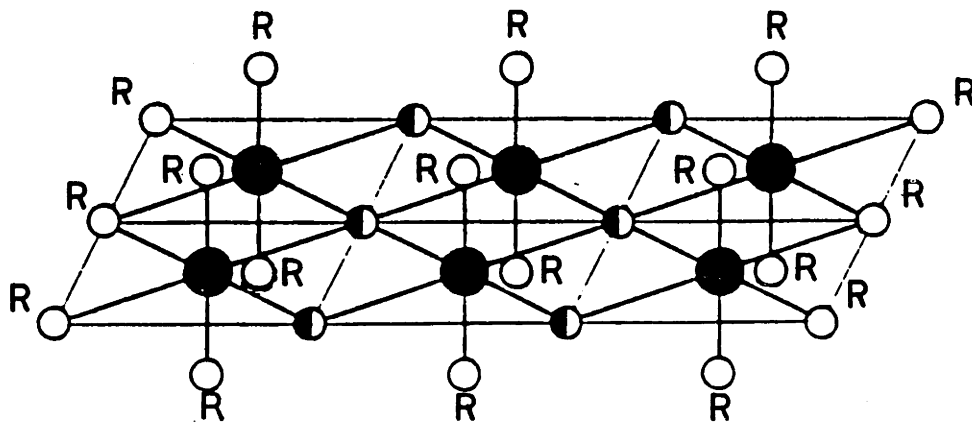


Figure 2.2.7  
Proposed structure of  $\text{Ta}_6\text{O}_6(\text{OEt})_{18}$  showing the  
bilinear chain (after [34]).

process, Nylon 6,6, e.g. As a result, there is much known about condensation reactions in terms of their kinetics and the species that are expected to form [49]. In fact, the hydrolysis and condensation of alkoxide systems reactions can be viewed as a polymerization process involving a bifunctional A-A type molecule (water) and, in the case of tantalum, a pentafunctional star-shaped molecule with B groups at the end of each "arm" of the star. In this model, A groups can react only with B groups. The first reaction of an A group with a star molecule is the hydrolysis step. It is immaterial that the alkyl group of the alkoxide is no longer part of the structure. The reaction of a previously hydrolysed molecule with another star molecule B group is the alcohol producing condensation reaction. One complication which arises is that one of the known condensation reactions involves two hydroxyl groups. However, as mentioned before, the water produced is fed back into the system via the hydrolysis reaction, and since the detailed structures are not being followed, the discussion below is unaffected.

There are several terms needing definition prior to this discussion. The first term of consequence is  $r$ , the ratio of the number of A groups to the number of B groups. This term is not equivalent the degree of hydrolysis, because in the case of tantalum alkoxides, while each water molecule has two ends, each alkoxide monomer has 5 reactive sites. However, the two are closely related. For a degree of hydrolysis of 1, the value of  $r$  is 0.4. The functionality,  $f$ , is defined as the number of reactive sites on the star shaped monomer. As just mentioned, in this system  $f$  equals 5. These remainder of the following discussion applies only to non-ringforming systems where equal reactivity applies. Equal reactivity is the name for the condition

where all possible polymerizable sites react at the same rate regardless of their positions on the growing polymer, and the size of that polymer. There are no steric or chemical hindrances to any particular sites reacting.  $\alpha$  is defined as the probability of one of the star-shaped monomers being connected to another, where

$$\alpha = r\rho^2 \quad (2.2.11)$$

and  $\rho_A$  is the probability of an A group being reacted. The number average degree of polymerization (molecular complexity) under these conditions and assuming that the polymerization reaction has gone to completion ( $\rho_A = 1$ ) is calculated as

$$\bar{x}_n = \frac{1}{1-r} \quad (2.2.12)$$

If condensation is complete, then  $\alpha = r$ . According to Flory [49], "Infinite network formation becomes possible when the expected number of chains (or elements) which will succeed  $n$  chains (or elements), through branching of some of them, exceeds  $n$ ." In other words, gelation occurs when when  $\alpha$  has reached a value such that there is a better than even chance that any given star-shaped monomer is connected to another.

Mathematically, gelation occurs when  $\alpha = \alpha_c$ , where

$$\alpha_c = \frac{1}{f-1} \quad (2.2.13)$$

Specifically for a five functional monomer if all of the above criteria are met, gelation occurs when

$$r_c = \frac{1}{f-1} \quad (2.2.14)$$

i.e.  $r_c = 0.25$ . Converting this to a degree of hydrolysis, we arrive at  $h_c = 0.625$ . In other words, we expect gelation to occur when the mole ratio of water to alkoxide reaches 0.625.

Clearly this does not happen in the case of tantalum ethoxide, where gelation is not observed before precipitation occurs at a degree

of hydrolysis of 1.6. If gelation were to occur, it must happen at a higher degree of hydrolysis. Therefore, if the assumptions made in the model are valid, for every condensation that results in an increase in the degree of polymerization of a given oligomer, at least 1.5 result in ring formation. We shall define this term as the ring-ratio. Using the bilinear chain model, less than half of the 5 original ethoxy groups per tantalum are present upon precipitation. This shows how easily these species condense to form densely crosslinked structures, even at low degrees of hydrolysis. Precipitation occurs because the oligomers lose much of their organic nature during the polymerization process. i.e., they become "more inorganic". As the solvent does not change with the exception of a small amount of water being consumed during hydrolysis, the solubility parameters of the solvent and solute diverge, causing precipitation.

The next point to be addressed is if precipitation of the oligomers is due to their crystallizing out of solution. In the case of titanium ethoxide, the addition of minute amounts of water to an ethoxide-ethanol solution results in the precipitation of small rhombohedral prisms identified as the oxide ethoxide. Crystallization occurs due to the regularity of the titanium oxide-ethoxide structure allowing the oligomers to pack well with each other. That crystallization does not occur in the tantalum ethoxide system is a strong argument for a more randomly polymerized/branched structure than its titanium analog. This point argues against the bilinear chain model.

Based on the gelation model calculation, it is possible to conceptualize the structure of an average oligomer. A structure comprised of a single width ribbon of edge sharing octahedra where



condensation has occurred at four of the six corners is characterized by a ring-ratio of 1. Examining the bilinear chain model, one finds that for small oligomers (i.e., a molecular complexity of 4) the ring ratio is 1. However, as the molecular complexity increases the ring-ratio asymptotically approaches 1.5. This structure is probably indicative of the number and size of the rings that predominate, i.e., they are small and abundant. Their number indicates that they are probably not individual rings connected by bridges, but are instead more like edge sharing polyhedra. While the bilinear chain model is successful at predicting the correct ring-ratio, as will be presented later, it does not account for other structural details observed for the oligomers.

Once the oligomers have been formed and the coating solutions are no longer changing, supported films are easily produced by any number of coating techniques [50]. Spin-coating is the most convenient for coating silicon wafers and will be discussed here [15,51-54]. The thickness of layers deposited from alkoxide solutions [15,51] is proportional to the weight fraction of solids in the solution, and inversely proportional to the square root of the spin speed of the silicon wafer. This is also the case for standard photolithographic resists used in semiconductor processing [55]. For silica, titania, mixtures of the two, and tantala deposited from alkoxide solutions, excellent results, in terms of thickness uniformity and the absence of defects, have been reported for solutions containing between one and five weight percent oxide [15,52].

### 2.3. Drying gels

After the films have been deposited from solution, the solvent must be removed. One of the major considerations for pursuing thin films as opposed to bulk pieces on which to measure electrical properties is the relative ease in which films are produced. Silica films thicker than 1 micron are difficult to produce due to the fragmentation of the samples from stresses that arise during drying [56]. Bulk gels thicker than 1 cm are difficult to produce as well. The difference in maximum dimension attainable is due to the substrate not allowing the film to relax in the plane parallel to the substrate.

Two models have been proposed to account for the occurrence of crack formation during the drying process. The first relies on pores of different sizes and capillary forces to produce tension in the gels [44]. First we will assume a gel structure consisting of two adjacent cylindrical pores, each with a different radius (fig. 2.3.1). Initially, the solvent phase covers the entire surface of the gel. As the solvent evaporates the liquid/vapor interface approaches the surface of the gel and eventually penetrates. The liquid/solid interface has a lower energy than the solid/vapor interface, causing the liquid to favor spreading onto the dried solid. This phenomenon gives rise to tension in the liquid, the so-called redistribution pressure. Because the two adjacent pores have different radii, they will support different columns of solvent against the redistribution pressure. However, in addition to the component of the force that is normal to the gel surface, the liquid/vapor interface applies a horizontal force to the walls of the pores. Due to the differing heights of the liquid in the adjacent pores, these horizontal forces are applied at different places, causing

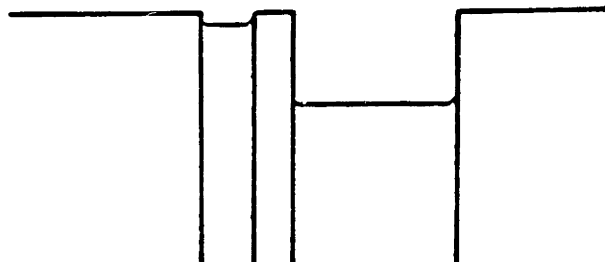


Figure 2.3.1  
Model of drying gel showing two adjacent pores of  
different diameters. Shear stresses develop due to the  
menisci residing at different heights in the pores  
(after [44]).

a shear to develop in the skeletal material. If this shear overcomes the the cohesive forces in the gel, the body will crack.

The second model [56,57] uses the viscoelastic properties of the gel in conjunction with the redistribution pressure to arrive at tension in the gel. In this case, the liquid still wants to spread up the sides of the pores to reduce the total energy of the system. When it is unable to do so, the gel reacts to lower the surface area by changing the aspect ratio of the the skeletal material. This is accomplished by the densification to a lower surface area to volume structure. If the solvent has a reasonable viscosity, the interior part of the gel cannot densify at the same rate as the exterior because the liquid in the gel cannot redistribute itself fast enough. This causes the outside of the gel to shrink faster than the interior, creating tension in the outer layer. As before, if this tension is greater than the cohesive forces in the gel, the gel will fragment.

Specialized treatments have been developed to overcome this problem, including slow drying [58,59], hypercritical drying [60], and the use of drying control chemical additives (DCCA) [60,61]. Slow drying allows time for the solvent to be redistributed in the gel, thereby lowering the redistribution pressure and allowing the inside of the gel to shrink at the same rate as the outer skin. Hypercritical drying completely eliminates the solvent/vapor interface, so that in the case of the first model there are no capillary forces, and in the second the speed of redistribution of "solvent" is much increased within the gel allowing the body to shrink uniformly. Several theories have been advanced by the authors of the DCCA work, the most recent being that the use of DCCA in silica systems decreases the rate of hydrolysis while

increasing the rate of condensation. This leads to more of the monomer being bonded into the network upon gelation. As a result, the gel has a more uniform pore size and is harder, both conditions favoring less cracking upon drying.

Supported alkoxysilane derived films spun onto silicon up to 1 micron thick dry in air without serious problems [51,63], although it has been reported that the maximum thickness attainable before cracking depends on the coating application procedure. Silica coatings made by dipping substrates cracked when the thickness exceeded 0.7 microns [63] or 1.1 microns [64]. The same workers who could not exceed a 0.7 micron thickness by dip-coating, spun identical solutions onto silicon wafers, obtaining a maximum thickness of 1.1 microns. Gel-derived titania films deposited by spin coating cracked upon exceeding 1100 nm in thickness [65]. An attempt to overcome the barriers to thick silica film formation using complexing agents, e.g. acetylacetonate, combined with small amounts of titanium ethoxide was successful in extending the maximum thickness to greater than 2 microns [64].

Drying in air serves to introduce more moisture into the film as well as to evaporate residual solvent. The additional water promotes the hydrolysis and condensation reactions if the alkoxide has not been completely reacted up to that point. These processes help to remove some of the residual organics from the system. More importantly, however, densification accompanies the additional condensation. This can give rise to tension in the gel.

Tension arises in a thin film because the film is constrained [57]. The substrate is generally covered with a layer of surface hydroxyl groups and several layers of condensed water. Just as condensation

occurs within the film, substrate hydroxyl groups serve as potential sites onto which condensation may occur. The end result is strong film-to-surface bonding which prevents movement of the film in the plane of the substrate. After covalent bonds have formed to the substrate, condensation is still progressing in the film. This additional condensation results in the compaction of the structure from which tension arises.

If unconstrained, the film would shrink in all three dimensions to relieve the developing stress. However, it can only shrink perpendicular to the substrate as is the case for thin layers of glass between two layers of another material [66,67]. Models for sandwich seals (fig. 2.3.2) predict that the ratio of the length of the seal to the thickness of the seal ( $b/a$ ) must be at least 3 for a condition termed plane strain to arise in an area surrounding the exact center of the seal. Plane strain is the name of the condition where there is no strain in the plane of the substrate, only perpendicular to it. Supported films are similar in geometry to the sandwich seals. In fact, the seals were modeled as supported films by noting that a plane of symmetry exists at the center of the sandwiched material. Therefore, for a film of thickness  $t$ , the plane strain condition arises in all areas except those within  $1.5t$  from the edge of the film. For alkoxide derived films where the thickness is typically less than 1 micron, coated substrates inches in diameter are essentially entirely in plane strain. As in these structures, the only way that stress parallel to the plane of the substrate can relax is by viscous flow within, or relaxation of the network. However, if these stresses are not annihilated by these mechanisms, they may be high enough to result in

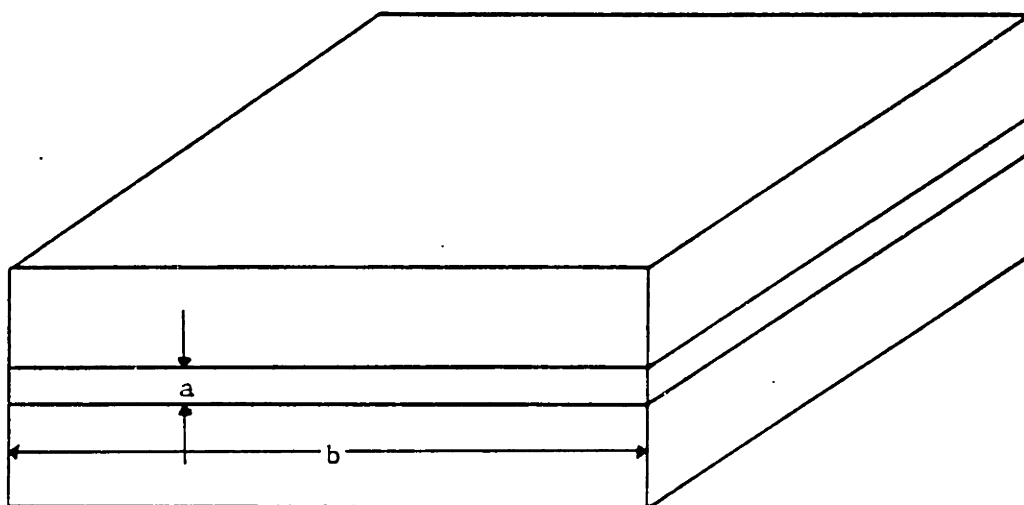


Figure 2.3.2  
Schematic of sandwich seal showing the thickness (a) and  
the width (b) of the seal (after [66]).

the mechanical failure of the film.

#### 2.4. Densification of gels

The final step in generating ceramic films via wet-chemical processing involves heating the films. Several processes occur in the gel upon raising the temperature. First, heating causes residual organics and water to be driven off. Then as the structure is allowed to relax at higher temperatures, condensation occurs as these groups are brought into closer proximity. This might be envisioned as crosslinking, and causes the densification to be irreversible. Finally, as the glass transition temperature is approached, the film densifies by viscous sintering, and possibly crystallizes. For silica coatings, adsorbed and chemically bonded water and alcohol are evaporated between room temperature and 300 C [68]. When fired in an oxidizing atmosphere, residual organics decompose to carbon dioxide and water between 300 and 500 C.

The total amount of weight lost upon firing depends on the conditions of gel formation. In HCl catalysed silica systems, increasing the initial degree of hydrolysis from 1 to 4 decreases the weight lost on heating to 250 C almost in half from 40% to 23% [59]. These gels continued to lose weight until 700 C, the highest temperature of the experiment reported. Titania films made from the ethoxide lose 22% of their weight by 300 and lose no more up to 800 C [69]. Titania silicates behave as an average of the two extremes, losing most of the total weight loss by 300 C, but continuing to lose weight past 700 C



[70].

Care must be taken during heating to insure that outgasing and organic decomposition occur before substantial pore closure. If this is not the case, gases produced will be trapped within the body to form pores, and in extreme cases cause foaming [71,72,73]. In fact, where foaming is desired, agents may be added to the gels to amplify this effect. For this reason, for most ceramics formed from carbonates, nitrates and other salts, the powders are calcined before pellets are made out of them. However, this can be counterproductive during gel processing, as will become apparent shortly.

Densification also occurs upon heating. Several processes can contribute to densification of amorphous inorganic systems; condensation of hydroxyl and alkoxy groups in the skeletal material and on the pore walls [59], rearrangement of particles [74], viscous sintering [75,76] and sintering of crystalline powders [74]. TEOS gelled in the presence of hydrochloric acid at an acid concentration of 0.1 moles per liter formed pieces that were completely densified by 700 C. For ammonia catalysed TEOS systems, small pores begin to collapse between 400 and 500 C, while larger pores collapse between 700 and 900 C. This leads to two distinct regions of the densification curve [59]. Commonly, silica films are fired to between 900 and 1000 C for densification to be assured [77,78,79]. Additions of soda to ammonia catalysed silicate gels causes densification at lower temperatures, as might be expected due to the lower viscosity of the skeletal material. Gels having 33 mole percent soda were dense by 600 C [69].

Crystallization may occur during the densification process, and in gel-derived systems these two processes are viewed as being competitive.

This is because viscous sintering operates only in noncrystalline systems [75]. After crystallization, densification may only occur by diffusion through the lattice. This process is generally much slower than viscous sintering at a given temperature [47]. Therefore, in order to produce a dense body at very low temperatures where diffusion is slow, densification should be complete before crystallization occurs. If this does not happen, one will lose one of the benefits of using the gel process for the production of ceramics. Gel derived anorthite crystallizes after densification is almost complete [47], as do silica [59] and a mixed alkali aluminoborosilicate [80]. However, this is not the case with gel derived alumina [81].

## 2.5. Electronic Characterization

The electronic devices of interest are of the general metal-insulator-silicon (MIS) capacitor type. The capacitance-voltage technique (C-V) is a standard test in the study of semiconductors to characterize not only the dielectric constant of the insulating layer, but also interface states and fixed charge in the dielectric. There are three regimes of behavior of the capacitance as a function of the applied bias voltage in an MIS capacitor; inversion, depletion, and accumulation [82]. These regions are differentiated by the type of charge that builds up on the semiconductor surface to balance the charge in the gate electrode. Accumulation occurs when a bias is applied to the gate electrode that increases the concentration of majority carriers at the semiconductor-insulator interface. Depletion occurs when a low

bias of the opposite sign is applied, creating a layer in the semiconductor that is depleted of the majority carrier. If the magnitude of this bias is increased sufficiently, a layer of minority carriers will form at the insulator-semiconductor interface. This condition is called inversion. The energy band representations of these conditions, as well as a theoretically predicted capacitance-voltage curve, appear as figure 2.5.1.

The behavior of principal concern in the present work is that of accumulation. Under these conditions, the capacitance is solely a function of the permittivity of free space ( $\epsilon_0$ ), the area of the gate electrode (A), the thickness of the dielectric layer (l), and the dielectric constant of the insulator ( $k'$ ),

$$C = \frac{\epsilon_0 k' A}{l} \quad (2.5.1)$$

If the system of interest is made up of two layers, the lower being silica, and the top being tantala, this is modeled as two capacitors in series, i.e.,

$$\frac{1}{C} = \frac{1}{C_1} + \frac{1}{C_2} \quad (2.5.2)$$

where the subscripts 1 and 2 are for the individual layers and the unsubscripted variables are for the composite structure. Substituting for and combining all the variables and rearranging, we arrive at

$$\frac{1}{C} = \frac{l_1}{\epsilon_0 k'_1 A_1} + \frac{l_2}{\epsilon_0 k'_2 A_2} \quad (2.5.3)$$

Since the area of the gate electrode is constant, we rearrange to get

$$\frac{\epsilon_0 A}{C} = \frac{l_1}{k'_1} + \frac{l_2}{k'_2} \quad (2.5.4)$$

Proceeding further, we obtain

$$k'_1 = \frac{1}{l_1} \left( \frac{\epsilon_0 A}{C} - \frac{l_2}{k'_2} \right) \quad (2.5.5)$$

Therefore, knowing the dielectric constant of silica and all of the geometrical dimensions of the system, the dielectric constant of the

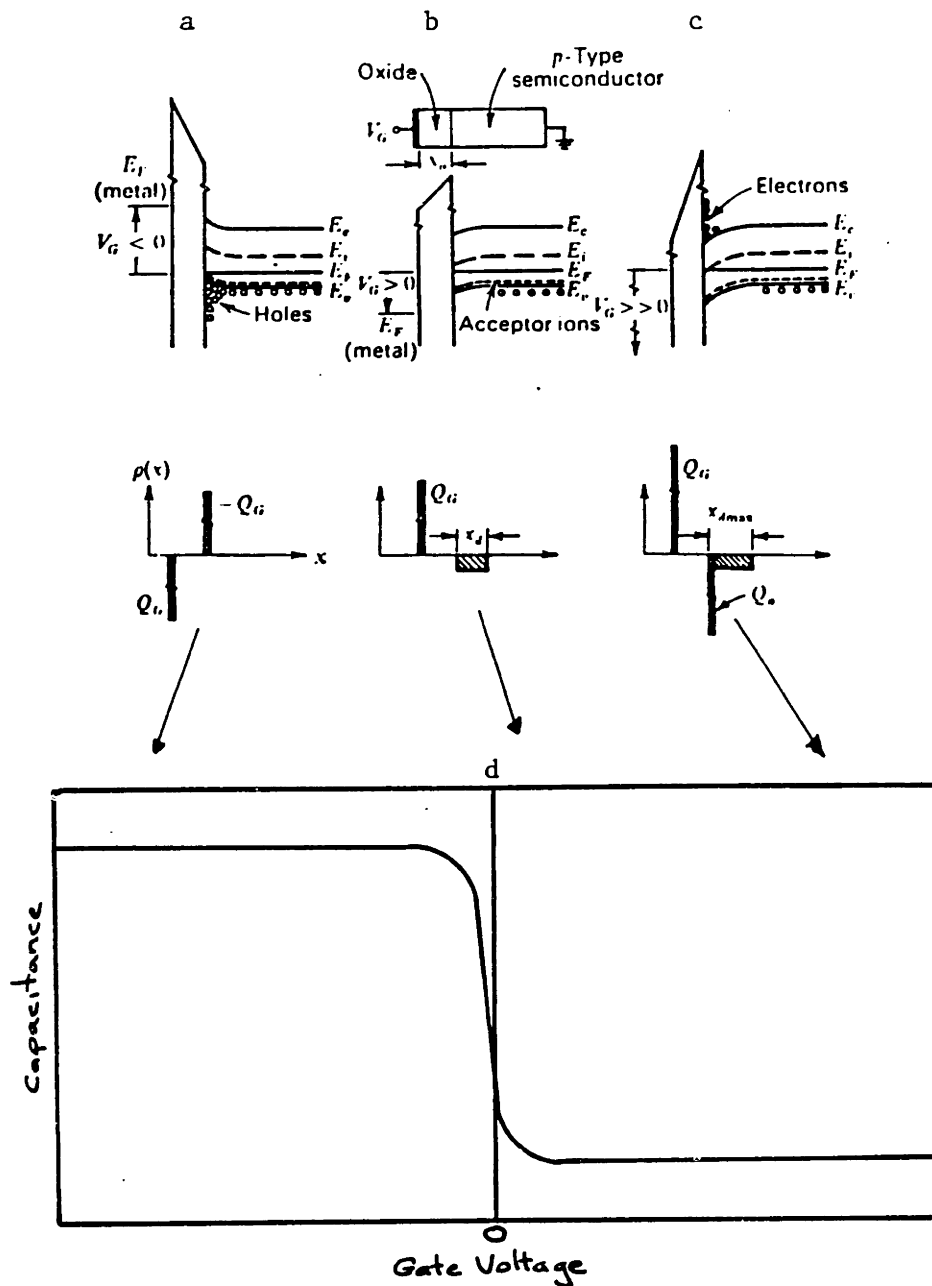


Figure 2.5.1  
 Energy band representations of different bias conditions of an MOS capacitor on a p-type substrate. Also shown are the concentration of various species for the three bias of (a) accumulation, (b) depletion and (c) inversion (after [82]). Also shown is a typical C-V curve for a device on p-doped silicon (d).

tantala layer may be calculated from the capacitance of the composite.

Another electronic property of interest is the loss. This material property is a measure of how much energy is lost upon polarizing a dielectric media. For applications where a high capacitance is needed, it is important to select a material with both a high dielectric constant and a low dielectric loss,  $\tan \delta$ .  $\tan \delta$  can be calculated from data collected during the C-V experiment using the relation

$$\tan \delta = \frac{1}{\omega RC} \quad (2.5.6)$$

where  $\omega$  is the frequency, R is the resistance and C is the capacitance of the circuit.

The loss factor of anodic tantala thin films has been measured [74]. It was found to be 0.004 for 500 nm thick films measured at 1 kHz at 300 K. However, as the thickness was decreased, the loss factor increased to 0.015 for 10 nm thicknesses. For a 40 nm thickness, the loss factor was 0.007. The increase in  $\tan \delta$  in these films was ascribed to tunneling of electrons into the surface. If this is the case, the loss factor should be quite dependent on the preparation conditions.

For VLSI applications it is also important for the dielectric material to have a high resistivity so that the MOS devices need not be refreshed often. Therefore, in determining the suitability of a material, the dc leakage current should also be characterized.

## 2.6. Gel-derived Tantala

Tantalum oxide has been reported to have been produced using

tantalum ethoxide and hydrolysis ratios of 1,2 and 3 [1], and 10 [15]. As mentioned earlier, the former paper dealt with corrosion protection of aluminum by the application of a gel derived tantala coating. No processing details are given, possibly because the authors applied for a patent on this process. One must note, however, that in order to obtain homogeneous coating solutions at the high degree of hydrolysis mentioned, an additive must have been used in order to stabilize the resulting sol. Three separate dips into the coating solution were used to eliminate problems with pinholes, and to build up the thickness of the coating. No firing step was mentioned. Aluminum wire coated in this manner were resistant to the attack of wet chlorine for at least 60 hours. This point suggested that the films as deposited were relatively dense with no high temperature treatments.

The latter study [15] disclosed many experimental parameters, including the use of hydrochloric or acetic acid to prevent the premature precipitation of powder. The resulting solutions were clear sols after the addition of enough water to bring the degree of hydrolysis up to 10. The coating and densification behavior of the films on silicon substrates was characterized in addition to thermal analysis done on bulk pieces of gel resulting from air drying of the coating solution. Thermogravimetric analysis showed only a 17 percent weight loss for samples stabilized with acetic acid fired in either oxygen or nitrogen. Just over half of this weight loss was due to the loss of solvent below 150 C, while most of the remainder was lost between 430 and 500 C, depending on the atmosphere. A final weight loss was reported at 730 C. The last two losses are attributed only to the loss of carbon and hydrogen from the network. A sample TGA trace is

included as figure 2.6.1.

These gels are shown to crystallize slowly at 400 C, the beta phase finally being well developed after 16 hours at that temperature. The thickness of the spun-on films was shown to vary as the square root of the spin speed, with the thickness varying plus or minus 2.5% across the face of the wafer. The films were shown to shrink just over 50% upon firing to 800 C, with most of the change occurring below 400 C. The refractive index was shown increasing from 1.75 in the as deposited film, to 2.1 in the films fired to 800 C. Interestingly, the films were said to start crystallizing between 635 and 650 C. The difference between film and bulk crystallization temperatures for materials derived from gels was attributed to a change in the number of nucleation sites.

No reason is given for the discrepancy between the final refractive index of the fired tantalum and those existing in the literature. If the difference is due to pores, it is possible to estimate how much porosity remains in the film based on the refractive index of the material. The assumptions in obtaining this estimate are several. First, we will assume that the film is made up of randomly distributed spherical pores in a tantalum oxide matrix, using refractive indices of 1 and 2.2 respectively for these phases. Secondly, the imaginary part of the refractive index will be taken as zero. With these assumptions in mind, one may use the relationship between refractive index and dielectric constant,

$$n^2 = k' \quad (2.6.1)$$

A second equation relates the dielectric constant to a volume fraction of dispersed second phase,

$$k' = \frac{V_m k'_m \left( \frac{2}{3} + \frac{k'_d}{3k'_m} \right) + V_d k'_d}{V_m \left( \frac{2}{3} + \frac{k'_d}{3k'_m} \right) + V_d} \quad (2.6.2)$$

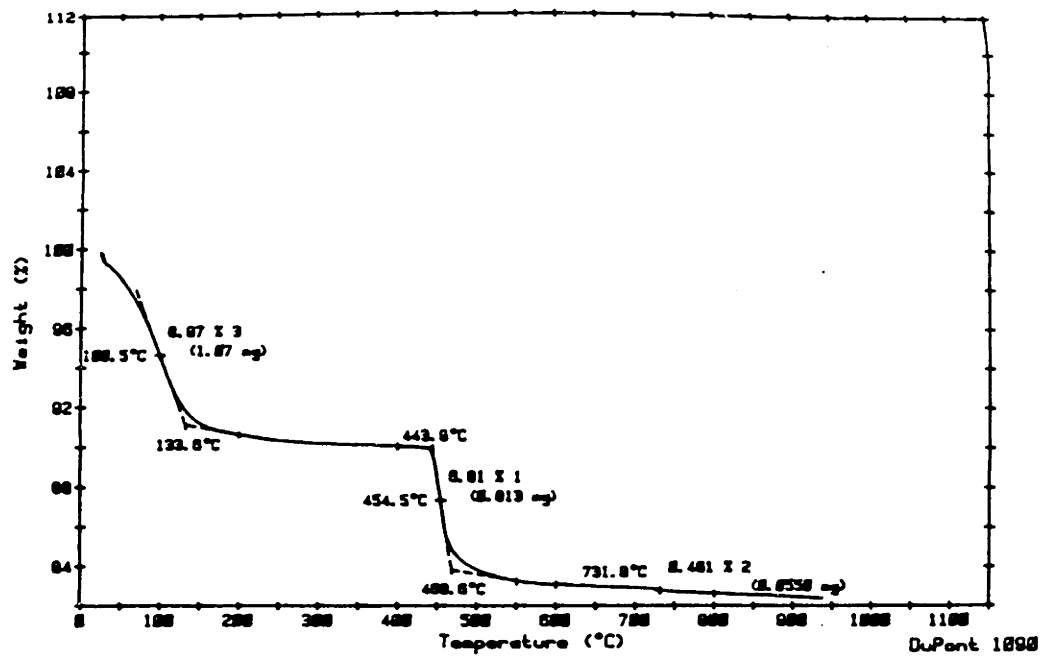


Figure 2.6.1  
 Thermogravimetric analysis of tantalum sols made from  
 the ethoxide using HCl as a catalyst (after [15]).



where the subscripts m and d represent the matrix and dispersed phases respectively. Substituting and rearranging, we find

$$\frac{V_d}{1 - V_d} = \left( \frac{2}{3} + \frac{n_d^2}{3n_m^2} \right) \left( \frac{n_m^2 - n^2}{n^2 - n_d^2} \right) \quad (2.6.3)$$

Inserting the refractive indices of air and crystalline tantala for the phases, one calculates the pore volume fraction as between 8 and 9 percent.

One must note, however, that the calculated density is much dependent on the value of the refractive index used for the fully dense material. Although 2.2 has been used here, values have been reported ranging from 1.96 to 2.42. This calculation, therefore, must not be relied upon too heavily.

### Chapter 3. Experimental Procedure

Tantalum ethoxide was purchased from Alfa Products as optical grade (99.999%). The pale yellow liquid was packaged in sealed glass ampoules. Multicomponent systems were made using reagent grade magnesium ethoxide, aluminum isopropoxide, titanium ethoxide and zirconium propoxide, all purchased from Alfa Products. Prior to use, the tantalum ethoxide was transferred to vacuum/flame dried Schlenk tubes in a glove box so that material could be withdrawn from its container in the laboratory while still maintaining a dry inert atmosphere over this reactive precursor. The other alkoxides were transferred to the reaction vessels while in a dry box immediately prior to use.

Anhydrous ethanol was received in gallon cans. Karl Fischer reagent was used to determine the water content of the solvent as received. This initial level (0.1%) was too high for several experiments, so the ethanol was further dried by refluxing over magnesium ethoxide. Ethanol was withdrawn from the distillation apparatus immediately prior to use. Using Karl Fischer reagent on solvent prepared in this manner revealed no measurable water in samples as large as 10 ml.

Water for hydrolysis was used as deionized by the central facility system. This water had a measured pH of 6.6. Toluene used in the nuclear magnetic resonance (NMR) experiment was reagent grade, dried over 5 Angstrom molecular sieve and filtered prior to use. Deuterated toluene (d-8) was used directly from the glass ampoules immediately

after opening.

All glassware was dried prior to use to reduce exposure of the ethoxide to the adsorbed moisture. The drying process consisted of first heating the glassware to 125 C in an oven. It was evacuated, and heated over a bunsen burner to drive off all moisture possible. After cooling, the glassware was backfilled with nitrogen, which was dried by having passed through a calcium sulfate filled column. All syringes and hypodermic needles were dried by repeated flushing with freshly distilled hot dry ethanol. Millipore filters used during coating were flushed with cool dry ethanol to remove as much moisture as possible.

Silicon substrates were supplied by the IBM Corporation. Silicon wafers 2.25 inches in diameter, both n and p doped, were cleaned thoroughly prior to coating. First they were cleaned of organics in a solution of ammonium hydroxide and hydrogen peroxide. Then the thin oxide layer was removed in dilute hydrofluoric acid. Finally they were cleaned of ionics in a solution of hydrochloric acid and hydrogen peroxide (see table 3.1 for details of cleaning procedure). After cleaning, the wafers were not wet by aqueous solutions, indicative of the absence of any oxide layer and the presence of the hydrophobic silicon surface. Wafers used to characterize the spin coating process (samples not used for electronic characterization) were coated with tantalum ethoxide solutions immediately after cleaning. Wafers used for electronic characterization were oxidized in dry oxygen at 950 C for 20 minutes.

Table 3.1.

## RCA Cleaning Procedure

step	solution	temperature	time
1	200 ml conc. $\text{NH}_4\text{OH}$ 200 ml conc. $\text{H}_2\text{O}_2$ 1200 ml $\text{H}_2\text{O}$	80 C	20 min.
2	cascade rinse	20 C	15 min.
3	5% HF	20 C	20 sec.
4	$\text{H}_2\text{O}$	20 C	30 sec.
5	200 ml conc. HCl 200 ml conc. $\text{H}_2\text{O}_2$ 1200 ml $\text{H}_2\text{O}$	80 C	20 min.

Two processes were used for the different sets of samples because of the different measurements to be performed on them. Wafers intended for electronic characterization were coated with silicon dioxide prior to coating with the tantalum ethoxide solution so as to passivate the surface of the wafer. This resulted in the elimination of dangling silicon surface bonds by the growth of the oxide layer, and made the results of the electronic characterization more reproducible. The  $\text{SiO}_2$  layer was measured using ellipsometry prior to the deposition of the tantala, and was  $16.3 \pm .1$  nm thick. The thickness of the entire dielectric layer was measured using profilometry, and the thickness of the tantala film was calculated from the difference between the thickness of the entire film and that of the silica layer.

Ellipsometry is the measurement technique of choice for determining the thickness of single layers. For samples that were to be used for thickness measurements only, an underlying oxide layer would affect the

ellipsometry measurement. Therefore these samples were coated with the ethoxide solution without having had an oxide layer grown on the silicon wafer prior to spin coating. Exposure to air results in a very thin surface oxide which will provide the silanol groups necessary for good adhesion to the substrate

Coating solutions were prepared in the following manner: Tantalum ethoxide, measured volumetrically in a disposable syringe, was injected into a clean dry 50 ml round bottom flask through a silicone rubber serum stopper. To this, dry ethanol was added in a similar fashion. In a separate flask, the desired amount of water was diluted with almost 100 times its volume in dry ethanol (see table 3.2 for a representative recipe). The water-containing solution was then added, one drop at a time, by syringe to the stirring ethoxide solution over roughly one minute. The resulting solution was then allowed to stand for 30 min. to 1 hour. Unless otherwise specified, all coating solutions contained the equivalent in ethoxide of 2.5 weight percent tantalum oxide. This means that 100 grams of solution contained the equivalent of 2.5 grams of tantalum oxide. Using the molecular weight (441.89 g/mole) of the oxide and the ethoxide (406.05 g/mole) together with the density of the ethoxide (1.6 g/ml), the volume of ethoxide was calculated (2.87 ml in this example).

Table 3.2.

Typical recipe for tantala coating solution. The oligomers form as solution 2 is slowly added to solution 1.

solution	component	amount
1	ethanol	35 ml
	tantalum ethoxide	1.0 ml
2	ethanol	6.91 ml
	water	.071 ml

Multicomponent coatings were prepared in much the same manner. The second component in alkoxide form was added to the tantalum ethoxide and allowed to dissolve before the dilution with dry ethanol. Clear solutions resulted. The concentration of oxide in these solutions was calculated in an identical manner as the single component systems, with tantalum comprising 2.5 weight percent of the solution weight. The amount of water used was calculated based on a degree of hydrolysis of 1 for the tantalum ethoxide only. The result of these calculations is that the multicomponent solutions were more concentrated and less hydrolysed than the single component solutions when all of the alkoxides are taken into account.

Infrared spectroscopy on solutions was performed on a Perkin Elmer 297 using a calcium fluoride liquid cell with Teflon spacers. These materials were stored under vacuum for 24 hours prior to use to reduce adsorbed moisture. Solutions for IR spectroscopy were prepared in a similar way as those used for coating solutions except that the water-containing solution was injected quickly into the solvated alkoxides. After mixing for a few seconds, the resulting solution was drawn into a second syringe and injected into the bottom port of the IR cell. The spectrometer had been previously set at the free water vibration at  $1630\text{ cm}^{-1}$ . The absorption at this frequency was then measured as a function of time.

Nuclear magnetic resonance was performed on a Bruker 300 megahertz machine. NMR tubes 5 millimeters in diameter were used after flame drying as described previously. The preparation of the initial solution was identical to that of the coating solution. However, initial experiments indicated that the ethanol solvent would have to be replaced

with a deuterated solvent. To this end, the original solution was placed in a rotary evaporator and the solvent removed. The resulting white powder was redissolved in dry reagent grade toluene; and the solvent was again removed. This time the solvent was replaced with toluene d-8. The solution was removed with a syringe and injected into a dry NMR tube.

Coatings were applied to the silicon substrates by spin coating. However, since the coating solutions were quite hygroscopic, the Headway Spinner, containing a dish of desiccant, was enclosed in a nitrogen purged glove bag (fig. 3.1). The silicon wafer was mounted on the vacuum chuck and the bag closed. The solution was filtered with a 0.2 micron Millipore filter mounted on the end of the syringe. The solution was thus injected through the glove bag onto the stationary wafer. As soon as the wafer was entirely covered with solution, the wafer was spun at the desired speed for thirty seconds. During a second 30 sec. spin, the wafer was exposed to nitrogen saturated with water via a tube extending outside the glove bag. During an additional thirty second spin, excess moisture was allowed to evaporate; and the bag regained its relatively dry atmosphere. After this two step treatment, a subsequent layer could be spun on. After the coating application was complete, the wafers were stored in fluorocarbon containers.

All samples were then coated with a masking agent (black wax) except for a small area. The masked samples were submerged in dilute hydrofluoric acid until the exposed silicon shed the solution evenly. This indicated the complete removal of any oxide layer. Etching was stopped by thorough rinsing of the wafer in water. The mask was removed by washing in acetone, then trichloroethylene, then acetone again, and

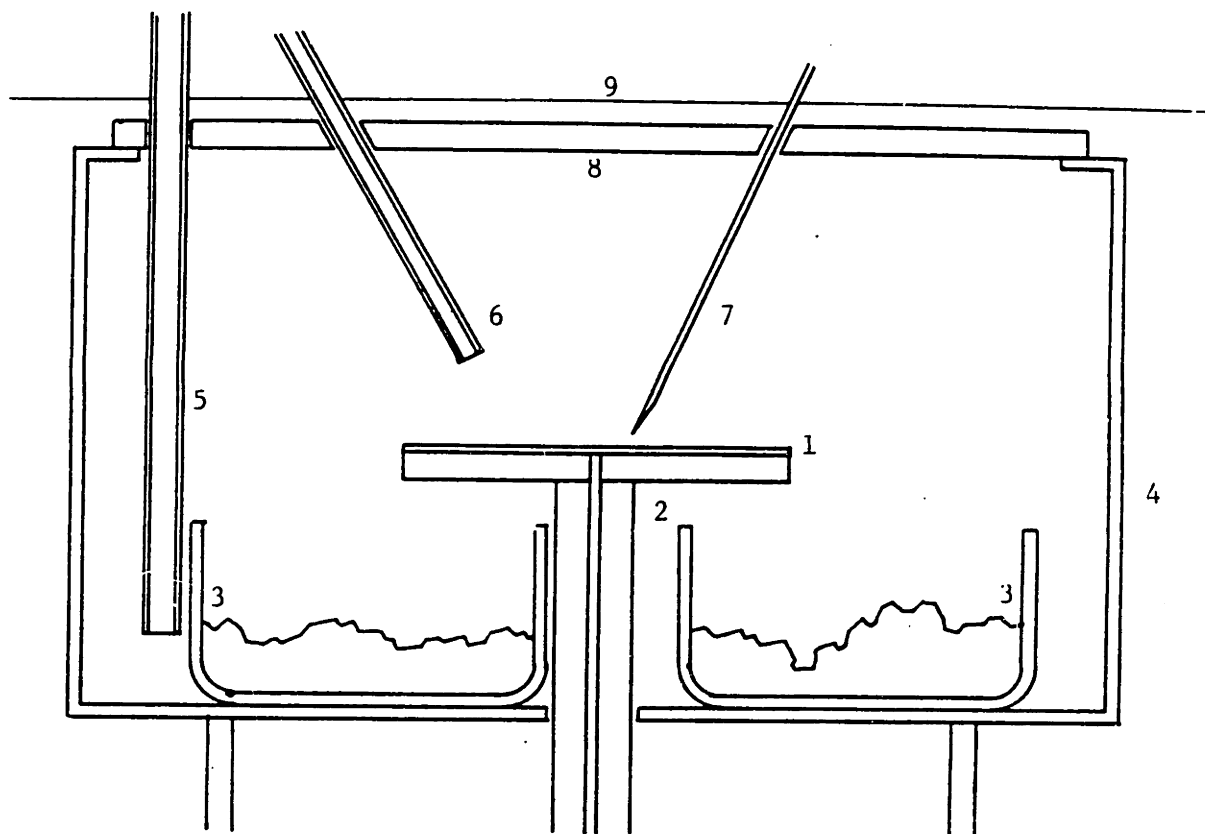


Figure 3.1

Spin coating apparatus showing: (1) silicon wafer substrate, (2) vacuum chuck, (3) petri dishes containing desiccant, (4) spin bowl, (5) tube for injecting dry nitrogen, (6) tube for injecting humidified nitrogen, (7) syringe needle for delivery of coating solution, (8) Lexan cover, (9) glove bag.



finally, methanol. The height of the step resulting from the acid etch was measured using profilometry and ellipsometry.

The coated substrates were fired to densify the oxide. All were fired in nitrogen containing silica muffle furnaces. Some were placed directly into the hot furnaces. Others were placed in cold furnaces and the temperature raised at a known rate to the desired temperature. All samples were removed from hot furnaces after being held at temperature for the requisite time. After firing, the thicknesses of the films were again measured so that the amount of densification could be determined. The samples were prepared for photolithography by a series of washings in trichloroethylene, acetone, and methanol to assure the adhesion of the aluminum gate electrodes to the tantalum film.

Aluminum was evaporated onto the densified oxide in a vacuum of under  $2 \times 10^{-6}$  torr. The thickness of the aluminum layer was roughly 0.3 microns. The samples were subsequently dehydrated at 200 C for 10 minutes immediately prior to spinning on the photoresist. The positive resist (KTI 1370) was spun on for 30 seconds at 3000 RPM. After one minute in air, the samples were moved to a 85 C furnace for 25 minutes to evaporate the solvent. The photoresist was exposed using a Karl Zeuss MJD3 aligner with a black emulsion mask defining the gate electrodes. A portion of the mask pattern appears as figure 3.2. After exposure, the photoresist was developed for one minute in 50% KTI 312 in deionized water, leaving the photoresist pattern intact on the aluminum. The samples were baked at 135 C for 25 minutes to crosslink the polymer layer.

The aluminum between the photoresist regions was removed using PAN etch (table 3.3). This took about 30 seconds in warm etch. The etching

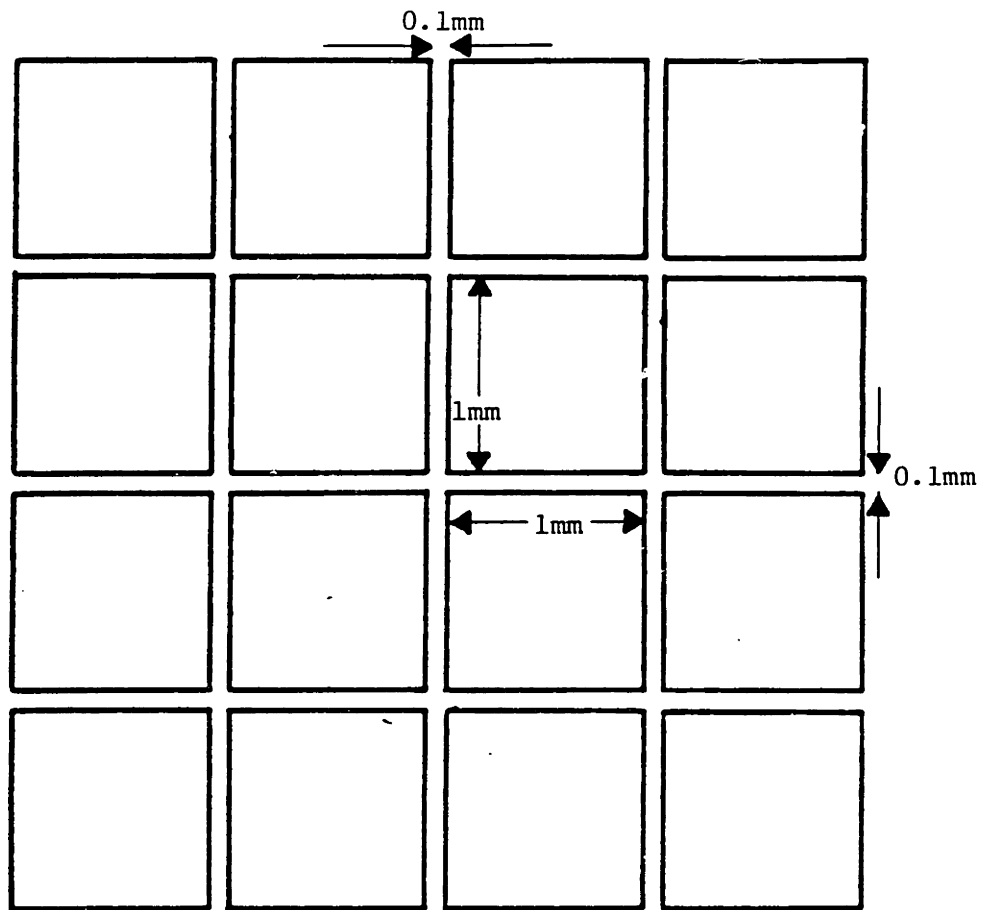


Figure 3.2

Section of mask pattern for definition of the gate electrode. Gates are 1mm squares separated by 0.1 mm spaces.

process was stopped by rinsing in deionized water. The mask was removed using a hot solution of Allied A20 photoresist stripper. The samples were again washed in water, then acetone, trichloroethylene, acetone, methanol, and then blown dry. The wafers were masked on the front with wax, then submerged in hydrofluoric acid to remove the oxide from the back of the wafer. Upon completion, the wax was removed as before and aluminum was evaporated onto the back to provide the rear contact.

Table 3.3.

## PAN etch composition.

Component	Amount
phosphoric acid	80 %
acetic acid	5 %
nitric acid	5 %
water	10 %

Electrical characterization was performed on two systems. The first was an HP 4192A Impedance Analyser interfaced with an IBM PC/XT using software modified from that written by P. Moon and G.M. Choi. The second system utilized was a Hewlett Packard Semiconductor Parameter Test Facility comprised of a 4083A Switching Controller, a 4140B Picoammeter, and a 4275A Multifrequency LCR Meter interfaced with a Hewlett Packard 9236 computer using software modified from that written by P. Whitney. All capacitance-voltage analyses were run at 1 megahertz with an oscillator voltage of 50 millivolts. The bias voltage was scanned in either 0.1 or 0.2 volt increments from +5 to -5 volts for p-doped substrates and from -5 to +5 volts for n-doped substrates. In other words, voltage scans were run from the depletion side of the flat band voltage to the accumulation side as practiced in industry. The

samples were measured in a shielded aluminum box to decrease noise. Immediately prior to each measuring session, the impedance analysis system was calibrated with an open and a short circuit. The open or short was made where the sample would be located so as to make the calibration as close as possible to the same situation occurring in the sample. Direct current leakage was measured using a Hewlett Packard 4140B Picoammeter interfaced with an IBM PC/XT using software written by P. Moon.

After electrical characterization, several samples were examined in a transmission electron microscope (TEM) in transmission mode on a JEOL 200CX, or using reflection high energy electron diffraction (RHEED) on a Phillips 100. All TEM samples were cleaned of the aluminum gate electrodes by immersion in warm PAN etch. Samples to be examined by RHEED were then fixed directly to the sample stage. Coated silicon transmission samples were first dimpled from the back to within 20 microns of the front face using a precision dimpler with one micron diamond paste. They were then ion milled from the back until a perforation appeared (fig. 3.3).

Powders were formed for thermal analysis and sintering experiments by precipitating the actual coating solutions in air at room temperature. The additional moisture necessary to cause precipitation was supplied by the ambient humidity of the laboratory. The solvent was allowed to evaporate at the same time. The powders were further prepared by grinding with a small agate mortar and pestle.

Thermal analysis was carried out with a Perkin Elmer 7/4 controller interfaced with both a TGS-2 thermogravimetric analyser and a DTA-1700 differential thermal analyser. TGA and DTA data were taken in both

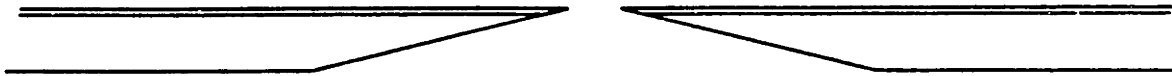


Figure 3.3  
Cross-section of TEM sample. Silicon substrate has been dimpled from the back, then ion milled from the back only, leaving regions of coating exposed.

flowing oxygen and nitrogen. In addition, effluent gasses that were products of chemical reactions and transformations in the powder upon heating were analysed for composition with an IBM System 90 Fourier Transform Infrared Spectrometer (FTIR) as depicted in figure 3.4.

Sintering experiments were carried out on identical powders. Pellets were formed by uniaxially pressing the ground powder to 28% relative density. These pellets were further processed by isostatically pressing at 40,000 psi. to 44% relative density. The resulting samples were sintered to 1000 C under oxygen in a dilatometer so that changes in length could be monitored continuously. Fired and unfired pellets were examined using a Cambridge Scanning Electron Microscope.

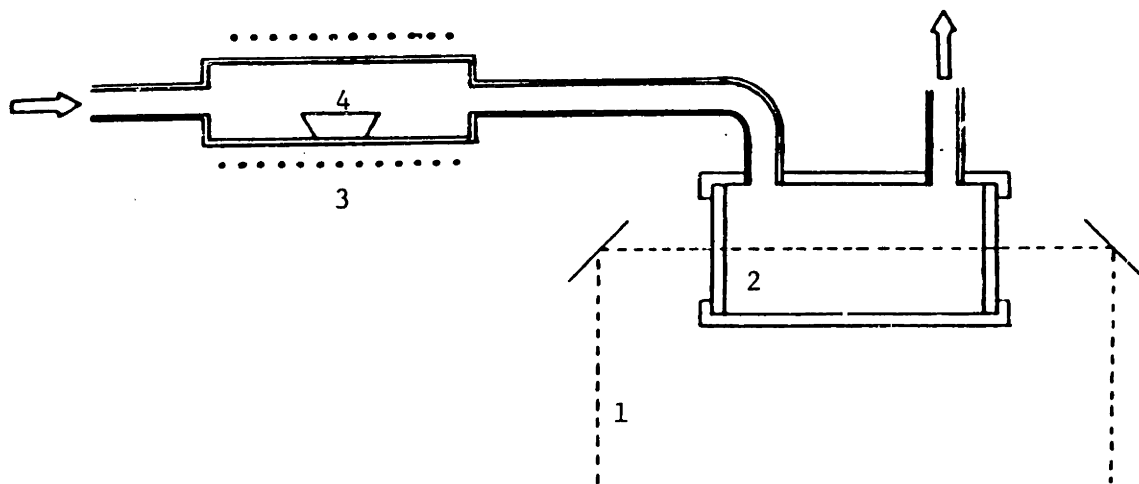


Figure 3.4  
Schematic of FTIR setup for the analysis of effluent gases during a controlled heatup. Figure shows (1) light path, (2) IR transmission cell, (3) furnace, and (4) sample. Gas flow is from left to right.

## Chapter 4. Results and Discussion

As stated previously, the intent of this work is to determine the dielectric properties of gel-derived tantalum thin films. Since the properties of these films may be dependent on processing in previous steps, much attention was paid to early processes in the work. Starting with the coating solutions, the process was monitored through film deposition and firing. Finally, work was done on powders to elucidate possible processes occurring in the films.

### 4.1. Coating solutions

The first step in this work was to confirm some of the results presented in previous works. First, proton NMR was run on the ethoxide in toluene. The spectrum was temperature dependent, showing the lower of the two coalescence temperatures, peak placement and relative intensities identical to those previously reported. The methylene portion of the NMR spectrum (fig. 4.1.1), by revealing three distinct methylene quartets, showed that complexes are formed in solution. Complexation behavior was also evident when a solid alkoxide of a second metal was added to the tantalum ethoxide to generate multicomponent coating solutions. When either magnesium ethoxide or aluminum isopropoxide was added to the tantalum ethoxide, they dissolved completely. As mentioned earlier, magnesium ethoxide is sparingly soluble in ethanol. Aluminum isopropoxide, itself a solid, if reacted



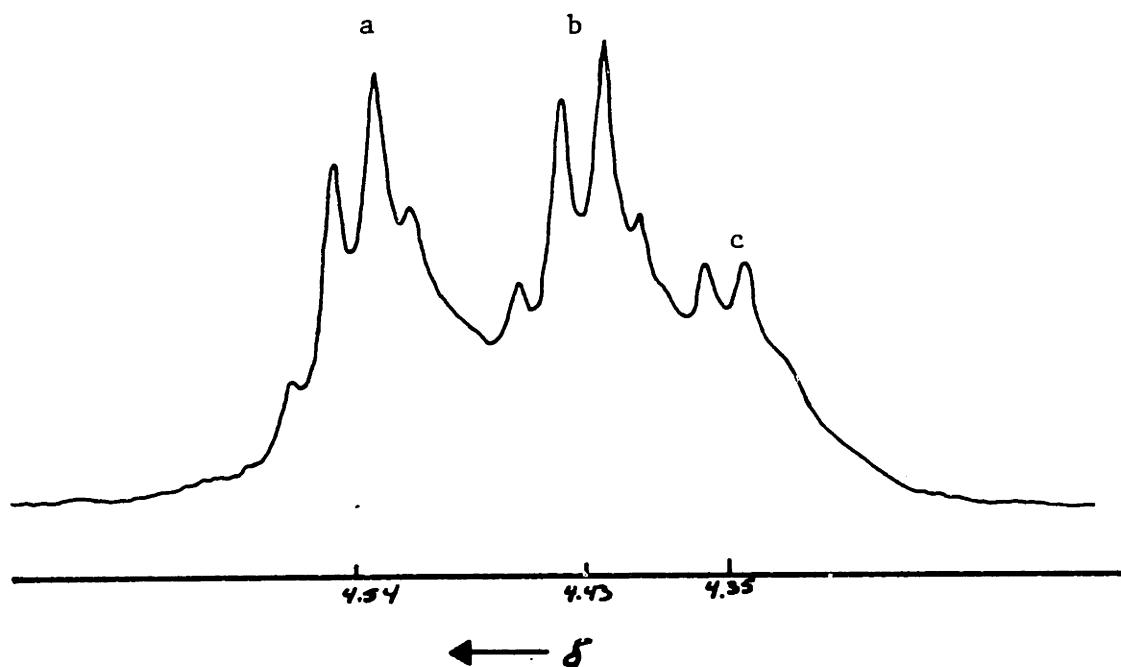


Figure 4.1.1  
Methylene portion of NMR spectrum of tantalum ethoxide  
showing signals originating from (a) equatorial non-bridging,  
(b) axial non-bridging, and (c) bridging ethoxy groups.

completely with the ethanol solvent, forms the ethoxide which is also sparingly soluble in ethanol. The dissolution of these compounds in tantalum ethoxide which subsequently dissolved completely in ethanol is strong evidence for the formation of mixed alkoxide complexes. This qualitatively confirms some of the work of previous investigators [34].

Work was also done to check at what degree of hydrolysis (h) precipitation occurs. In room temperature solutions containing only tantalum ethoxide, water and ethanol, precipitation occurred at a degree of hydrolysis of 1.6. This is the same result as reported by Bradley [34]. The induction time for precipitation depended strongly on the degree of hydrolysis, varying from just a few seconds at  $h=2$  to several minutes at  $h=1.6$ . However, when acetic acid in a 2:1 mole ratio to the ethoxide was added to the ethoxide prior to water addition, precipitation occurred between 24 and 36 hours after mixing at  $h=2$ . Similar results were obtained for additions of 2,4-pentanedione in a 1:1 mole ratio with the ethoxide at  $h=2$ . Solutions containing these agents with a degree of hydrolysis of 1.8 in closed containers remained clear for periods of more than 1 week before finally precipitating.

There are several possible explanations for this delay of precipitation. Acetic acid has been shown to stabilize tantalum sols [15]. More probable for the acetylacetonate is that the complexing agent effectively reduces the functionality of the tantalum monomer. The oxide-alkoxide structures that develop in the presence of this agent would then be sufficiently different from those generated without it so as to favor the oligomers remaining in solution. This has shown to be the case for titanium propoxide in ethanol [83], where replacing two of the covalently bonded propoxy groups and both of the complexed sites

with acetylacetonate causes the monomer to become essentially bifunctional (fig. 4.1.2). This is due to the relative stability of the bidentate acetylacetonate-titanium complex to hydrolysis. According to Flory [49], gelation is not expected when the monomers involved are entirely bifunctional, because  $\alpha$ , as defined earlier, cannot exceed 1. The result is that the forming polymers are linear and do not precipitate out of solution even when the degree of hydrolysis is raised to 40. Gelation occurs only after three hours in this last experiment, with precipitation having been avoided.

Because gelation does occur, the bidentate ligand-titanium bond is not totally inert to water, but hydrolyses at much slower rate than does the ethoxide-titanium bond. As soon as one of the bidentate ligands is removed from the titanium by hydrolysis, the monomer immediately becomes tetrafunctional. It then serves as a branch point so that infinite network formation can occur. The extent to which this can be applied to tantalum is limited. Complexation with three acetylacetonate molecules increases the coordination number to eight [39], and makes the tantalum essentially bifunctional if the metal-ketone bonds were stable to hydrolysis. After the formation of the diethoxytriacetylacetonate in this work, water was added to the yellow compound to bring the degree of hydrolysis to 4. Gelation was not observed, but precipitation did occur roughly 24 hours after hydrolysis. This does not indicate that the tantalum-ketone complex is less stable to hydrolysis as the titanium-ketone complex due to the long time prior to precipitation. However, it does suggest that the structures that form in the case of tantalum are more condensed, and have less organic character than does its titanium analog. The increase in the amount of condensation causes the

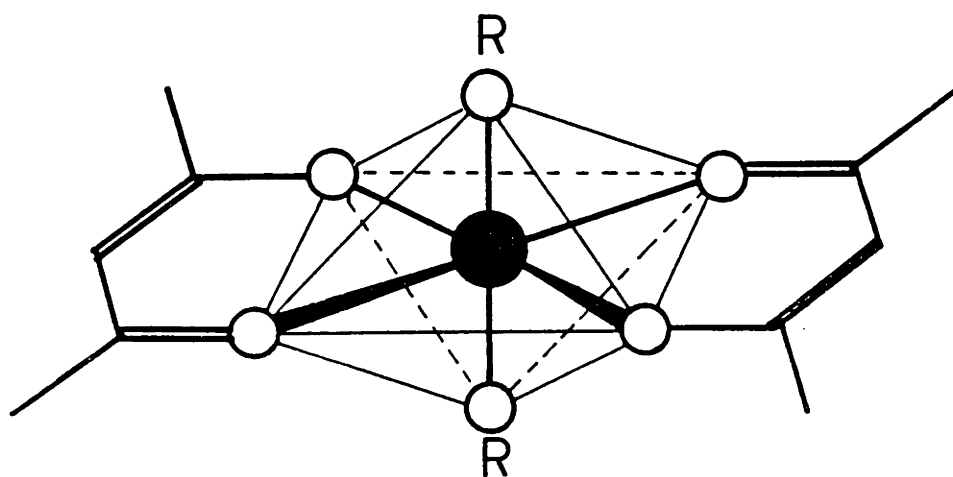


Figure 4.1.2  
Structure of titanium diethoxide diacetylacetonate  
(after [82]).

solubility parameter of the oligomers to deviate farther from that of the solvent. This in turn causes precipitation.

Preparation of the coating solutions followed the previously outlined method for several reasons. First, the water for hydrolysis was added to the ethoxide solution and not vice versa so as to prevent the degree of hydrolysis of any part of the solution from rising above 1.6, thus forming a precipitate.

The hydrolysis and condensation processes were modeled using a computer program to simulate the species that form during the solution phase of the sol-gel process. First, hydrolysis was examined for the condition that condensation was not allowed. Hydrolysis was assumed to be irreversible and first order with respect to each reactant. This means that the probability of the hydrolysis reaction decreases as the number of hydrolysable sites on the alkoxide molecule decreases, i.e.

$$\frac{-d(\text{H}_2\text{O})}{dt} = k(\text{H}_2\text{O}) \quad (\text{OR}) \quad (4.1.1)$$

Figure 4.1.3 shows how the different species develop as a function of time during the simulation for a degree of hydrolysis of 1. Time in this simulation is measured by the number of iterations through which the program has progressed. In each iteration, each species present is allowed to react with all others present, resulting in updated concentrations of those species. Table 4.1.1 shows the results for how many of each species has developed at the end of the simulation as a function of the degree of hydrolysis of the solution. The simulations are all ended when there is less than a 0.01 percent change in all of the species present. As expected, as water is added the hydrolysed monomers increase in concentration at the expense of the lesser hydrolysed species. All simulations resulted in a distribution of

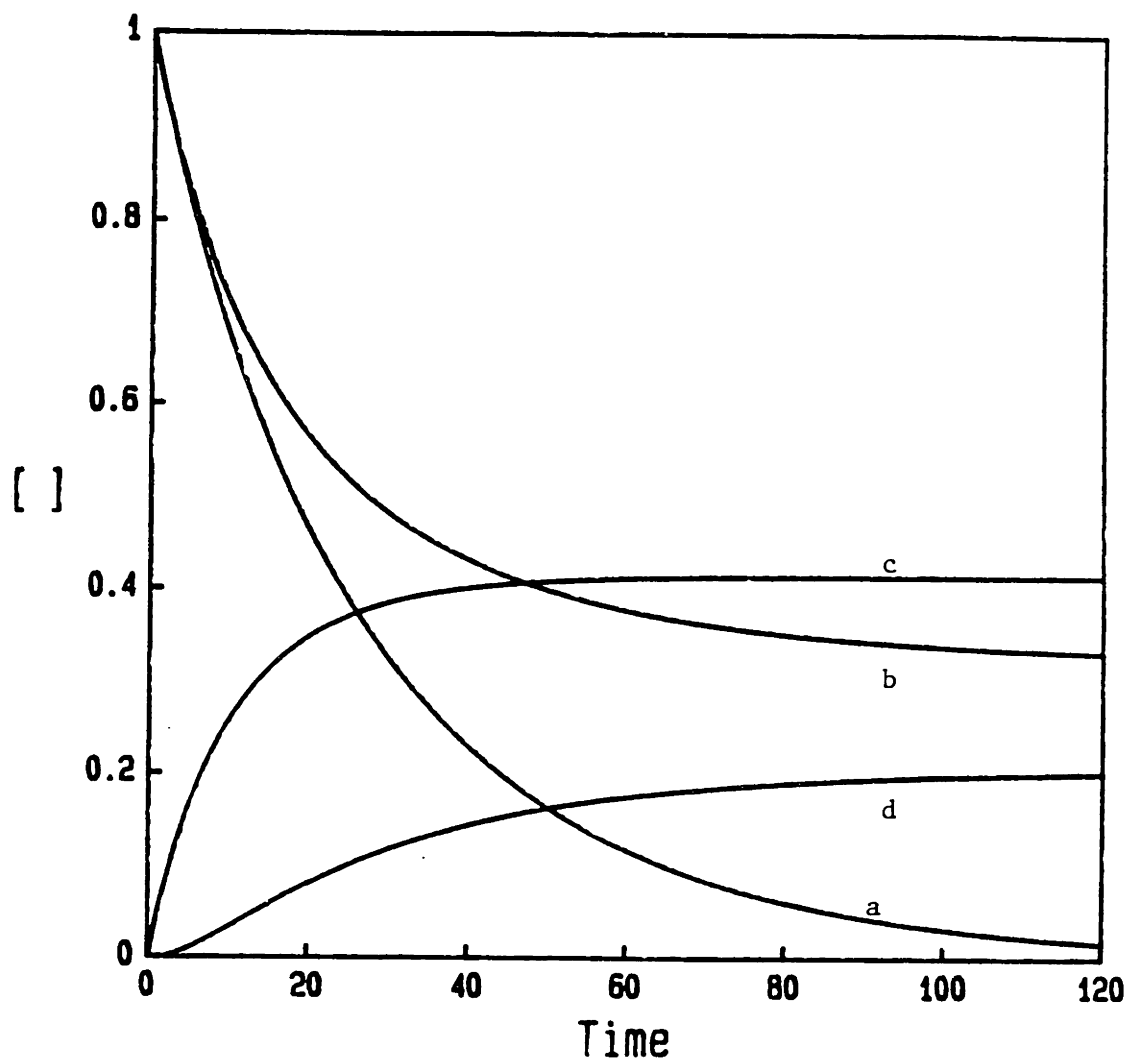


Figure 4.1.3  
Simulation of the development of species during hydrolysis for a degree of hydrolysis of 1. All concentrations have been normalized for initial water (a) and pentaethoxide (b) concentrations of 1. The concentration of (c) the monohydrate and (d) the dihydrate are also shown. Time is in arbitrary units.

species, with the highest concentration of a single species being for the average molecule.

Table 4.1.1.

Fraction of total species with a given number of hydroxyl groups vs. the degree of hydrolysis of the solution assuming no condensation. Blanks indicate fractions less than .001.

h	x in $Ta(OH)_x(OR)_{5-x}$					
	0	1	2	3	4	5
0.00	1	0	0	0	0	0
0.25	.773	.205	.0211	.001		
0.50	.589	.331	.072	.007		
0.75	.441	.396	.138	.023	.002	
1.00	.324	.414	.206	.050	.006	
1.25	.233	.400	.266	.086	.014	
1.50	.164	.363	.313	.131	.026	.002
1.75	.112	.314	.342	.181	.046	.005
2.00	.074	.260	.352	.231	.073	.009
2.25	.048	.205	.343	.278	.109	.017
2.50	.029	.155	.319	.316	.152	.028
2.75	.014	.106	.283	.351	.202	.043
3.00	.007	.070	.234	.361	.259	.069
3.25	.004	.043	.181	.351	.316	.160
3.50	.002	.023	.130	.321	.368	.156
3.75		.012	.084	.273	.406	.224

Condensation was also simulated to follow the increase in the number and weight average molecular weights as functions of the hydrolysis conditions. It should be noted here that the number average degree of polymerization is identical to molecular complexity if one assumes that the hydrolysis reaction does not change the degree of polymerization of the forming oligomer. The assumptions that were made in order to run this simulation are many. The rate of hydrolysis is assumed to be instantaneous compared to condensation and therefore is complete before condensation begins. Water added in the middle of the simulated reaction is introduced between iterations, and is assumed to

totally react by the time condensation resumes. Condensation is assumed to be irreversible and first order with respect to the active sites on the reactants. Both condensation reactions (alcohol and water producing) are possible in this simulation. However, in the absence of any kinetic data, the assumption made is that both reactions occur at the same rate, and that any water produced instantaneously hydrolyses the oligomer that just formed to split off the water. Therefore, the probability of the condensation reaction occurring is a function of the number of hydroxyl group on the oligomers reacting as well as the total number of hydroxyl and alkoxy groups with which the hydroxyl group can react. Ring formation was disallowed. This was done because the formation of a ring is the result of a condensation that does not change the degree of polymerization. The actual shape of each species formed is not followed because the probability that the reaction occurs is a function only of the number of reactive groups on the oligomer. Without ring formation, the number of reactive groups is a function only of the degree of polymerization and the degree of hydrolysis of each individual oligomer. For this reason, the only parameters necessary to follow are the molecular complexity, number of hydroxyl groups and number of alkoxy groups present on each oligomer formed. With these assumptions, an algorithm was developed where every condensation resulted in an increase in the molecular weight of the reacting species in addition to a decrease in the number of hydroxyl groups present on the resulting oligomer.

The results of the condensation simulation confirm the argument stated above, where the water solution must be added to the alkoxide solution to prevent the formation of very high molecular weight species.



Figure 4.1.4 shows the results of simulations where the degree of hydrolysis of the final solution was one half, but where the alkoxide was added to the water solution in two equal parts. In all cases, one half of the alkoxide was added at the beginning of the simulation and the remaining part during the simulation that was varied from the iteration 1 to iteration 31. All simulations were 100 iterations in length. It is clearly shown (table 4.1.2) that the weight average degree of polymerization is strongly impacted by the addition time. This value varies from 7.06 when all of the alkoxide is added at the first step, to 17.8 when the second half of the alkoxide is added at iteration 31 in the simulation. The number average molecular weight is always just less than two at the end of the experiment (fig. 4.1.5) regardless of processing parameters.

Table 4.1.2.

Weight average and number average degrees of polymerization for simulated solutions for different times of addition of the second half of the alkoxide to the water containing solution.

iteration of addition	number average	weight average
1	1.998	7.06
11	1.998	9.01
21	1.997	12.2
31	1.998	17.8

The results are explained in the following manner. As soon as half of the alkoxide is added to the water, the degree of hydrolysis of the resulting solution is one, well above the predicted ratio of 0.625 needed to gel the solution. The number average degree of polymerization rises rapidly, accelerating as the experiment progresses. The shape of this curve is similar to results obtained by Flory on the

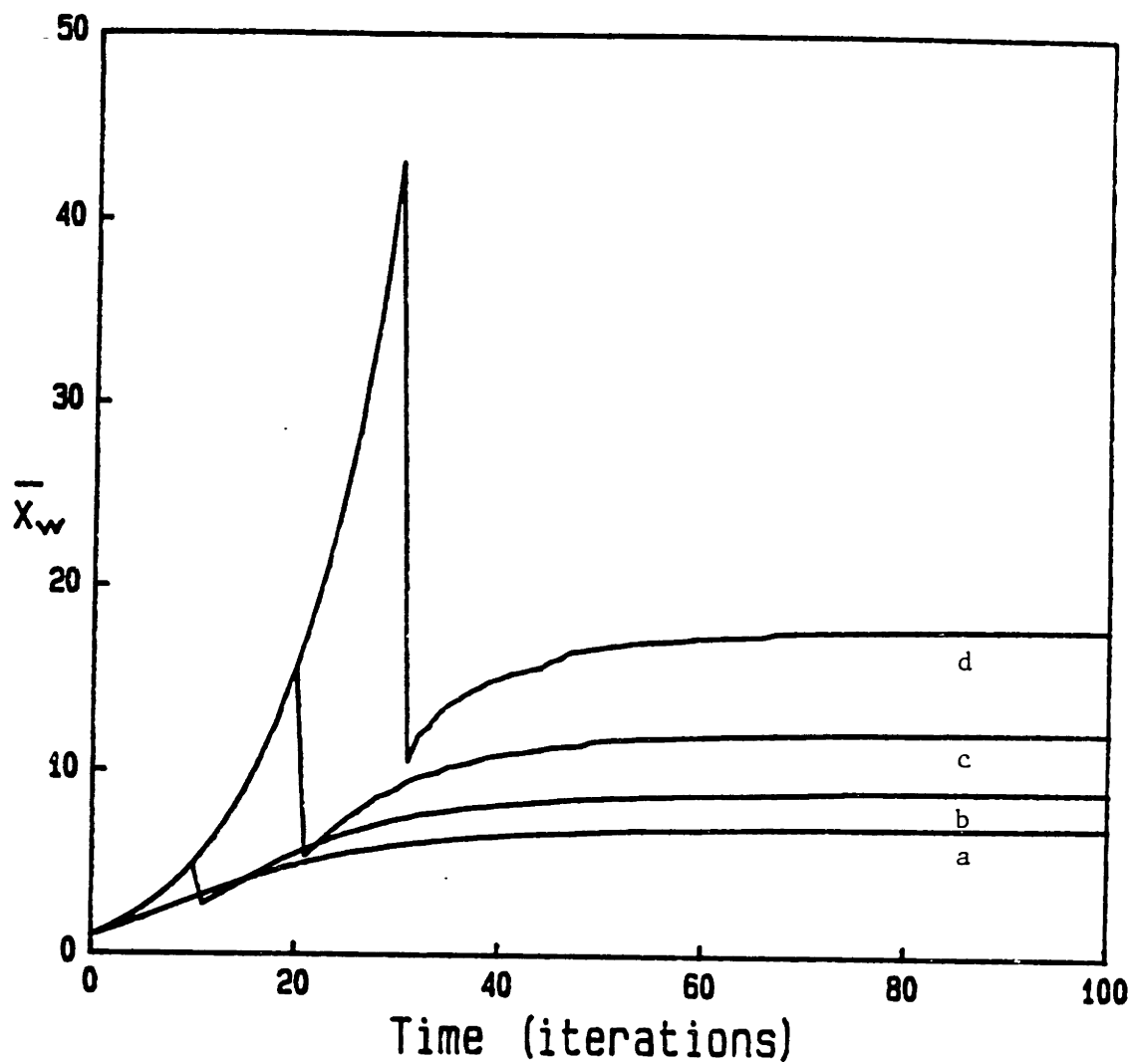


Figure 4.1.4  
Development of the weight average degree of polymerization  
for the case of the addition of the alkoxide to the  
hydrolysis solution. Curves show the second half of  
the alkoxide being added after iteration (a) 0, (b) 10,  
(c) 20 and (d) 30.

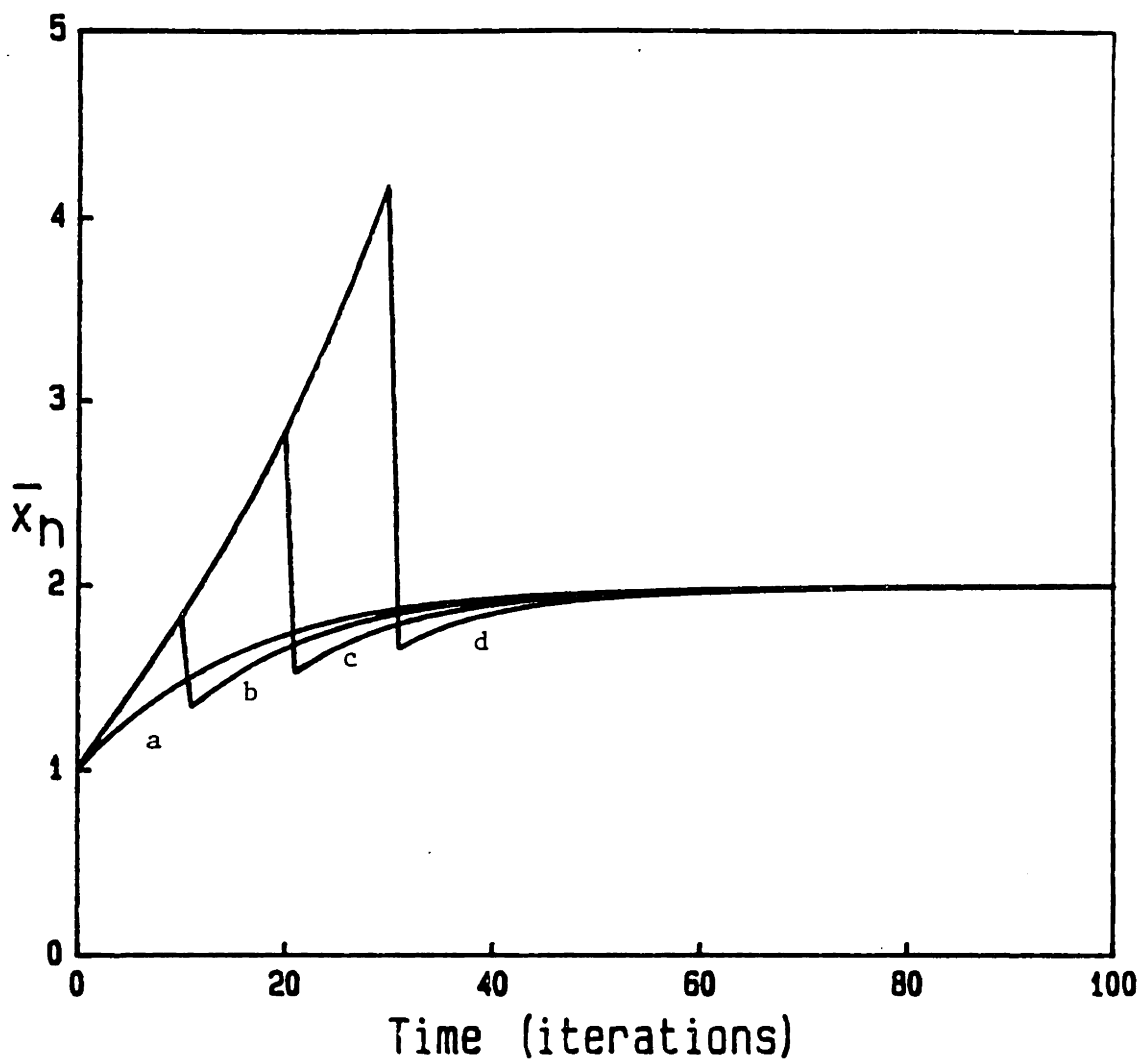


Figure 4.1.5  
Development of the number average degree of polymerization  
for the case of the addition of the alkoxide to the  
hydrolysis solution. Curves show the second half of  
the alkoxide being added after iteration (a) 0, (b) 10,  
(c) 20 and (d) 30.

polyesterification of succinic acid and tricarballic acid (fig. 4.1.6) where the system was seen to gel. Before gelation occurs, the second half of the alkoxide is added. This brings both the number average and weight average degrees of polymerization down immediately. The result of adding the unhydrolysed species is essentially to cap the reactive hydroxyl sites on the oligomers with alkoxide monomers, slowing down the polymerization reaction until it finally stops. The difference between the weight average degrees of polymerization is reflected in the distribution of molecular weights at the end of the simulations (fig. 4.1.7). Here we can see that as the second addition of alkoxide is delayed, the high molecular weight species build up, skewing the weight average degree of polymerization higher.

The results are not so extreme for the case where water is added to the alkoxide solution. These simulations were virtually identical to the previous ones except for the addition of the reactants being reversed. In this regime, if the second half of the water is added after 31 iterations, the weight average degree of polymerization decreases (fig. 4.1.8), but relatively slightly from the 7.06 mentioned before to 5.97 (table 4.1.3). As before, the number average degree of polymerization was just below 2 at the conclusion of the simulation (fig. 4.1.9). Figure 4.1.10 shows that the molecular weight distributions for these four simulations are more similar to one another than the cases where the alkoxide is added to the water solution. Therefore, the distribution of species in the coating solutions is more reproducible if the water containing solution were added to the alkoxide.

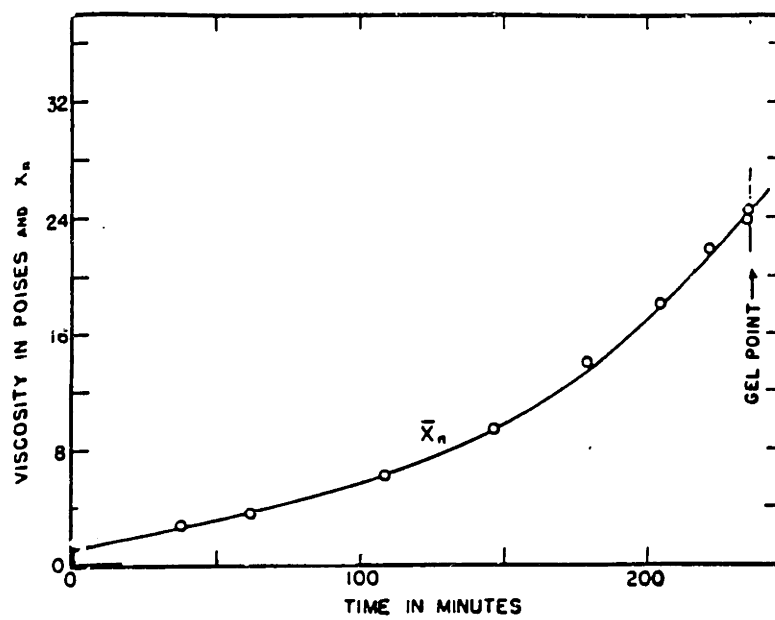


Figure 4.1.6  
Development of the number average degree of polymerization  
for the reaction of succinic acid and tricarballic acid  
(from [49]).

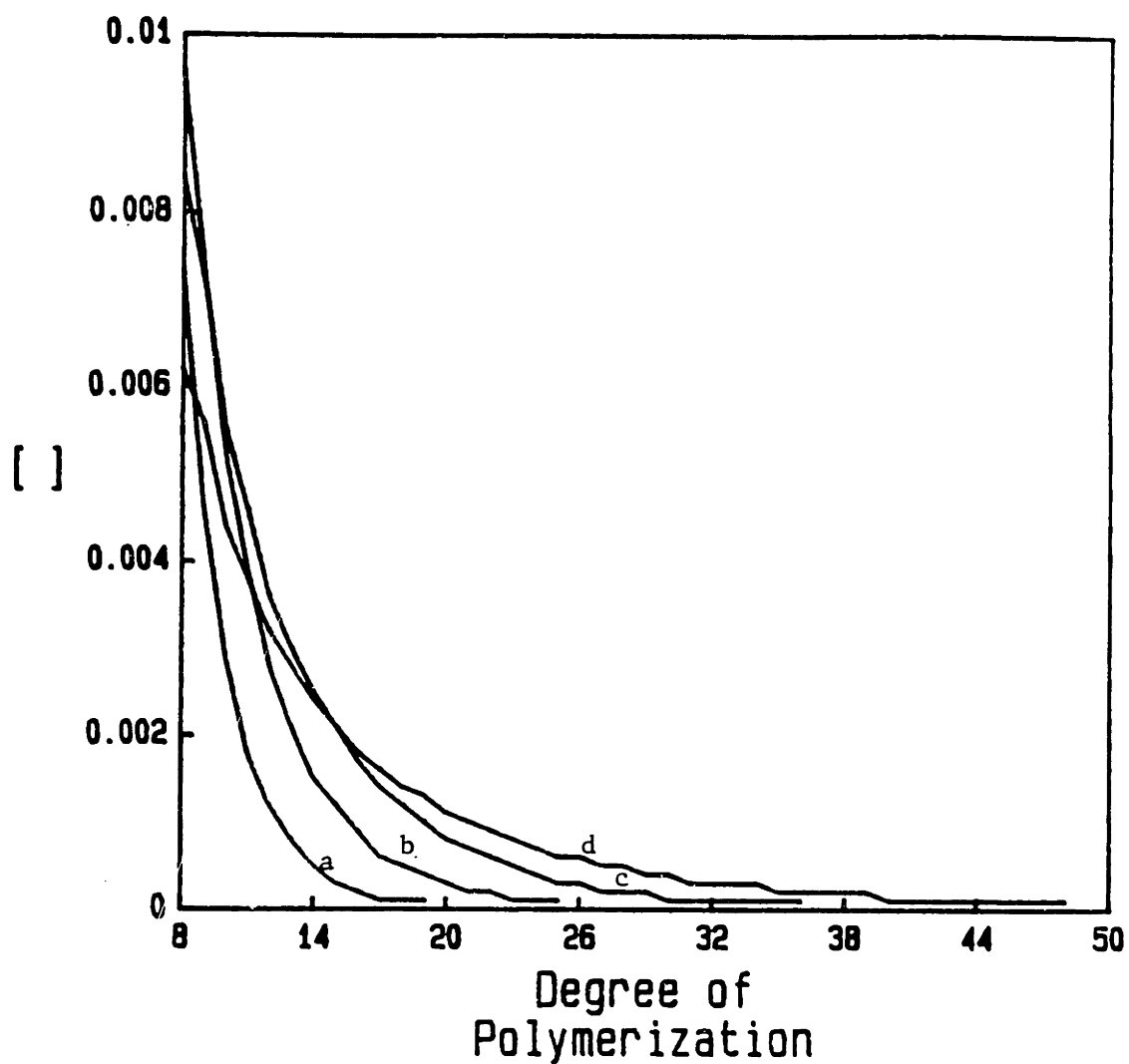


Figure 4.1.7

High molecular weight portion of molecular weight distribution resulting from simulation of polymerization for the case of the addition of the alkoxide to the hydrolysis solution. Curves show the second half of the alkoxide being added after iteration (a) 0, (b) 10, (c) 20 and (d) 30.

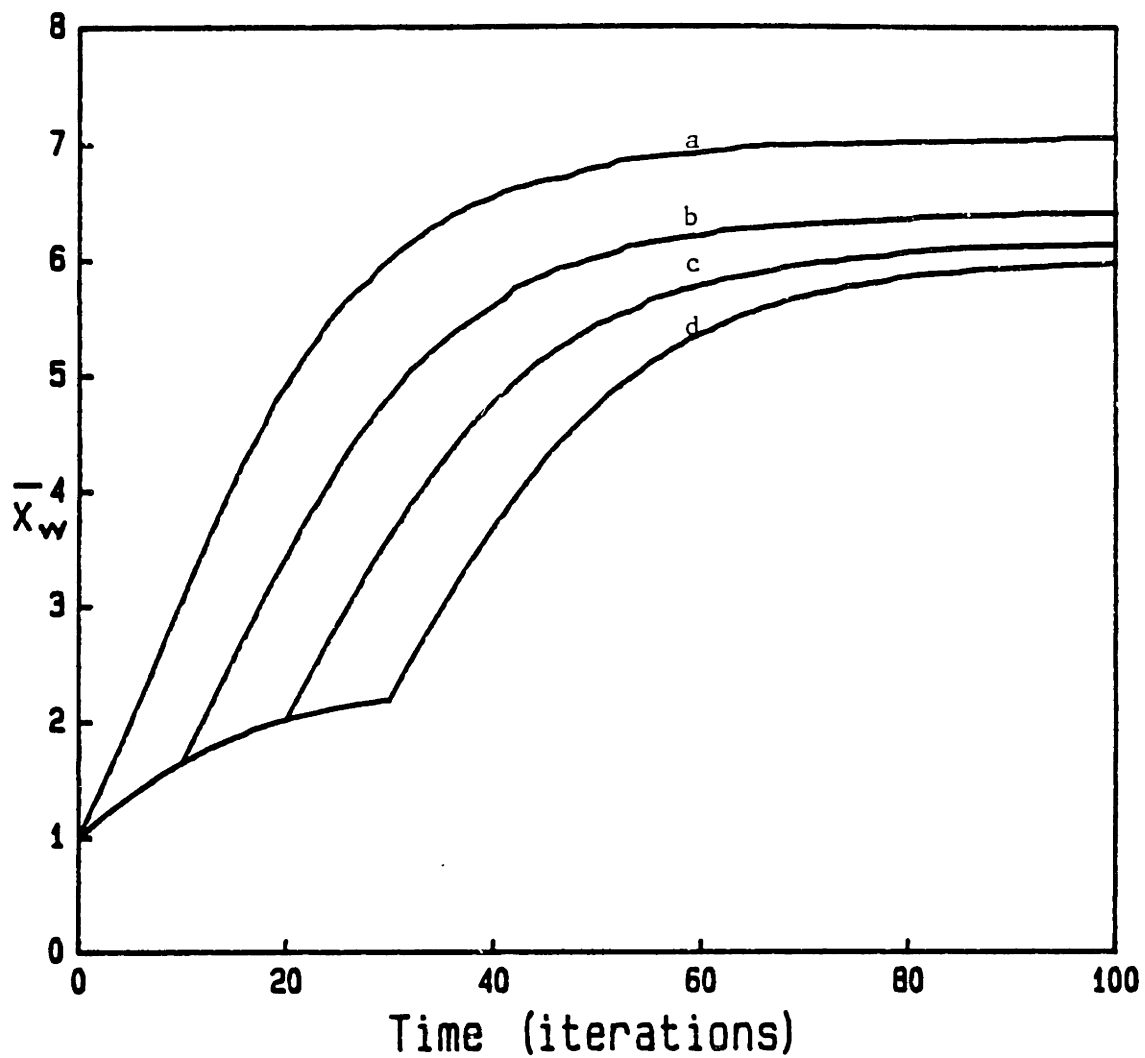


Figure 4.1.8  
Development of the weight average degree of polymerization  
for the case of the addition of the water to the  
alkoxide solution. Curves show the second half of  
the water being added after iteration (a) 0, (b) 10,  
(c) 20 and (d) 30.

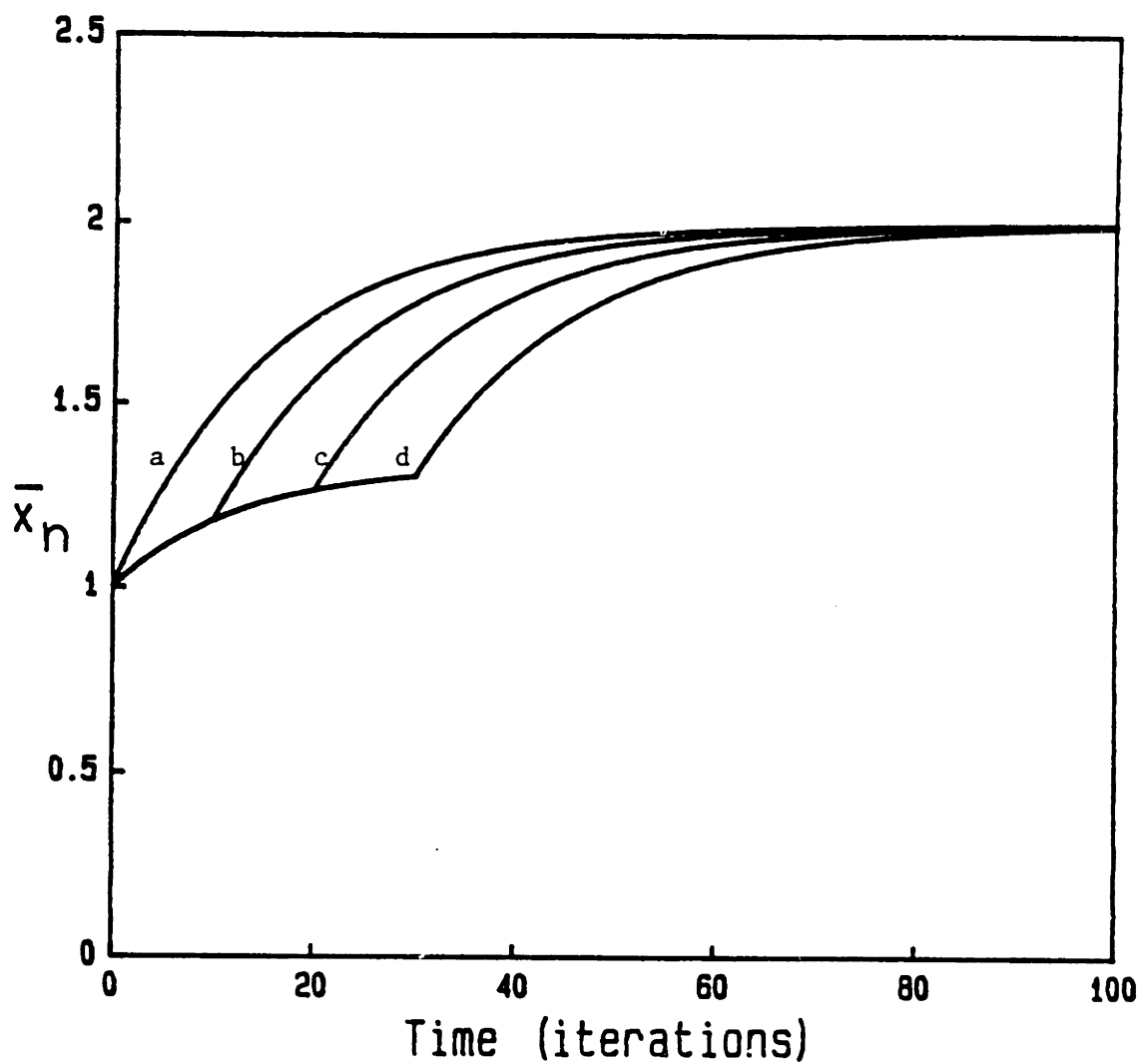


Figure 4.1.9  
Development of the weight average degree of polymerization  
for the case of the addition of the alkoxide to the  
hydrolysis solution. Curves show the second half of  
the water being added after iteration (a) 0, (b) 10,  
(c) 20 and (d) 30.



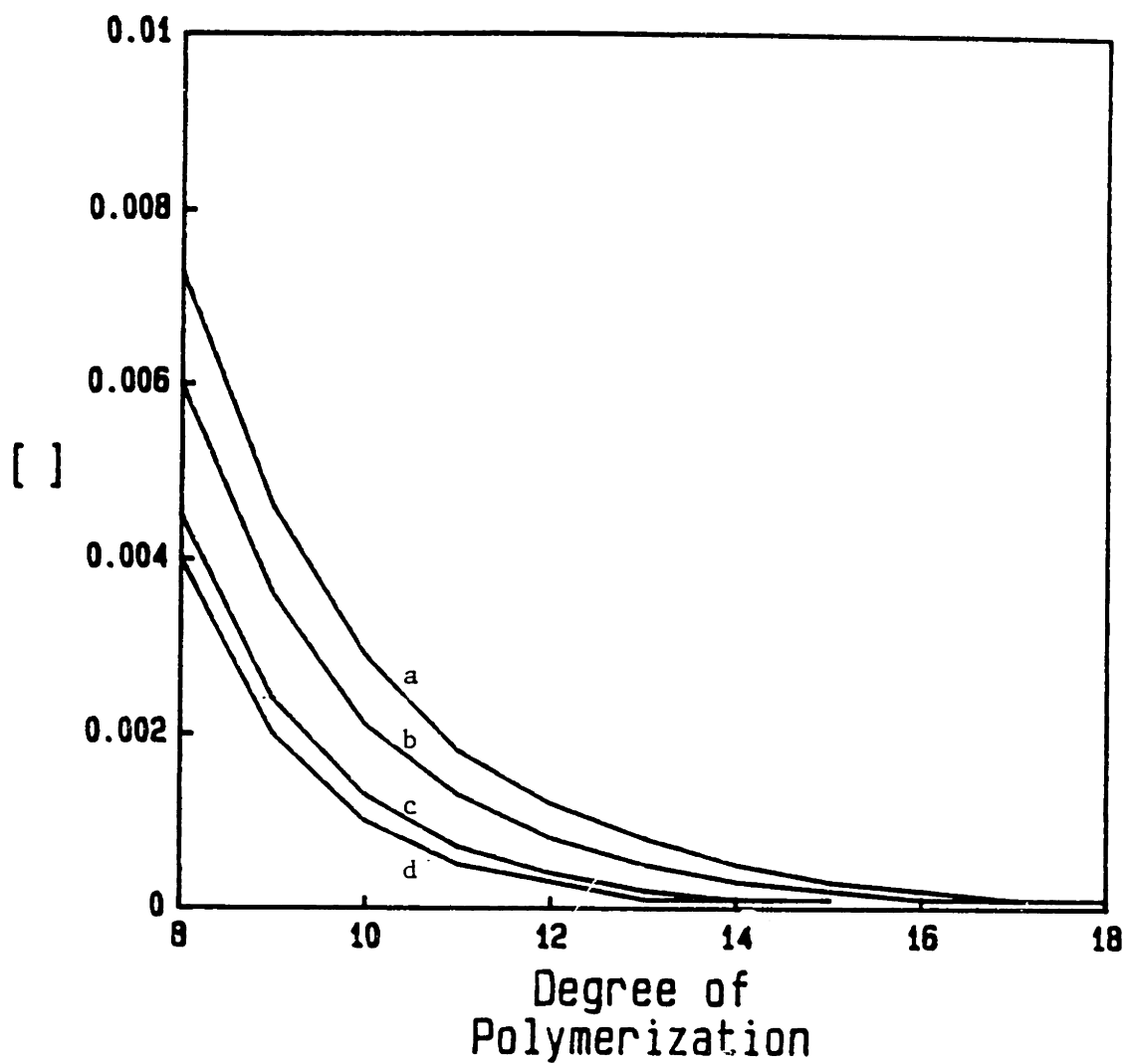


Figure 4.1.10  
High molecular weight portion of molecular weight distribution resulting from simulation of polymerization for the case of the addition of the water to the alkoxide solution. Curves show the second half of the water being added after iteration (a) 0, (b) 10, (c) 20 and (d) 30.

Table 4.1.3.

Weight average and number average degrees of polymerization for simulated solutions for different times of addition of the second half of the water to the alkoxide containing solution.

iteration of addition	number average	weight average
1	1.998	7.06
11	1.998	6.41
21	1.997	6.13
31	1.998	5.97

To check the validity of the simulations, several were run to simulate various degrees of hydrolysis when all of the reactant are mixed simultaneously. Figure 4.1.11 shows the results for the weight and number average degrees of polymerization plotted against the simulated degree of hydrolysis. Also shown are the predictions of Flory for the same quantities. The two are quite close below  $h=0.55$ , at which point the weight average degrees of polymerization diverge rapidly. This is due to Flory's model system rapidly approaching gelation. This comparison indicates that the condensation simulations closely approximate those of Flory, and are valid given the assumptions made.

In the actual coating solutions, the water bearing solution is slowly added to the ethoxide to allow for complete mixing during hydrolysis and condensation. If water were added quickly so as to make mixing less adequate, it might be possible for the ratio of water to alkoxide to locally exceed 1.6, causing precipitation. Since hydrolysis occurs very quickly in this system (see next section), mixing must be done very quickly relative to the speed of addition and reaction. Since reaction is effectively instantaneous, addition must be slow. Adding

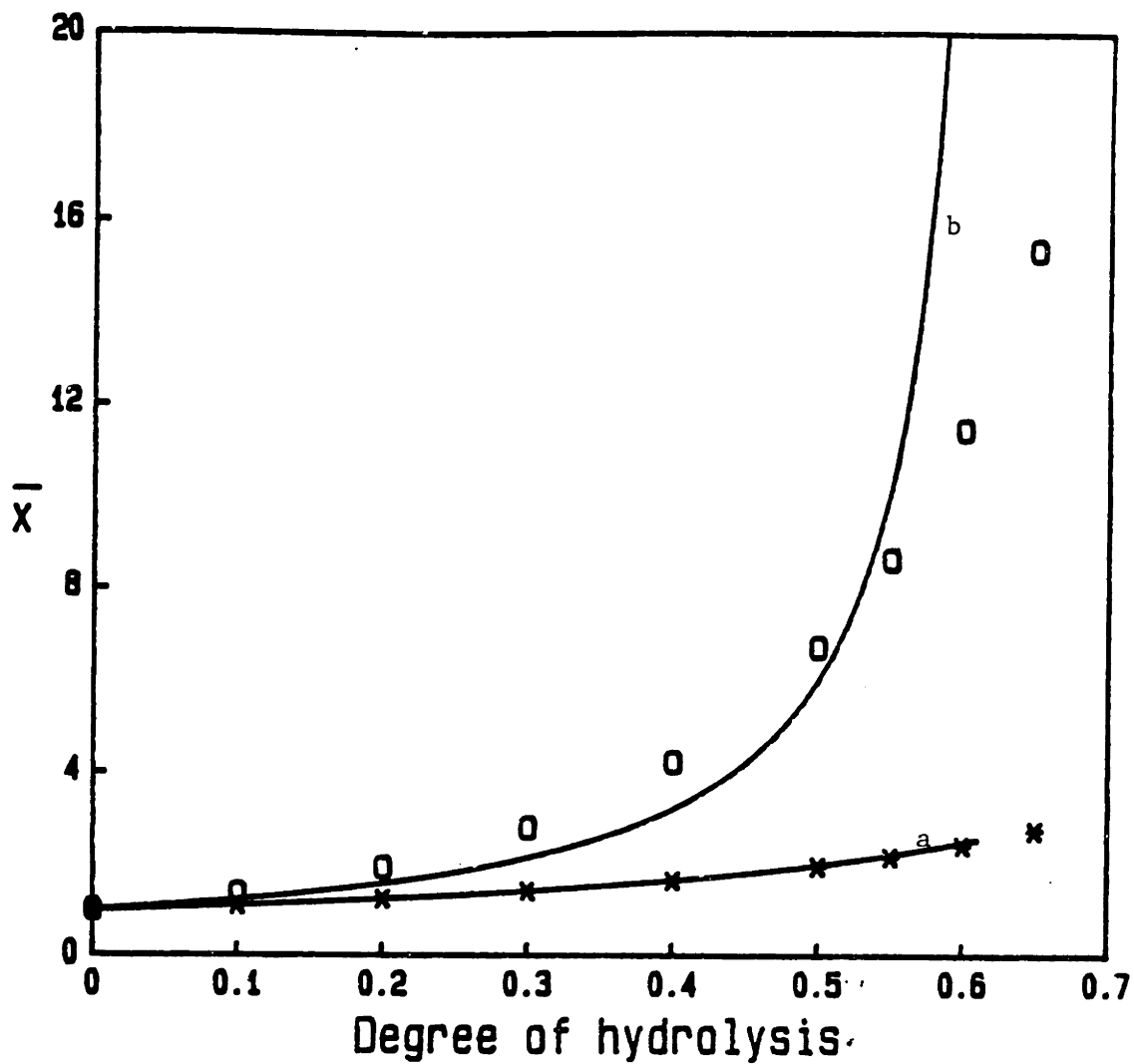


Figure 4.1.11

Number (\*) and weight average (□) degrees of polymerization of simulated polymerization reactions as a function of the degree of hydrolysis. Also plotted are the number (a) and weight averages (b) predicted from Flory Gelation Theory.

the water slowly and in a very dilute form allows adequate mixing of water into the ethoxide, and also permits the partially reacted species to be well dispersed in the solution while additional water is being added. The best method for this involves the in situ generation of the water for hydrolysis. The simplest example is the addition of an organic acid to the alcohol solvent, (e.g. adding acetic acid to ethanol). The reaction between these two species results in the formation of water and ethylacetate, which may be easily removed during drying due to its high volatility. However, the addition of the acid may complicate matters. Altering the pH of the solution may change the reaction kinetics and structures that develop as observed for silica systems. In addition, it will stabilize any sol formed, as mentioned previously in conjunction with acetic acid. This makes the detection of precipitation more difficult. For these reasons, this option was not pursued.

Infrared spectroscopy of the oligomers in ethanol showed no free water after the reaction was complete. In addition, trying to follow the magnitude of the free water peak as a function of time indicated that hydrolysis was quite rapid. In fact, it was so rapid that the free water had been totally consumed by the time the solution could be loaded into the spectrometer cell, which took several seconds. In a separate experiment, the ethanol was removed from the oligomers by rotary evaporation under nitrogen. The white powder was redissolved in toluene and examined with the IR spectrometer. There was no absorption band due to residual hydroxyl groups, indicating that condensation was complete. This supports the assertions of Bradley based on his ebulliometry work. The possibility exists that concentrating the oligomers in the evaporating solution forced the condensation reaction to go to

completion if it had not already. However, one must note that this process is much like what occurs during the drying phase of the coating application, and provides insight into the condition of the dry film.

The latter solution was also examined using proton NMR. The methylene portion of the resulting pattern (fig. 4.1.12) shows that the peaks due to the methylene protons at 204 K are less distinct than they were in the unhydrolysed sample. The room temperature pattern, however, when compared with the lower temperature spectrum shows that the peaks move and change shape as the temperature is decreased. Therefore, there is some motion occurring within the oligomers at room temperature that tends to average the positions of the alkoxy groups. The nonbridging methylene quartets in the unhydrolysed sample have moved closer together, now overlapping so that the signal appears to be a sextet located at the center of where the two quartets used to be, evidence that there no longer are distinct alkoxy sites in the oligomer. In addition, every one of the peaks has a shoulder associated with it at low temperatures, possibly indicating the different alkoxide monomers in chain end, chain, and branch point configurations. The signal from the bridging ethoxy groups is still visible, still in roughly a 1:4 ratio to the nonbridging ethoxy sites. This is evidence that there is still much complexation present, either within the oligomer chains, or between them. This is in contrast to the proposed bilinear chain structure, which contains too few bridging ethoxy groups. It should also be noted that even at this fairly low degree of hydrolysis, there are no peaks corresponding to totally unreacted ethoxide monomers or dimers. This indicates that all of the original ethoxide has been incorporated into the oligomers.

Based on these observations, the oligomers produced in these

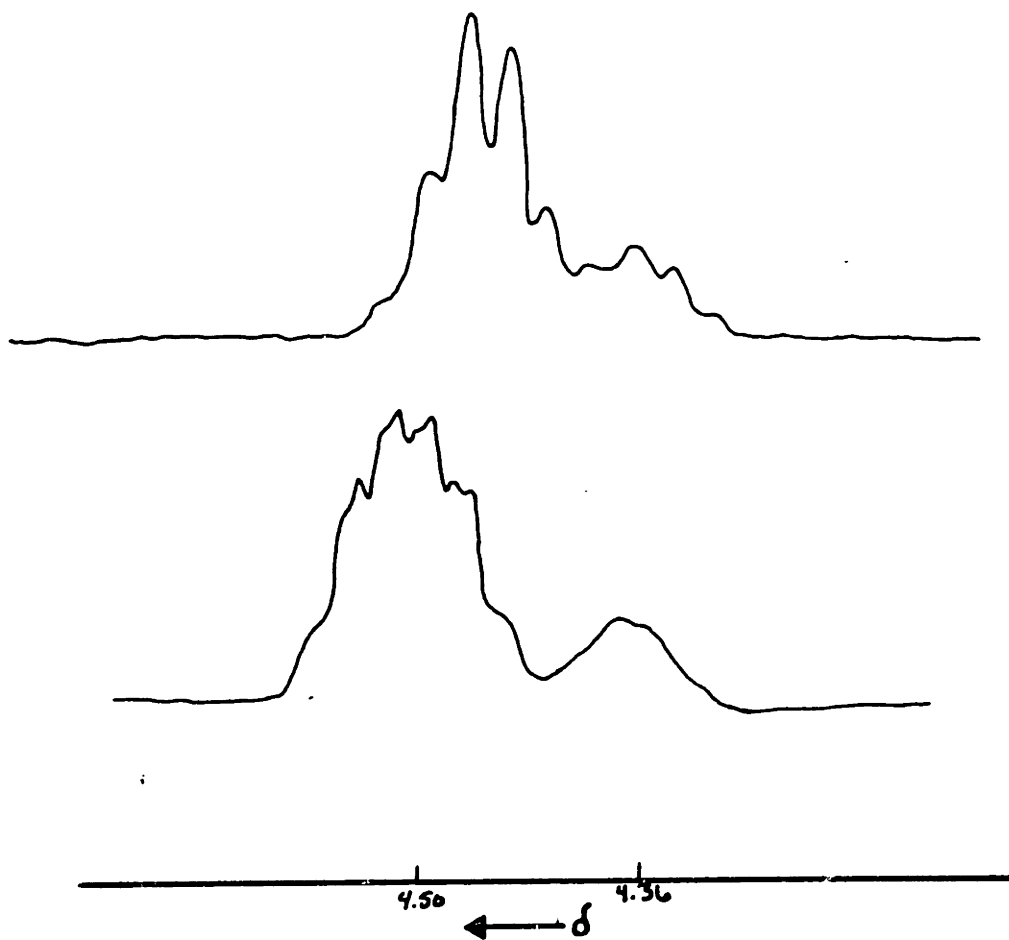


Figure 1.12  
Methylene portions of the NMR spectra of tantalum  
oxide ethoxide at (a) 298 K and (b) 204 K.

experiments have randomly polymerized structures, much as a similar organic polymer might. It should be noted, however, that details of the oligomer structure may be highly dependent on the reaction conditions, e.g., solution temperature, solvent nucleophilicity and precursor concentration. However, under the conditions studied, the oligomers in solution appear to be random in structure, and are made of closely connected rings.

#### 4.2. Coating application

Coatings were applied by covering the surface of the previously cleaned or cleaned and oxidized silicon wafers with between one half and three quarters of a milliliter of partially hydrolysed alkoxide solution prepared as outlined in the experimental techniques section. The viscosity of the coating solutions was not visibly different from that of ethanol. The wafer was then spun at the desired rate for 30 seconds. The resulting films often appeared to be colored due to an optical interference pattern appearing on the surface. During exploratory work in the late winter and early spring, coatings were applied in the ambient laboratory atmosphere. However, we found that as the year progressed, precipitation of particles in the coating solution as it sat on the substrate became a problem. Precipitates in the coatings gave them a pale blue appearance and scattered laser light very effectively. This effect made ellipsometry impossible. We hypothesized that this effect was due to a reaction between the coating solution and humidity in the ambient laboratory atmosphere.

In order to study the effect of humidity, several carbon covered transmission electron microscope grids were dip-coated with tantalum

oxide-ethoxide solutions. One was allowed to dry under dry nitrogen. A second was dried in the laboratory environment in the late spring. A third was hung within one centimeter of the surface of room temperature water in a half filled Erlenmeyer flask. After drying, the grids were examined in the TEM with 100 kilovolt electrons. Before going further, it should be noted that the films were affected by the electron beam. Unsupported films were seen to shrink and splinter upon exposure to the 100 KV electrons. Supported films were also seen to shrink, although not as much. The micrographs presented here represent areas that have had minimum exposure to the beam. These micrographs show that films dried without water present were fairly uniform in structure (fig. 4.2.1). However, films dried in humid air or over water were full of precipitated spherical particles (fig. 4.2.2). The more humid the drying environment, the more particles were produced. The particles were relatively uniform in size, averaging roughly 150 nm in diameter. Many of the particles were necked together due to their having aggregated during their formation. The oligomers still in solution then condensed onto these structures, resulting in the formation of the neck.

The precipitation is due to the fact that several processes can occur while solvent is being removed from the film. These include the increase in concentration of oligomers in the disappearing solvent and additional hydrolysis and condensation from water dissolving in the coating solution before it has completely dried. These two processes can occur simultaneously or sequentially, with either evaporation or hydrolysis/condensation happening first. In a hypothetical case where evaporation were to be prevented completely but water was allowed to dissolve into the coating solution from the atmosphere, particles would be sure to form after the degree of hydrolysis rose above 1.6. As the





Figure 4.2.1  
Transmission electron micrograph of tantalum oxide gel  
on carbon substrate. The gel was dried in a non-humid  
atmosphere. Scale bar is 10 nm.

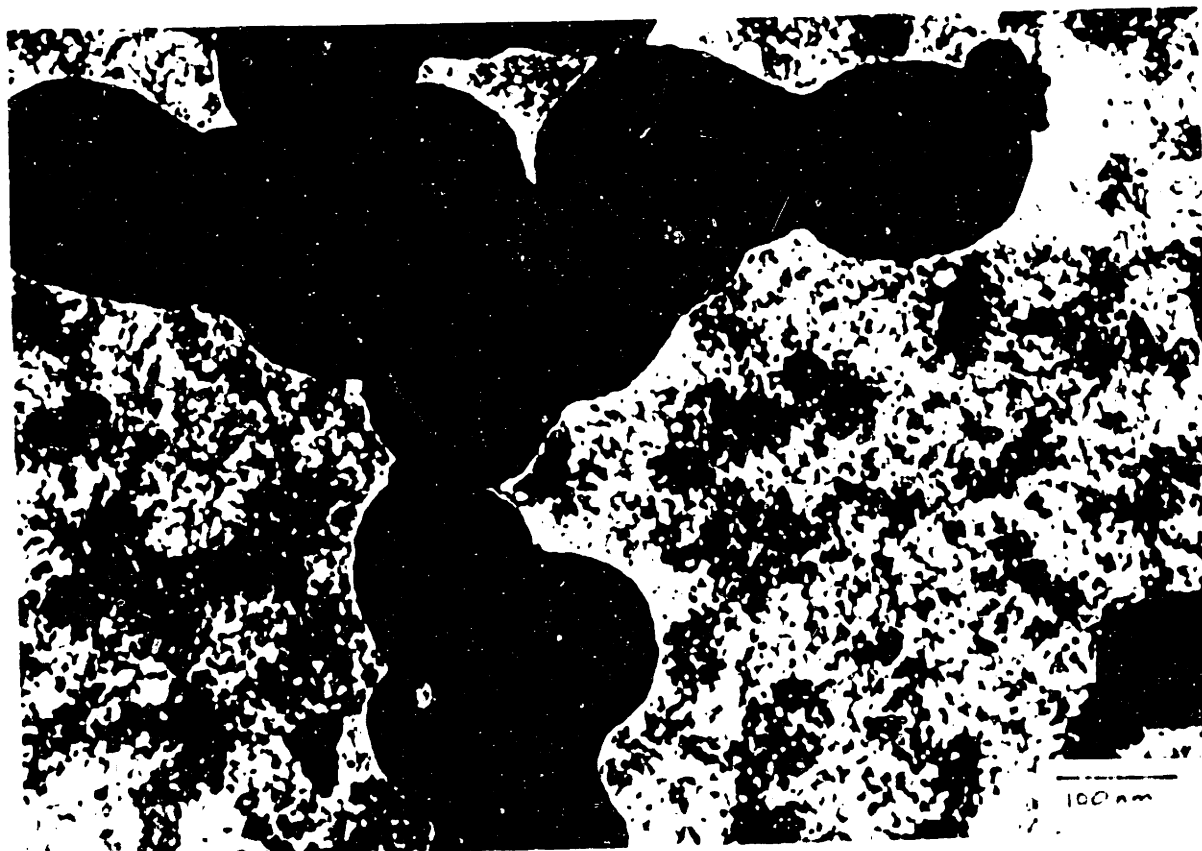


Figure 4.2.7  
Transmission electron micrographs of tantalum oxide gels on  
carbon substrates. These gels were dried in a humid  
environment. Scale bar is 100 nm.

solvent was then removed, the particles would settle onto the substrate. However, if evaporation were to occur first, it would leave the slightly condensed oligomers on the substrate. Moisture then introduced would cause crosslinking between the oligomers. These two scenarios are depicted in figure 4.2.3. For this reason, all subsequent coatings were applied in a dry atmosphere using the previously described apparatus so as to ensure the evaporation of the solvent before additional hydrolysis could occur.

Coating thickness was measured on single layer coatings as a function of spin speed, alkoxide concentration, and radial position on the wafer. All of these experiments were performed on the same day with identically treated wafers to minimize the effect of changes in humidity. Coatings were quite uniform in thickness as a function of the radius of the wafer. Table 4.2.1 shows the thickness of the coatings measured in the center and within 0.5 cm from the edge for several spin speeds. This shows that variations in thickness from the center to the edge of the wafer were routinely less than 2 percent. The data also indicate that the thickness was inversely proportional to the square root of the spin speed in rpm (fig. 4.2.4). The data in table 4.2.2 show that the concentration of oligomers in the coating solution was found to be proportional to the thickness of the resulting film for concentrations up to 5 weight percent oxide in solution (fig. 4.2.5). Both of these relations are widely known throughout the coating industry [55, e.g.] especially in relation to the spin coating of polymeric photoresists. These characteristics have also been shown to apply to colloidal systems [15]. From these data, it has been demonstrated that ethoxide derived tantalum coatings can be applied uniformly and controllably in dry environments.

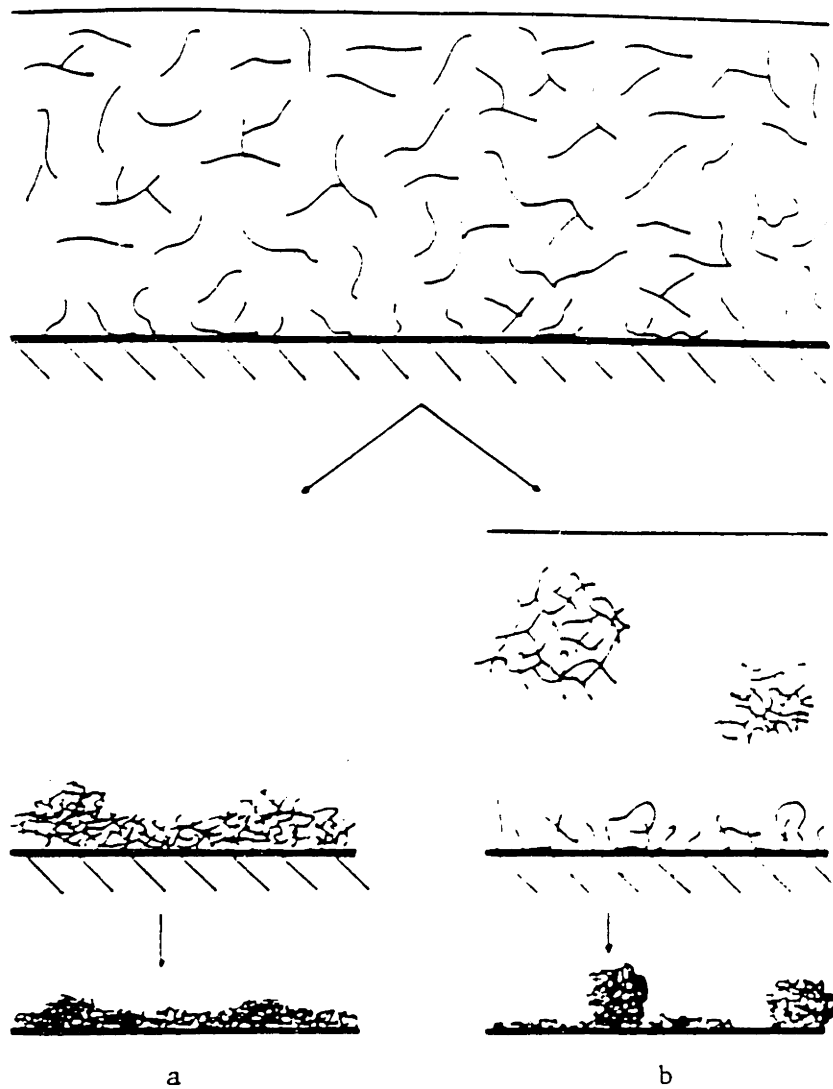


Figure 4.2.3  
 Schematic of the development of gel textures based on differences in the drying atmosphere humidity. Left side shows the removal of solvent before additional hydrolysis and condensation is allowed. Right side shows the addition of water before the solvent is removed.

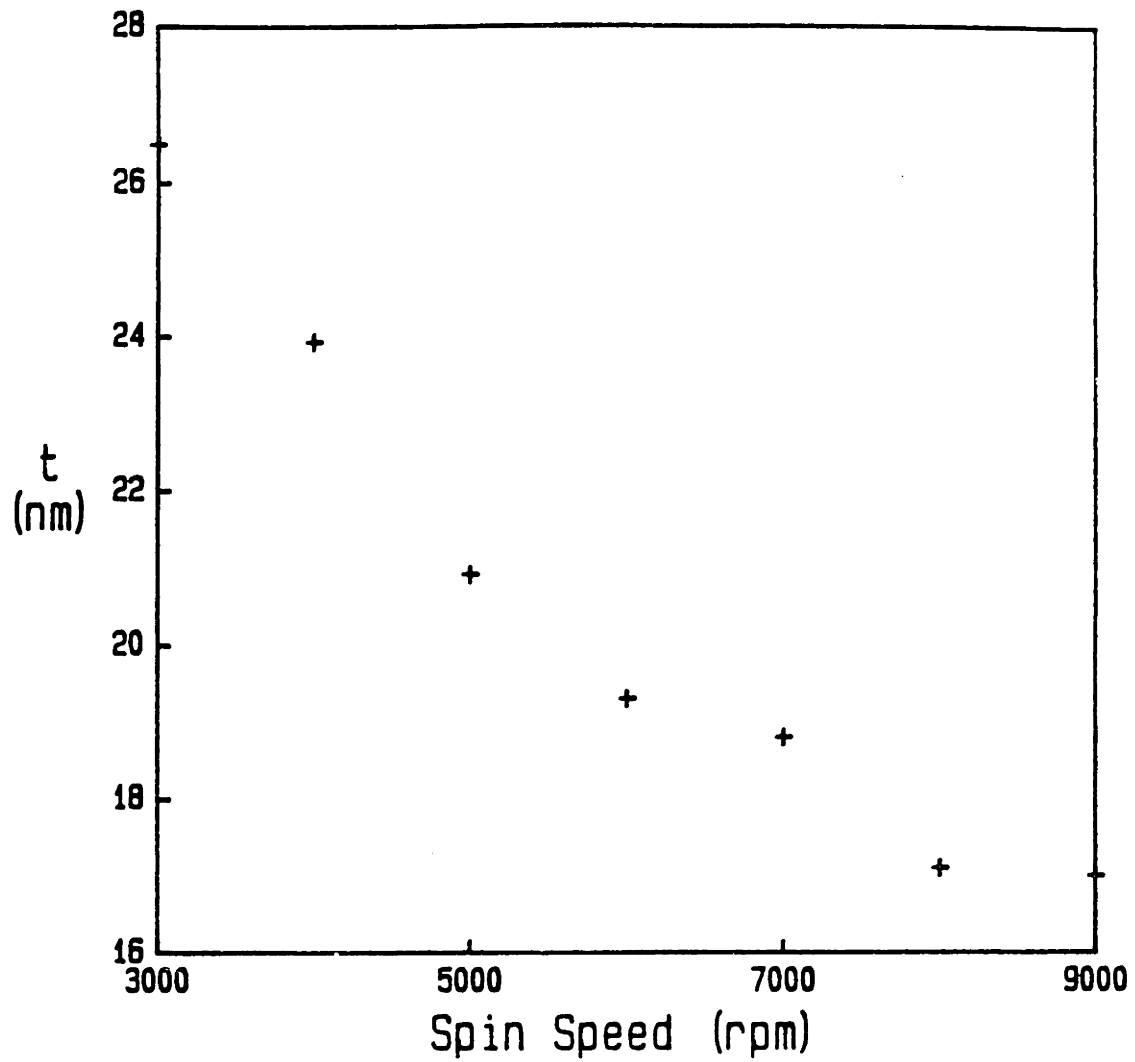


Figure 4.2.4a  
Thickness of the undensified tantalum gels as a function of the substrate spin speed. Coating solutions were 2.5 weight percent equivalent oxide.

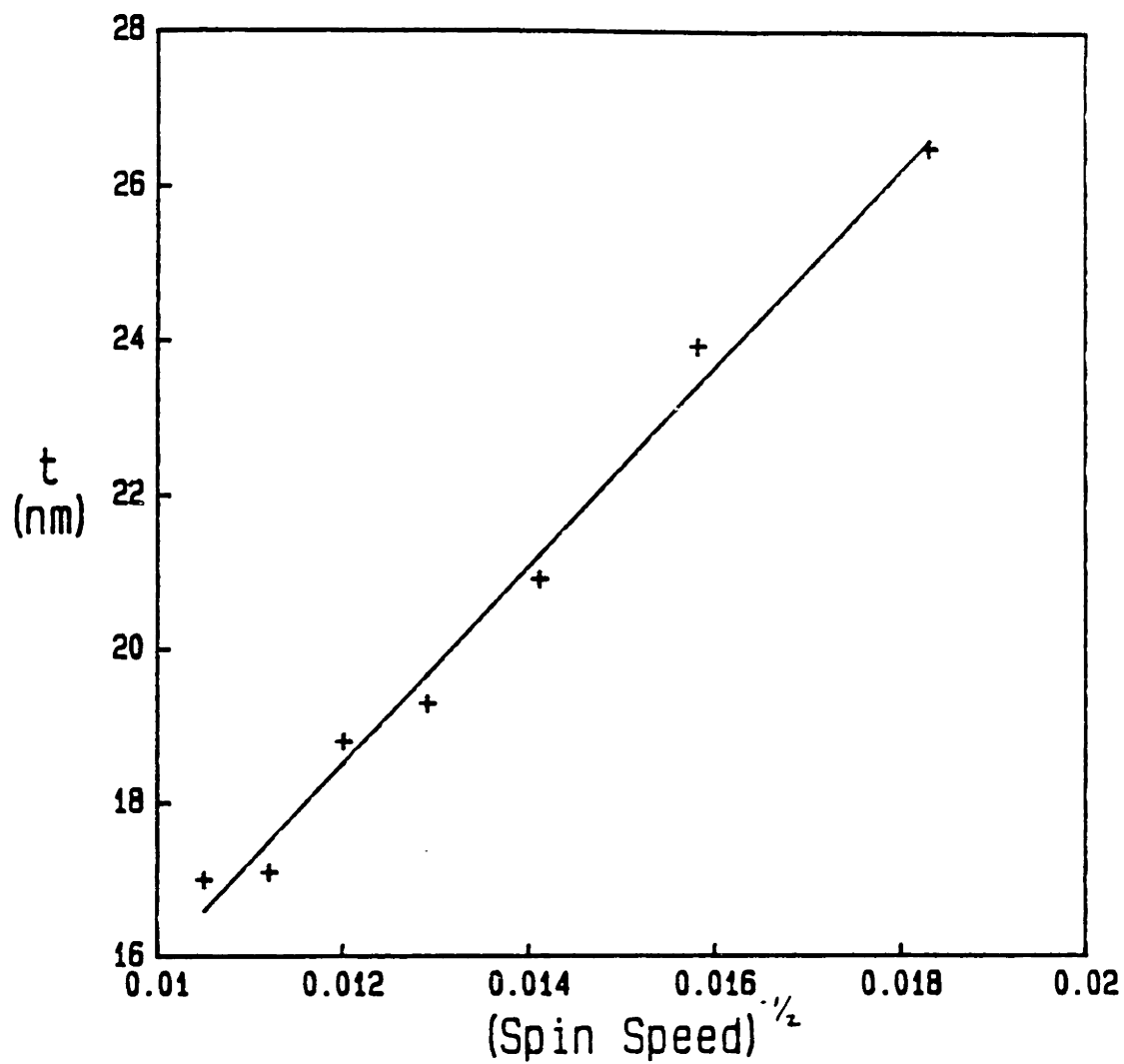


Figure 4.2.4b  
Thickness of the undensified tantalum gels as a function of the inverse square root of the substrate spin speed. Coating solutions were 2.5 weight percent equivalent oxide.

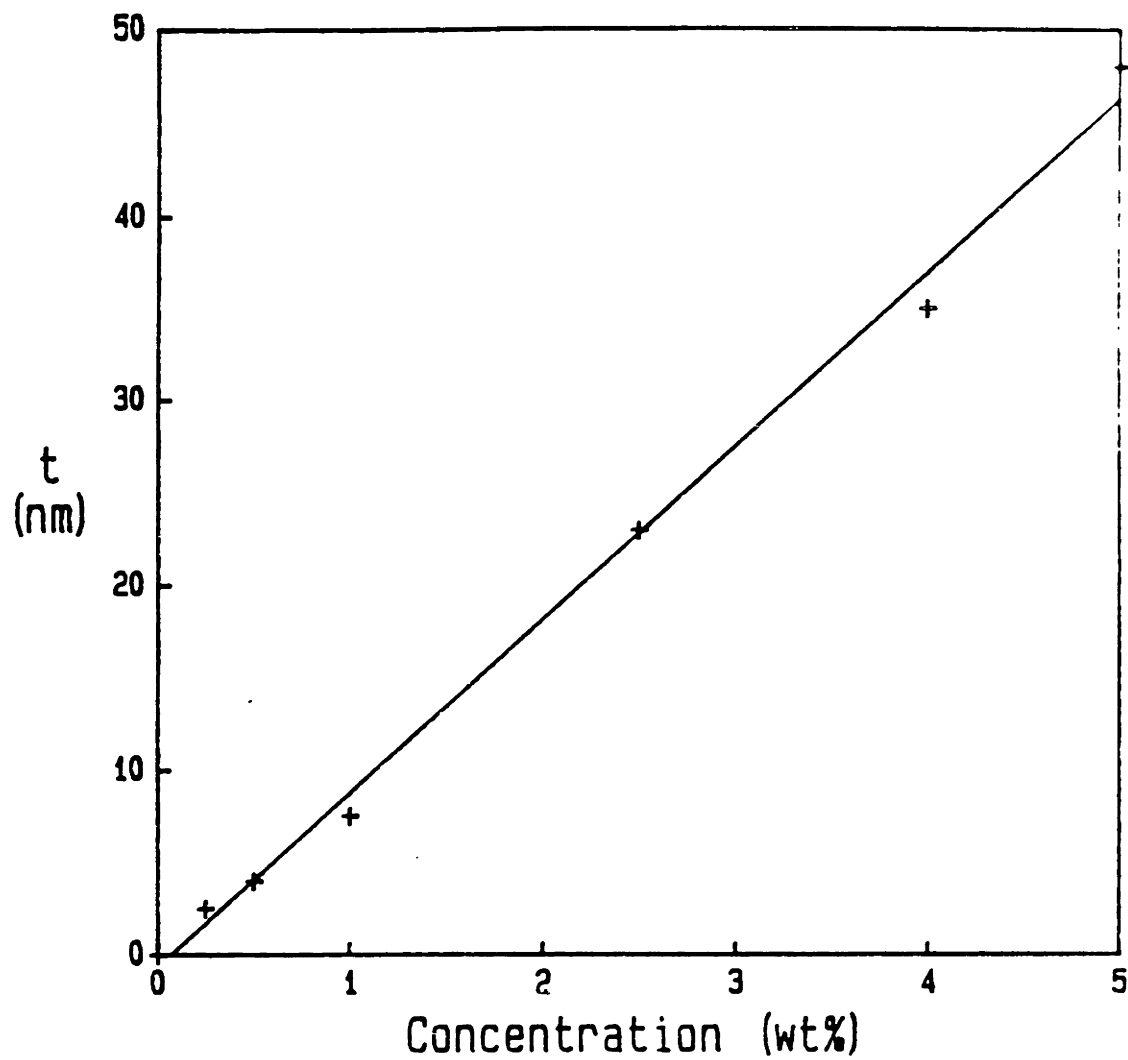


Figure 4.2.5

Thickness of undensified tantalum gels as a function of the weight percent equivalent oxide in solution. Spin speed is 5000 RPM. Line shown is least squares best fit of the data.

Table 4.2.1.

Thickness of the coating as a function of spin speed and position on the wafer using a 2.5 weight percent coating solution. The edge position was measured 0.5 cm from the edge of the 5.7 cm diameter wafer.

Speed (rpm)	Thickness (nm)	
	center	edge
3000	26.5	26.2
4000	23.9	23.4
5000	20.9	20.5
6000	19.3	19.1
7000	18.8	18.2
8000	17.1	16.8
9000	17.0	16.7

Table 4.2.2.

Concentration of the coating solution in weight percent oxide vs. thickness of the resulting coating. Spin speed was 5000 rpm.

Concentration	Thickness (nm)
.25	2.6
0.5	4.2
1.0	7.7
2.5	23.1
4.0	34.9
5.0	48.0

Initially, these single layer coatings suffered from the problem of bubbles and pinholes due to wetting problems. Wetting problems arising from poorly cleaned substrates assumed the form of bare spots on the substrate and poor adhesion to the silicon. Bubbles in the coating solution prior to spinning had a similarly deleterious effect. The pinhole problem is illustrated in a scanning transmission electron micrograph of a single stage shadowed replica (fig. 4.2.6). The flaw



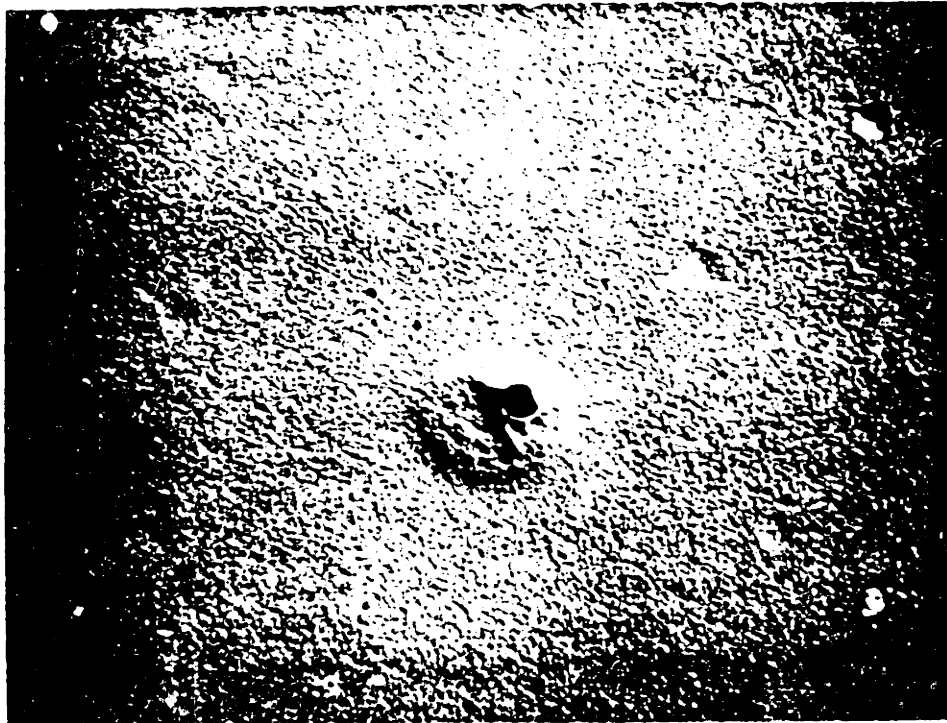
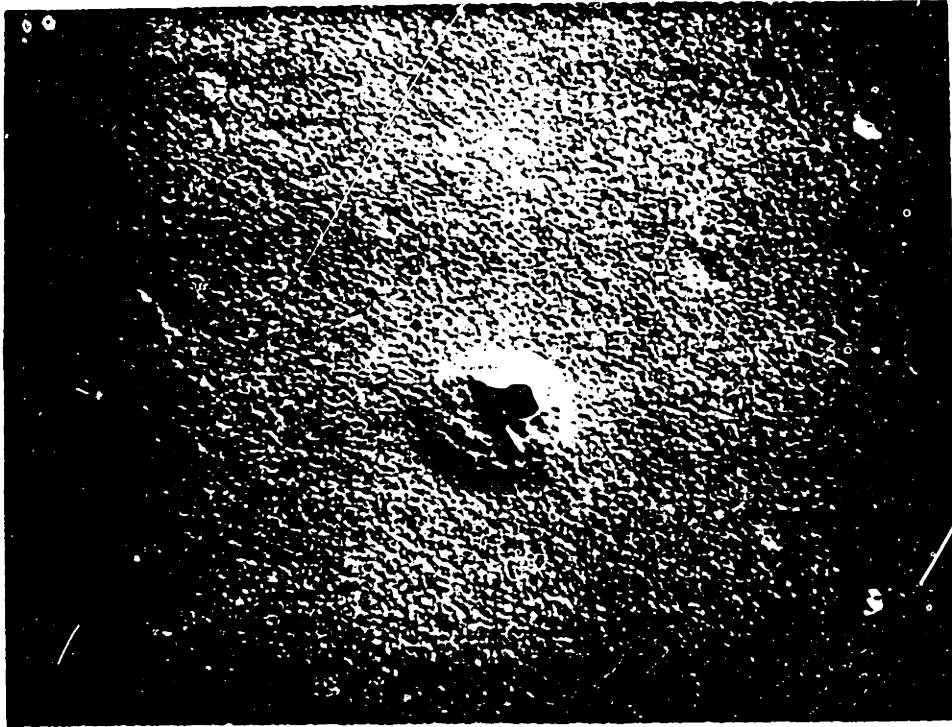


Figure 4.2.6  
Scanning transmission electron micrograph of shadowed  
one-step replica of tantalum gel surface. Major feature  
is the pinhole, although some surface texture is noted.  
Scale bar is 400 nm.



**Figure 4.2.6**  
Scanning transmission electron micrograph of shadowed one-step replica of tantalum gel surface. Major feature is the pinhole, although some surface texture is noted. Scale bar is 400 nm.

INTENTIONAL DUPLICATE EXPOSURE

was a depression with a flat bottom, i.e., a pinhole through the film to the substrate. These results were verified using Auger Electron Spectroscopy to examine the coated substrates for any substrate material that might show through. This technique showed that single layer coated samples were prone to the formation of bare spots.

If the properties of the coatings were not thickness dependent, it was decided that the thickness of the spun films should be as great as possible without running into film cracking problems so as to allow for more precise shrinkage measurements. In addition, they should be made of multiple layers so as to fill in flaws in the previous layers. To this end, multiple layers were applied to the substrates at 5000 rpm using solutions that were 2.5 weight percent oxide.

When done in the ambient laboratory atmosphere in mid-winter, the thickness of the multiple layer films built up rapidly with each additional application (fig. 4.2.7). Precipitation did not occur due to the relatively low ambient humidity. The thickness of the upper layers was quite reproducible, roughly 15.1 nm, and slightly less than the thickness of the original layer, 25.3 nm. As shall be shown later, this difference between the thickness of the first layer and that of the second is related to the amount of moisture adsorbed onto the substrate which had been stored in air, compared to that which can adsorb onto a dry film in a short time. In contrast with this, when done in the dry atmosphere of a glove bag, applying a second layer immediately after the solvent had evaporated from the first resulted in only very slight increases in the thickness of the film. Figure 4.2.8 shows that the first layer is very close to the same thickness as before, not surprising in light of the fact that they were coated on the same day after being stored under identical conditions. However, the subsequent

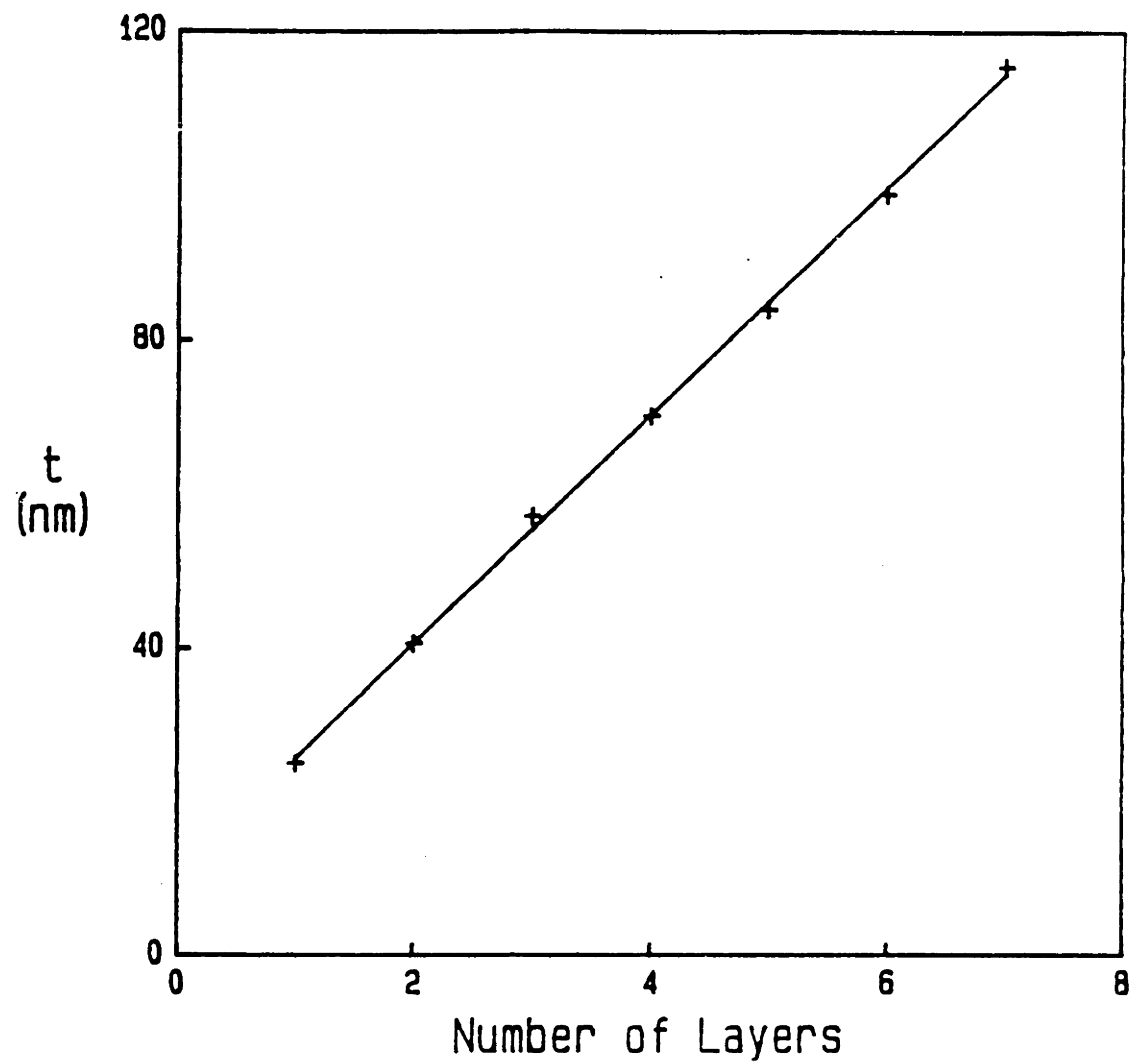


Figure 4.2.7

Thickness of undensified gels as a function of the number of layers applied. These coatings were applied in the slightly humid laboratory atmosphere of mid-winter. Coating solution contained 2.5 weight percent oxide. Substrate spin speed was 5000 RPM.

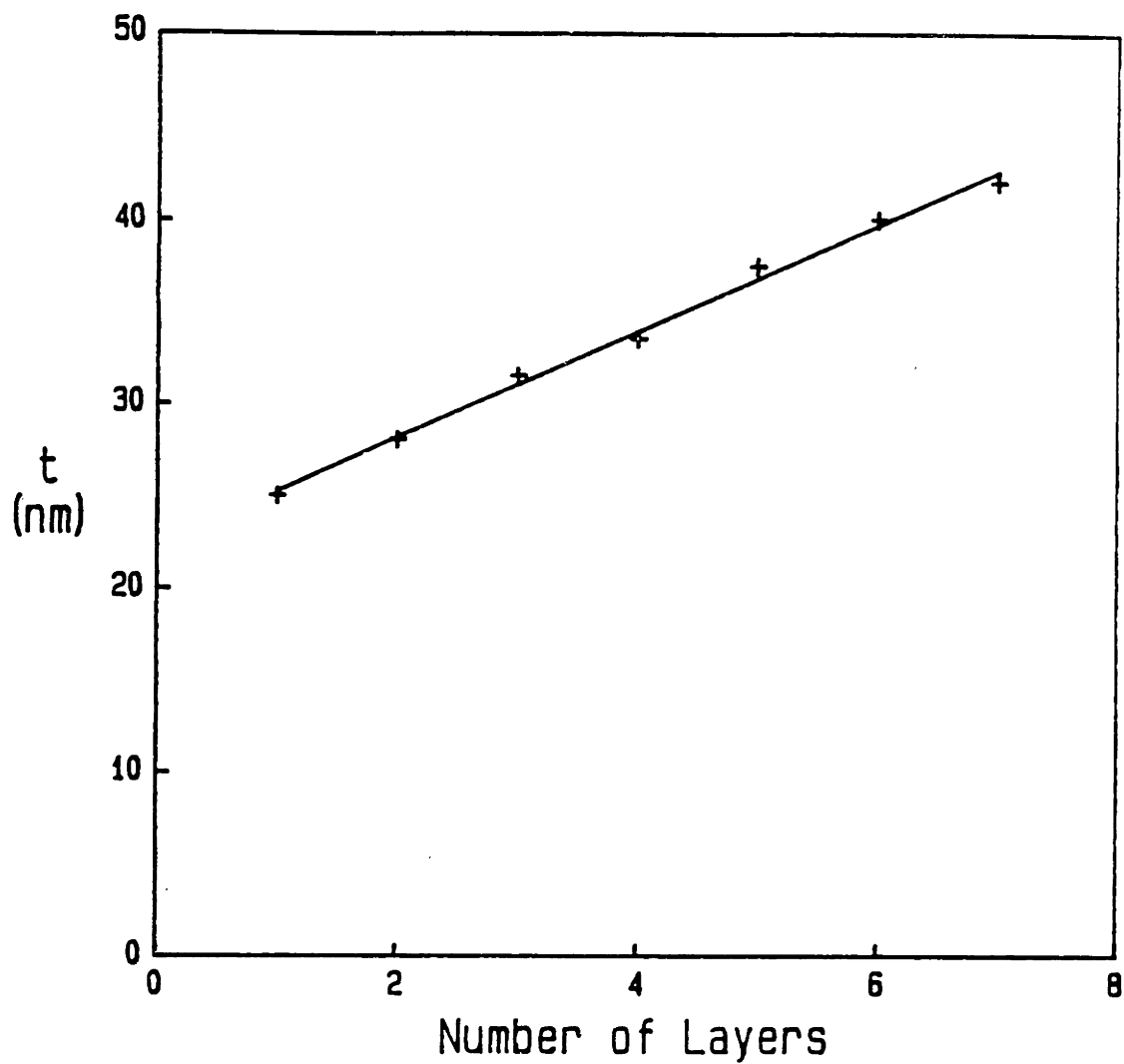


Figure 4.2.8

Thickness of undensified gels as a function of the number of layers applied. These coatings were applied in very dry atmosphere of glove bag. Coating solution contained 2.5 weight percent oxide. Substrate spin speed was 5000 RPM.

layers are quite thin, averaging 2.8 nm due to no moisture having been allowed to contact the as-spun film.

The next experiment on the effect of humidity on thickness was to remove single layer coated samples from the dry coating environment into the ambient air prior to the application of a second layer. During the exposure to the ambient air, the color of the optical interference fringe appearing on the surface changed. This change continued for up to 24 hours before stabilizing. On the contrary, samples kept in the dry environment of the spin coater did not change color. When the change occurred, it was always toward the blue end of the spectrum, indicating that the optical thickness was decreasing. This is generally due to either a decrease in refractive index or thickness, or both. Since samples not exposed to the ambient atmosphere did not undergo this change, the effect must be connected with the contact of the partially hydrolyzed and condensed film with the air. Of the components of air, water is abundant, and has been shown to cause chemical reactions in these precursors. Since water reacts with alkoxide compounds and generally results in the compaction of structures, it is likely that this is occurring here.

As mentioned before, this exposure to water causes additional hydrolysis and condensation within the film, leading to loss of ethoxy groups. The hydroxyl groups generated will be sites for possible condensations to occur. Condensation of these groups will lead to shrinkage of the film. As condensation continues, the network is getting stiffer due to the increase in crosslink density. Finally the network gets so stiff as to be unable to relax further. However, because the film is still porous, ethoxy groups will still be reacting with the ambient atmosphere to generate hydroxyls. However, because the

hydroxyls are constrained from moving, they are unable to get sufficiently close to one another for condensations to occur. Ethanol has a lower refractive index than water; however, when the density and molecular weight are taken into consideration, ethanol has a higher refractive index on a molar basis. For instance, if a given number of ethanol molecules in a given volume is replaced with the same number of water molecules, the refractive index will be lower. Therefore replacement of a given number of ethoxy groups with hydroxyls on a given number of sites in the network might lower the index of refraction of that network. Therefore, the change in optical thickness might be due to both decreases in thickness and refractive index of the films.

Coating in a dry atmosphere and hydrolysing the coating by exposing it to the ambient atmosphere worked as well as coating in the ambient air as far as how the thickness built up, and did not result in the precipitation of particles mentioned earlier. However, it was cumbersome, and allowed the dry coating environment to be contaminated with water every time the glove bag was opened. The next experiment was to blow humidified nitrogen onto a previously coated spinning sample for 30 seconds while still in the dry environment. This method also resulted in good layer addition. In this way we also limited the exposure of the sample to dust and dirt in the laboratory environment. However, when humidity was injected into the chamber, precipitation occurred in the subsequent layer as the coating solution sat on the substrate prior to spinning. This was overcome by allowing an additional 30 second spin under the flow of dry nitrogen for excess moisture to evaporate from the wafer as well as for the Drierite in the spin bowl to absorb most of the moisture introduced.

Hydrolysis of previous layers in order to apply additional ones is

necessary because as the films are applied they are very dry. The oligomers closest to the substrate attach themselves to the substrate by condensing directly onto the surface silanol groups of the wafer. In the extreme case of coating in an atmosphere containing absolutely no water, they do not crosslink at all because there are no hydroxyl sites on the oligomers as they are deposited from solution. The solvent evaporates, leaving a layer of oligomers covering the silica surface. As subsequent layers are applied, the solutions dissolve the layer previously applied, except for the first layer that is bonded directly to the substrate. If this model were applied to a system in a totally dry environment, one would see the thickness vs. number of layers graph level off after two layers had been applied. As the coating chamber was probably not entirely dry, one might expect the slight increase in thickness with the application of each additional layer that is observed.

As determined using Auger Spectroscopy, building layers on top of one another eliminates the signal from the substrate. This indicates that multiple coatings solve the pinhole problems. This result is not due to the increase in thickness of the film, but must result from increased surface coverage because the Auger electrons only come from a very thin layer at the surface of the sample. However, just as in other sol-gel derived materials, if the thickness of the multiple layer structure is too great before complete drying occurs, the film will crack. This can be understood best when taken in the context of the drying process occurring in the films for up to 24 hours as indicated by the gradual change in color. Exposing the film to moisture for a short time does not allow the film to attain the structure that it would reach after sitting for one day in the laboratory atmosphere. Therefore, if the



film is built up to a large thickness but none of the individual layers have dried completely, one runs the risk of developing cracks as the individual layers age and shrink.

The above discussion brings to mind the possibility of fabricating films thicker than 130 nm by allowing a sufficient period of time after the deposition of each single layer for the oligomers to become completely hydrolysed and condensed. If this were done there would be no dimensional change subsequent to the drying of additional layers. However, we must then examine the result of putting solvent back into the pores of a dried gel that was the product of previous processing steps. Will it swell as happens in many organic and siloxane polymeric systems? The answer is most likely not. The fully hydrolysed lower layers are probably sufficiently crosslinked to prevent swelling. If this is the case, it may be possible to build thick multilayer structures with this method.

For multilayer films deposited as described here, the maximum thickness before aging is roughly 130 nm if the film is to remain intact upon drying completely. This value is close to that reported for films derived from titanium ethoxide [65], but far less than that reported for gel-derived silica films. The explanation for this may be tied into the observation that in both the titania and tantala systems condensation is not reversible as it is in silicates, and is much faster than corresponding alkoxy silane systems. This could lead to a film with a higher crosslink density than is the case for silica, possibly resulting in a stiffer, higher modulus film. During drying, the film will try to relax in order to eliminate the stresses that arise. If the same amount of strain were imposed on the material, a more brittle film will have a higher stress level, and may therefore be unable to accommodate these

stresses without failing. The addition of a bidentate complexing agent such as 2,4-pentanedione should reduce the crosslink density, and hence make it easier for the film to relax during drying. It should, therefore, be possible to make films that are thicker than the previously stated upper limits using this scheme, and some success has been reported [64]. It should be made clear, however, that the comparison between tantalum and silica films is not nearly this straightforward. Other issues such as film nanostructure and the volume fraction solids are different in the two materials, and may play a key role in the maximum attainable thickness before fracture.

However, in order to make films that are appreciably thicker than this, the coating procedure will have to be changed. If it is allowed for the first multiple layer coating to be fired before the application of a second coating, it is likely that very thick coatings may be produced by a process that alternates several coating and firing steps. Even if multiple firing steps are not permitted, it might be possible to generate thick films by allowing the previous layer to dry completely before the application of a subsequent one. This scheme would be hard to justify for silica film because the drying (hydrolysis/condensation) rate is so slow. In the case of a fast reacting precursor, on the other hand, if there is minimal disturbance of the previous layer by the application of another this scheme may work.

It should be stressed that using the procedure outlined here, it is possible to produce smooth, precipitate free, pinhole free coatings. In addition, rules for thickness versus spin speed and solids content of the coating solutions for more well known systems apply here as well. The coatings must be applied to very clean substrates in a dry, dustfree environment, with each layer having been hydrolysed preceding the

application of a subsequent one. It was these coatings which were analysed as presented in the following sections.

#### 4.3. Densification of films

After the films had dried and fully reacted with moisture subsequent to coating, they were fired at various temperatures to characterize the densification process. Initial runs were made by loading the samples directly into furnaces already at their desired temperature. To decrease the amount of time for the furnace to equilibrate after loading, the sample carriers were preheated. The carriers were removed from the furnace, loaded with samples, and reinserted into the furnaces. While still outside the furnace, the optical interference colors on the films changed immediately upon exposure to the hot sample carriers. After being held at temperature for up to 24 hours, the color had not changed appreciably from the initially loaded color, indicating that a majority of the densification had occurred in the first few seconds at the elevated temperature.

Profilometry of the steps that had been etched into fired films indicated that densification occurs to its full extent within the first hour of heating, with no additional shrinkage occurring in the next 23 hours (fig. 4.3.1), for temperatures greater than 300 C. At 150 C, the film continued to shrink for longer than 5 hours. As a function of the firing temperature, the thickness of the film decreases continuously from its room temperature thickness until roughly 700 C (fig. 4.3.2). Between 700 and 750 C, the slope of the densification curve levels off with no additional densification occurring up to 1000 C. The films lose a total of about 55% of their original volume during densification when

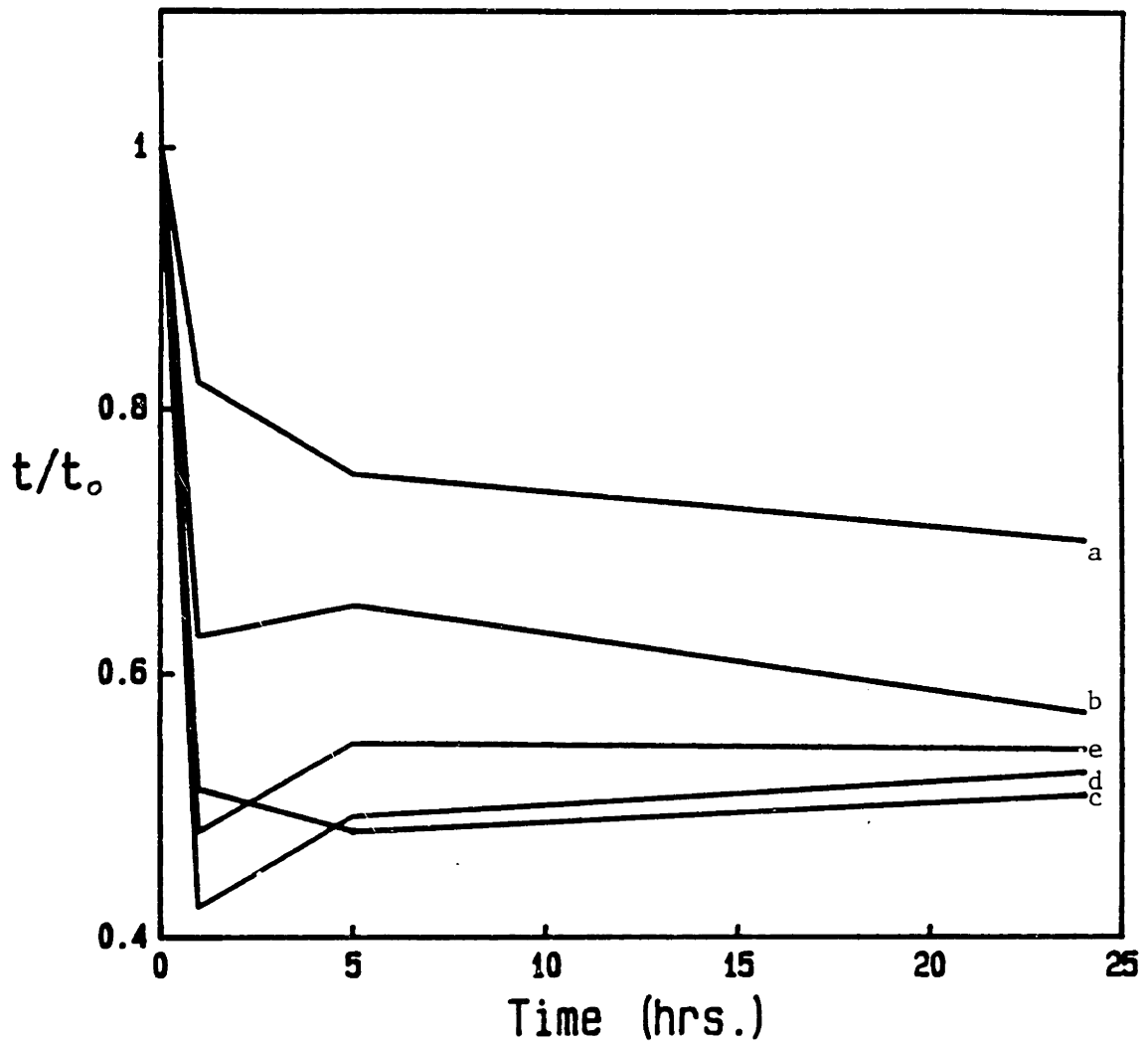


Figure 4.3.1

Thickness of fired gels as a function of the firing time at various temperatures. Thickness has been normalized to the thickness before firing.

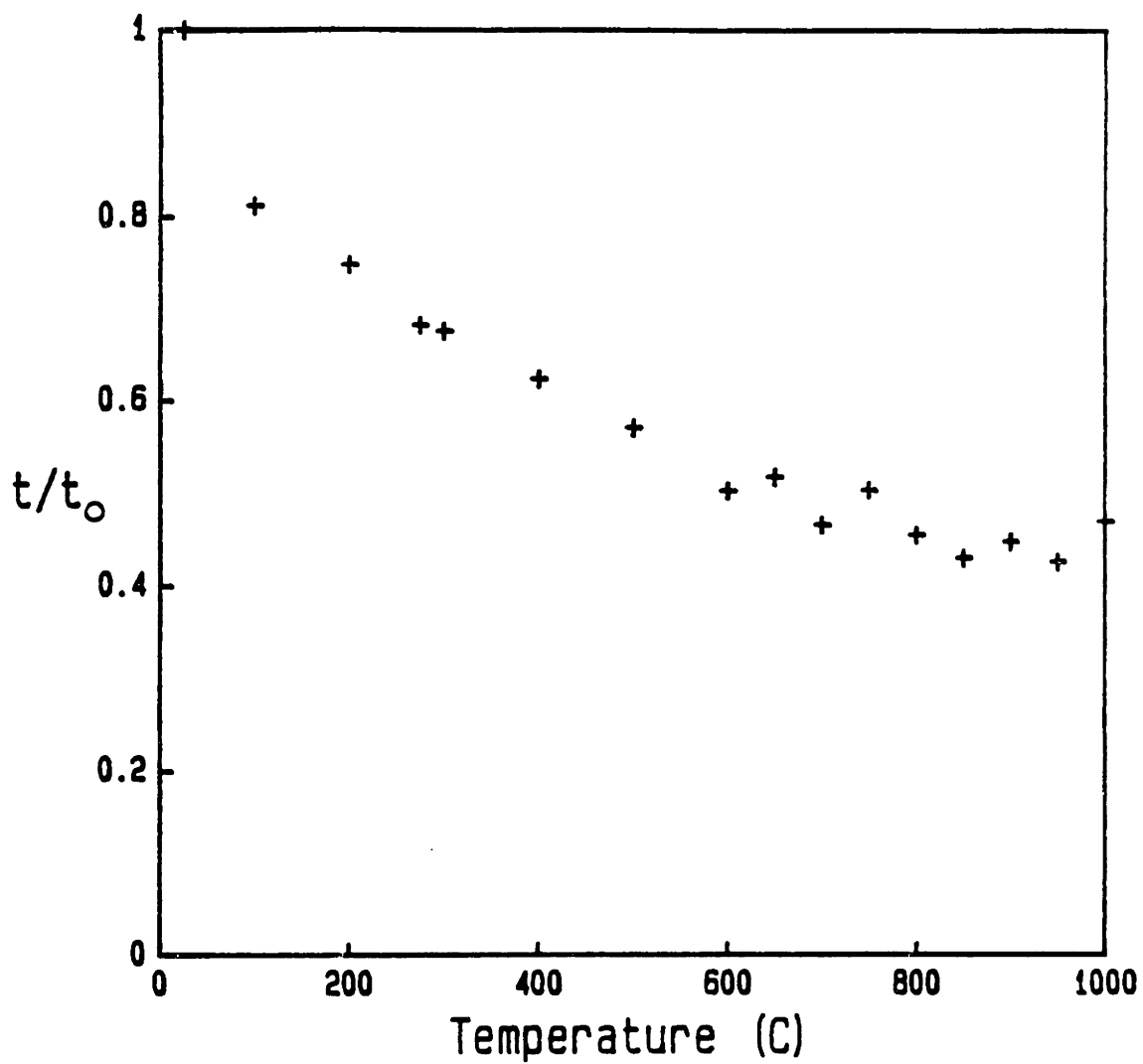


Figure 4.3.2  
Thickness of fired gels as a function of the firing temperature. Thickness has been normalized to the thickness before firing. All films were fired for one hour.

fired to 1000 C.

If the densification observed in these films were due entirely to structural relaxation, one would expect the films to continue to decrease in thickness as long as the elevated temperature were maintained. This is clearly seen at 150 C, but not at the higher temperatures. There are two possibilities. The first is that the measurement is not sensitive enough to detect the changes between 1 and 24 hours at an elevated temperature. This could be true. However, the data indicates that upon heating for extended times, the film actually expands. This is also indicated during the densification of pressed powder pellets, and will be discussed there.

The refractive index, measured ellipsometrically, of the films described above shows complementary behavior. The index is seen to rise from its unfired value of 1.73 to level off at just below 2.1 between 750 and 800 C (fig. 4.3.3). It should be noted that these values are independent of film thickness and are identical to those reported for the refractive index of tantala films formed from sols [15]. The refractive index of the most dense films is not as high as has been most often reported for crystalline or amorphous tantala (2.2). If one assumes that the refractive index is due to randomly located spherical pores in a matrix that does not change in refractive index, using the relationships mentioned earlier the amount of porosity is calculated as decreasing from 51 to roughly 8 percent. As adsorbed water and alcohol, as well as residual hydroxyl and ethoxy groups, will contribute to the refractive index for unfired films, the former number is an underestimate of the amount of porosity initially present.

STEM on shadowed single stage replicas of unfired films indicated that the film surfaces are reasonably smooth when compared with the

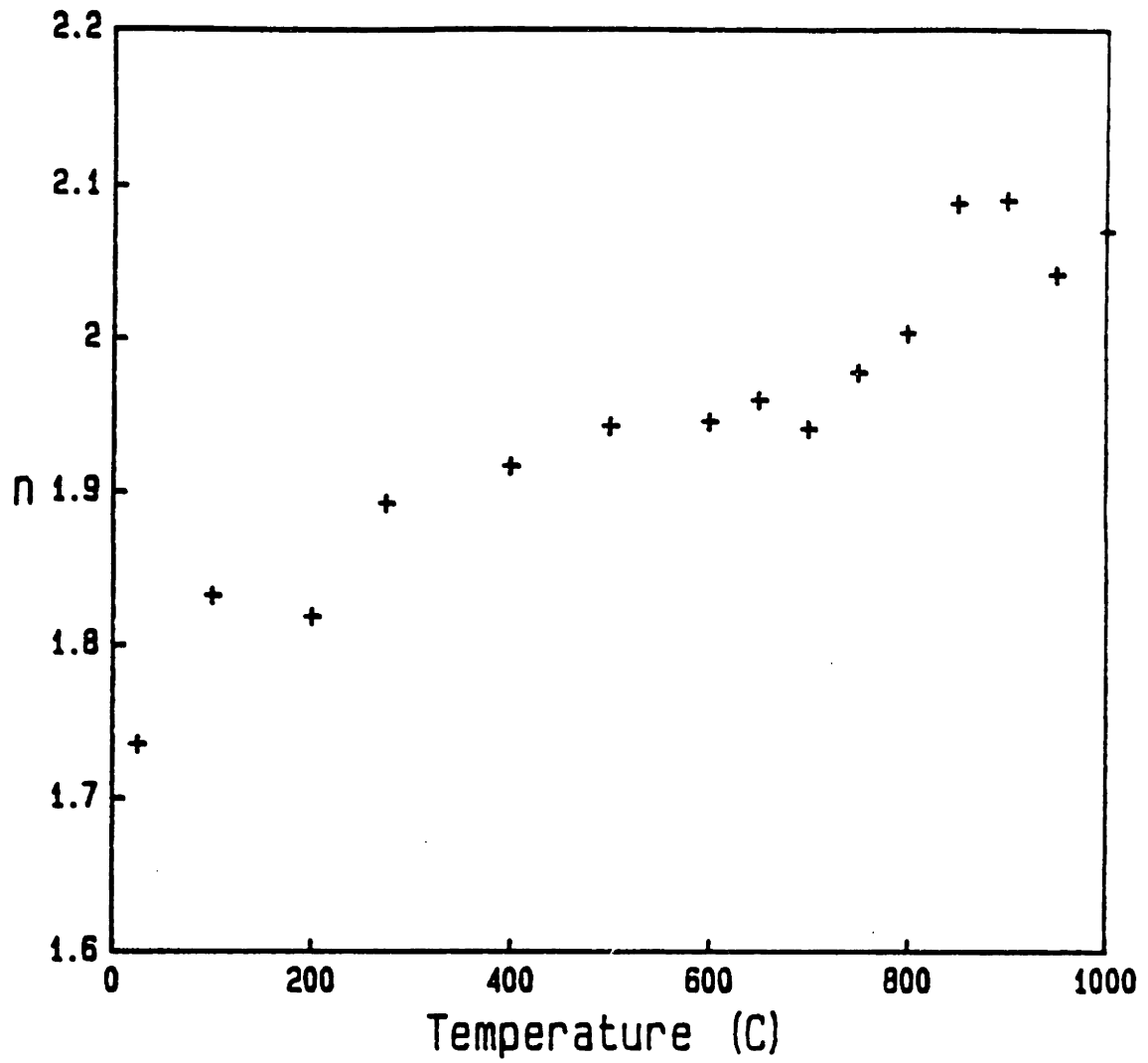
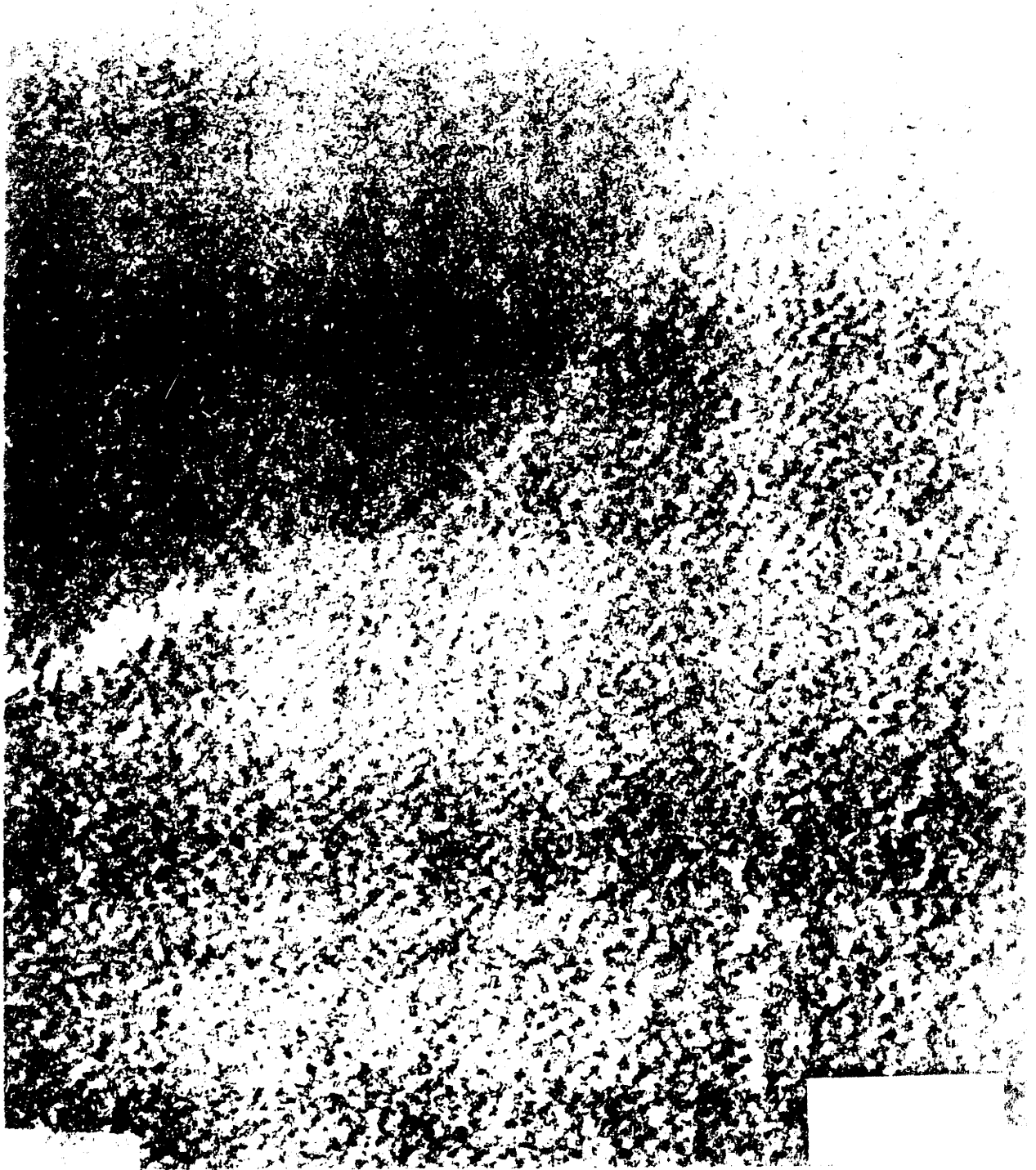


Figure 4.3.3  
Refractive index of fired gels as a function of the firing temperature. All films were fired for one hour.

thickness of the film, the exception being macroscopic defects such as pinholes, which presumably account for only an exceedingly small volume fraction. TEM was used to inspect the films for porosity. Films with heat treatments ranging from unfired to fired for 1 hour at 1000 C showed no porosity greater than 2 nm in diameter (fig. 4.3.4). The crystal grains are large fractions of a micron in diameter, and extend from the substrate all the way to the upper surface. Noncrystalline films examined at high magnification resulted in a salt-and-pepper pattern roughly 4 to 5 nm in size (fig. 4.3.5). However, upon examination of these micrographs, one first notices that there are large grooves and pits clearly visible. This topographical effect is greatest closest to the edge of the perforation. Micrographs of replicas of films that were not ion milled (fig. 4.2.6) do not exhibit these features. This indicates that ion milling produces the holes and grooves in the sample. The large amount of milling damage may result in the 4 nm features mentioned above. Crystalline films, on the other hand, ion mill more evenly; and the large features seen in the unfired milled films are not evident. The crystalline films do show 2 nm diameter features (fig. 4.3.4) due either to fine porosity or surface roughness which may reflect artifacts of the milling step.

Electron diffraction from these films was used to determine the crystallinity. Transmission diffraction patterns taken on unfired samples as well as those heated as high as 600 C for one hour showed no hint of crystallinity (fig. 4.3.6), only the broad halo characteristic of amorphous materials. Films fired at or above 700 C for one hour resulted in patterns which were clearly crystalline, with diffraction rings corresponding to the interplanar spacings of beta tantalum. Identical films were examined using reflection high energy electron





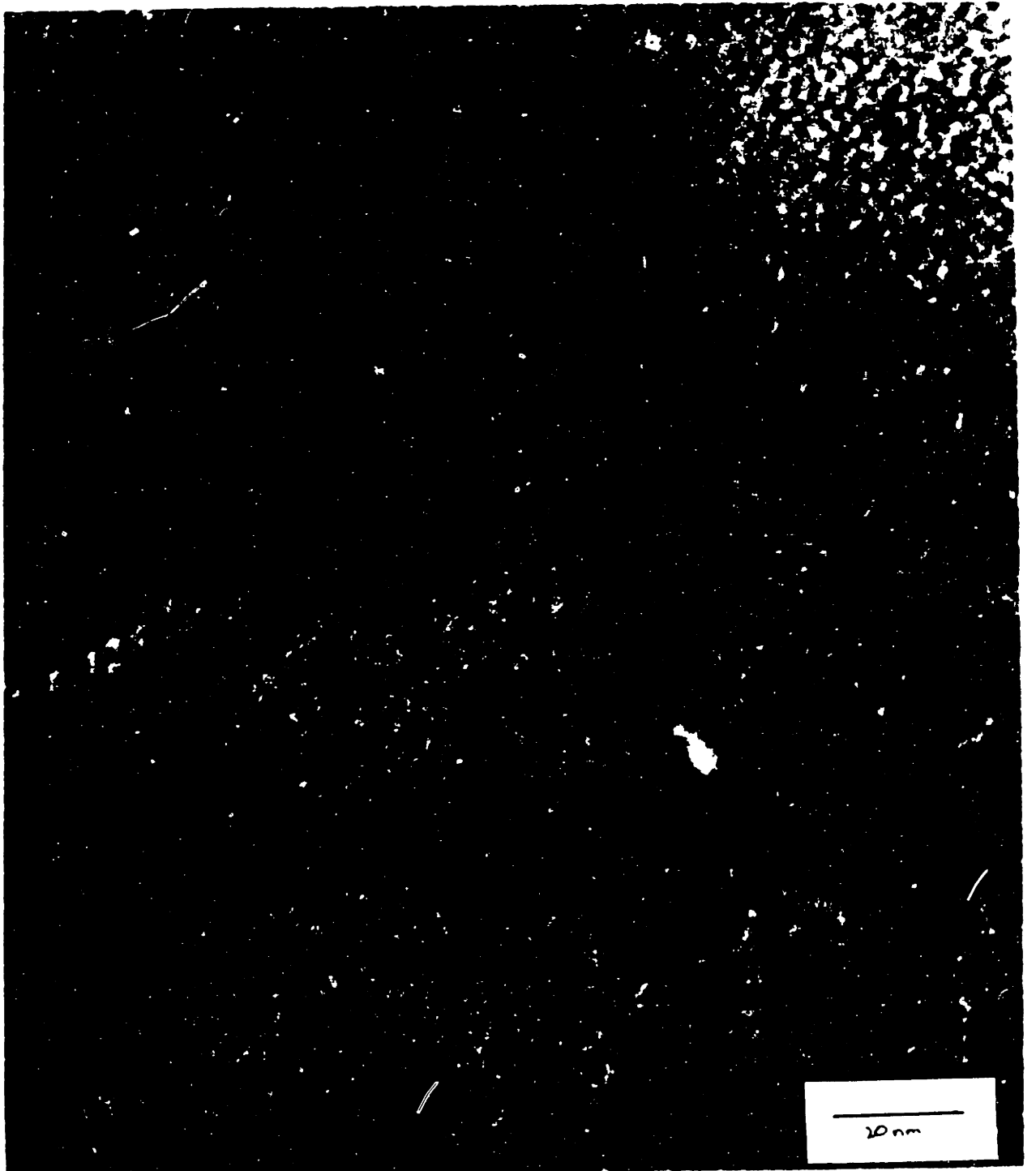
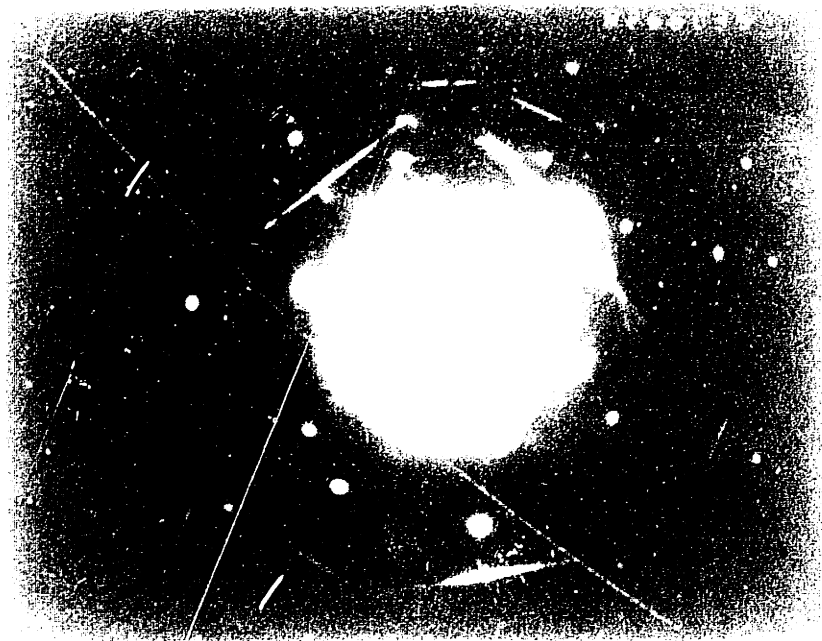
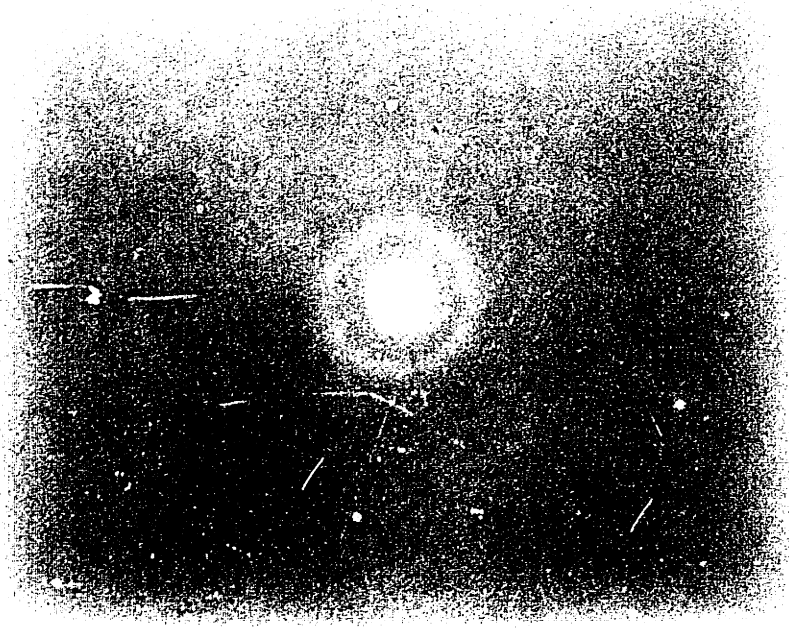


Figure 4.3.4  
Transmission electron micrograph of tantalum gel on silicon  
substrate. Gel has been fired at 1000 C for 1 hour. Scale  
bar is 20 nm.

INTENTIONAL DUPLICATE EXPOSURE



**Figure 4.3.5**  
Transmission electron micrograph of tantalum gel on silicon  
substrate. Gel is unfired. Scale bar is 100 nm.



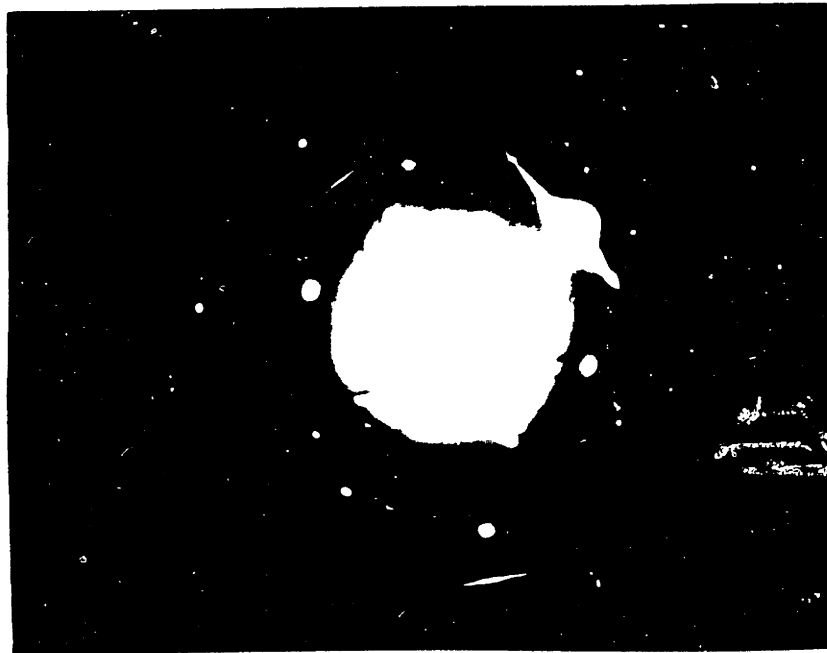
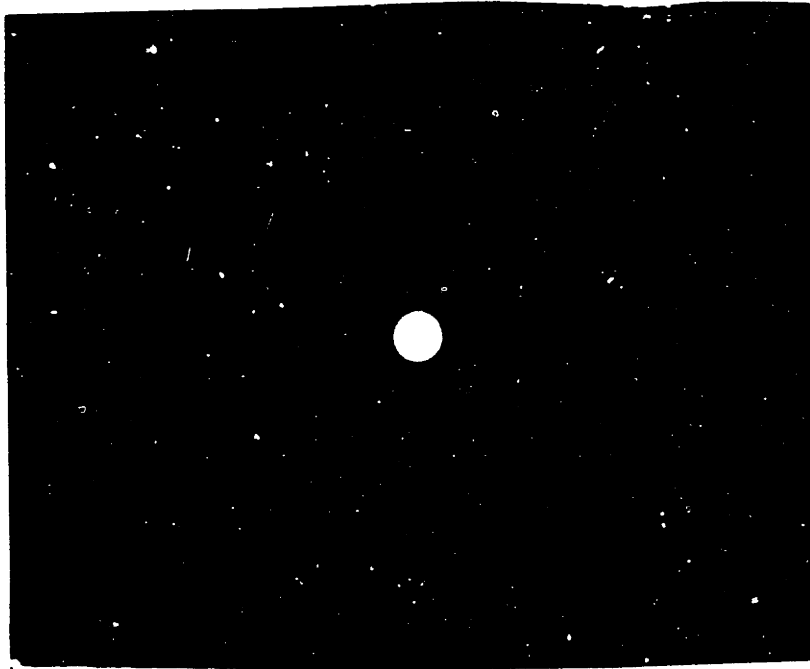


Figure 4.3.6  
Electron diffraction pattern of tantalum gels fired at  
(a) 600 and (b) 700 C. Diffraction was taken in transmitted  
electrons.

INTENTIONAL DUPLICATE EXPOSURE

diffraction. Here, films fired at 600 C for one hour showed a slight amount of crystallinity superimposed on a mostly amorphous pattern, indicating that these films were just starting to crystallize. Films fired to 700 C for one hour gave rise to a well developed crystalline pattern (fig. 4.3.7).

TEM was also performed on films applied to carbon covered grids. Films that were unfired showed salt-and-pepper patterns as described above. However, when the films were fired in nitrogen at 800 C for one hour the microstructure changed dramatically. These micrographs show large three-dimensional grains of crystalline tantalum oxide with crystallographically oriented pores (fig. 4.3.8). This is in stark contrast to the films fired on silicon which were flat and quite uniform. Each grain of the fired carbon-supported film is a single crystal, as evidenced by microdiffraction patterns obtained in the STEM. The crystallographic orientation of the pores is also evidence that each grain is a single crystal. The average grain size in this sample was 120 nm, while the average pore is a rectangular hole, roughly 4 by 15 nm. In this case, the film has broken in many places, then densified and sintered, resulting in the grains having moved in all three dimensions, forming a tangled network of necked particles.

This is evidence of what may occur during the densification of supported films which are bonded to the substrate and those which are not. The former, being constrained by the substrate, are allowed to move in only one direction - perpendicular to and towards the substrate as discussed earlier. Films densified in this manner are comprised of large planar grains. In contrast, when the film is not bonded to, and does not wet the substrate, it can move in all directions, breaking at weak points and forming oddly shaped grains with a considerable

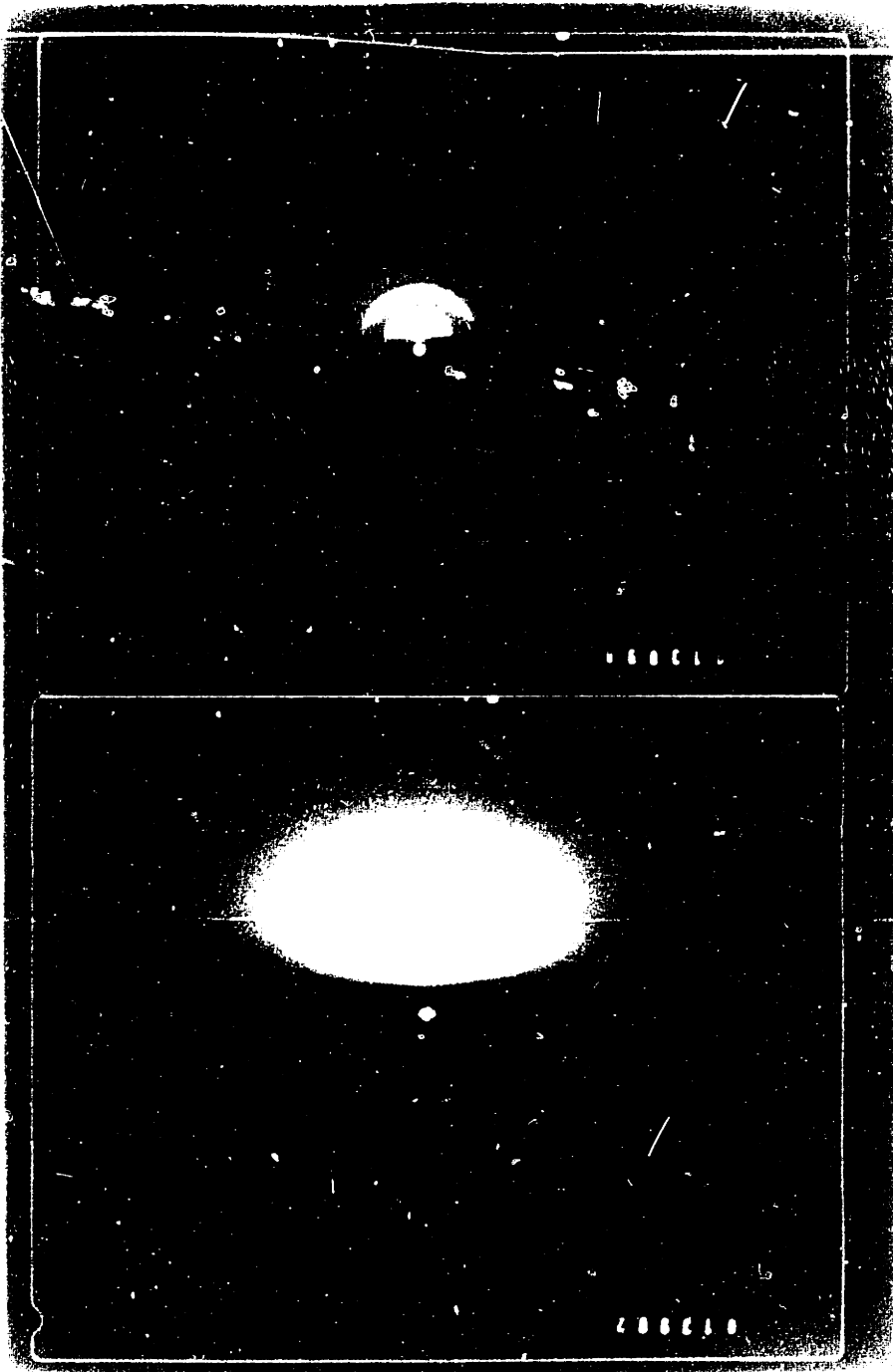




Figure 4.3.7  
Reflection high energy electron diffraction patterns of  
gels on silicon substrates. Gels were fired at (a) 500 °C  
and (b) 700 °C.

INTENTIONAL DUPLICATE EXPOSURE





Figure 4.3.3

Transmission electron micrograph of gel on carbon substrate, been fired for 1 hour at 800 C. Scale bar is 20  $\mu$ m.



Figure 4.3.8

Transmission electron micrograph of gel on carbon substrate.  
Gel has been fired for 1 hour at 800 C. Scale bar is 20 nm.

INTENTIONAL DUPLICATE EXPOSURE

thickness to reduce the surface to volume ratio. This is shown schematically in figure 4.3.9.

Summarizing this section, tantala gels densify rapidly at fairly low temperatures, with 92% of theoretical density, as determined using the refractive index of the film, being reached at 700 C. The microstructure of the densified film is quite dependent on the extent to which the film is bonded to the substrate. The films were shown to start crystallizing after 1 hour at 600 C, and were fully crystalline after 1 hour at 700 C.

#### 4.4. Electronic Characterization

Metal-insulator-semiconductor (MIS) capacitors, prepared as described earlier, were characterized with high frequency capacitance-voltage measurements. As stated earlier, the capacitance in the accumulation regime is a function of only the dielectric constant of the dielectric layer and the geometry of the system. Therefore, the maximum capacitance in this region was used to calculate the dielectric constant of the composite silica-tantala layer. Then, using the series model for the composite, the dielectric constant of the tantala portion of the dielectric was calculated. As photolithography uses a 10 minute-200 C dehydration step, data on films fired to temperatures below 300 C were not reliable because we were unable to use photolithography to define the gate electrodes. The gate electrodes formed by masking with wax were poorly defined in shape and size, causing much variability in the calculated dielectric constant. The dielectric constant of samples fired at 300 C was 46, declining to 30 as the firing temperature was

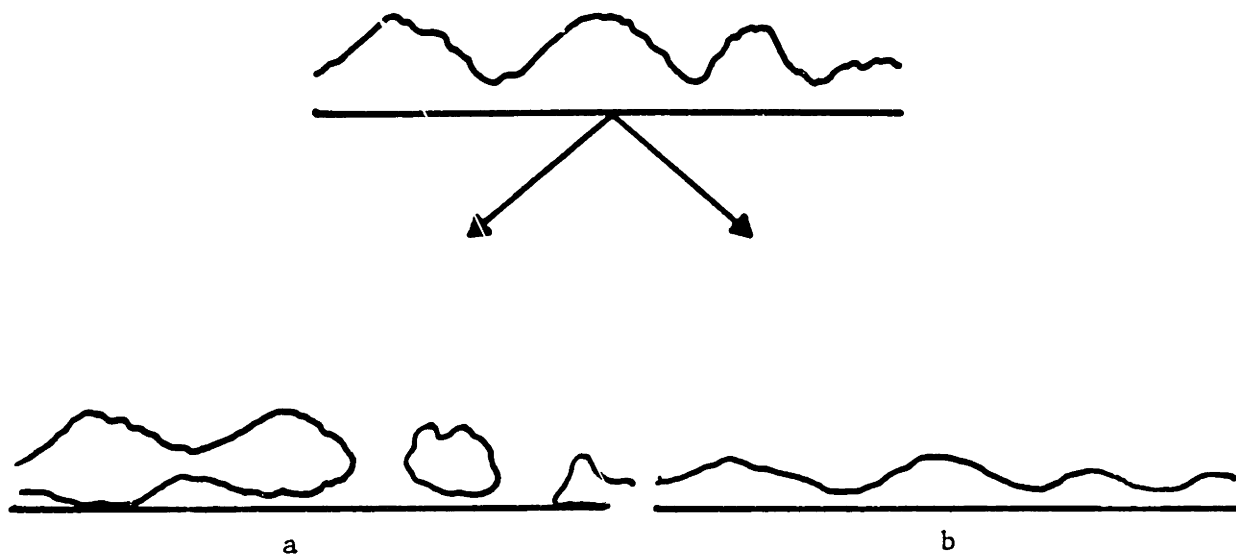


Figure 4.3.9  
Schematic of how adhesion to substrate effects the densification behavior of gels. Example (a) represents no bonding to the substrate, where the film can move in all directions and holes may develop. For tight bonding to the substrate (b), gel may only densify perpendicular to substrate.

increased up to 600 C (fig. 4.4.1). At that point the dielectric constant leveled off. This result is independent of film thickness from 200 to 600 nm.

For samples fired at 800 C for one hour, the loss factor is 0.032. When the loss factor is plotted against the log of the frequency, figure 4.4.2 is obtained. The sharp increase at high frequencies is probably due to the limit of the machine's reliability having been surpassed. The value obtained here is in the same range as that obtained for a similar thickness of anodic tantalum (0.007) [14], but slightly higher. Because the film is crystalline, the actual structure of the skeletal material can not account for this. It must be due to impurities either remaining in the material, or those that segregated to pores, grain boundaries, or the surfaces of the films.

The trend in the dielectric data is similar to that reported for gel derived silica films [77]. The initial trend in these data might be explained by noting that the dielectric constants of water and ethanol are close to 80 at a frequency of one megahertz. The unfired films contain high concentrations of these species. When they are removed from the film by evaporation, condensation and decomposition upon heating, the dielectric constant decreases. One must note, however, that there is little water or volatile carbonaceous content remaining in the sample after firing to 400 C (see next section). Therefore, the decrease in dielectric constant must have an additional explanation.

If one plots the measured capacitance of samples that all had the same thickness before firing as a function of firing temperature (fig. 4.4.3), one observes that the capacitance decreases slightly from 300 to 500 C, drops sharply around 700 C, then rebounds to very close to its original value at 800 C. As each datum presented in figure 4.4.3 is the

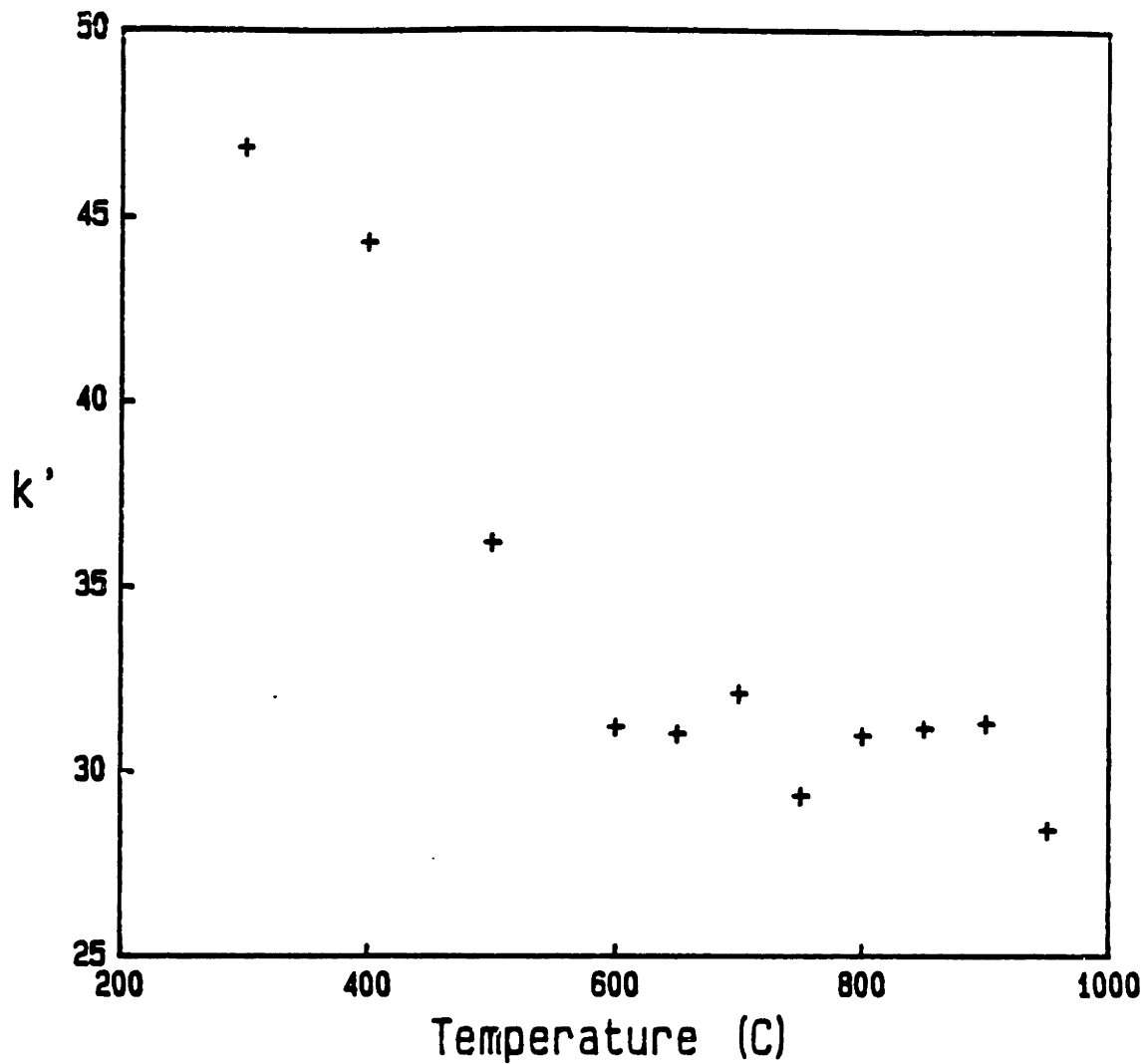


Figure 4.4.1  
Dielectric constant of tantalum gel films as a function of the firing temperature. All films were fired for 1 hour.

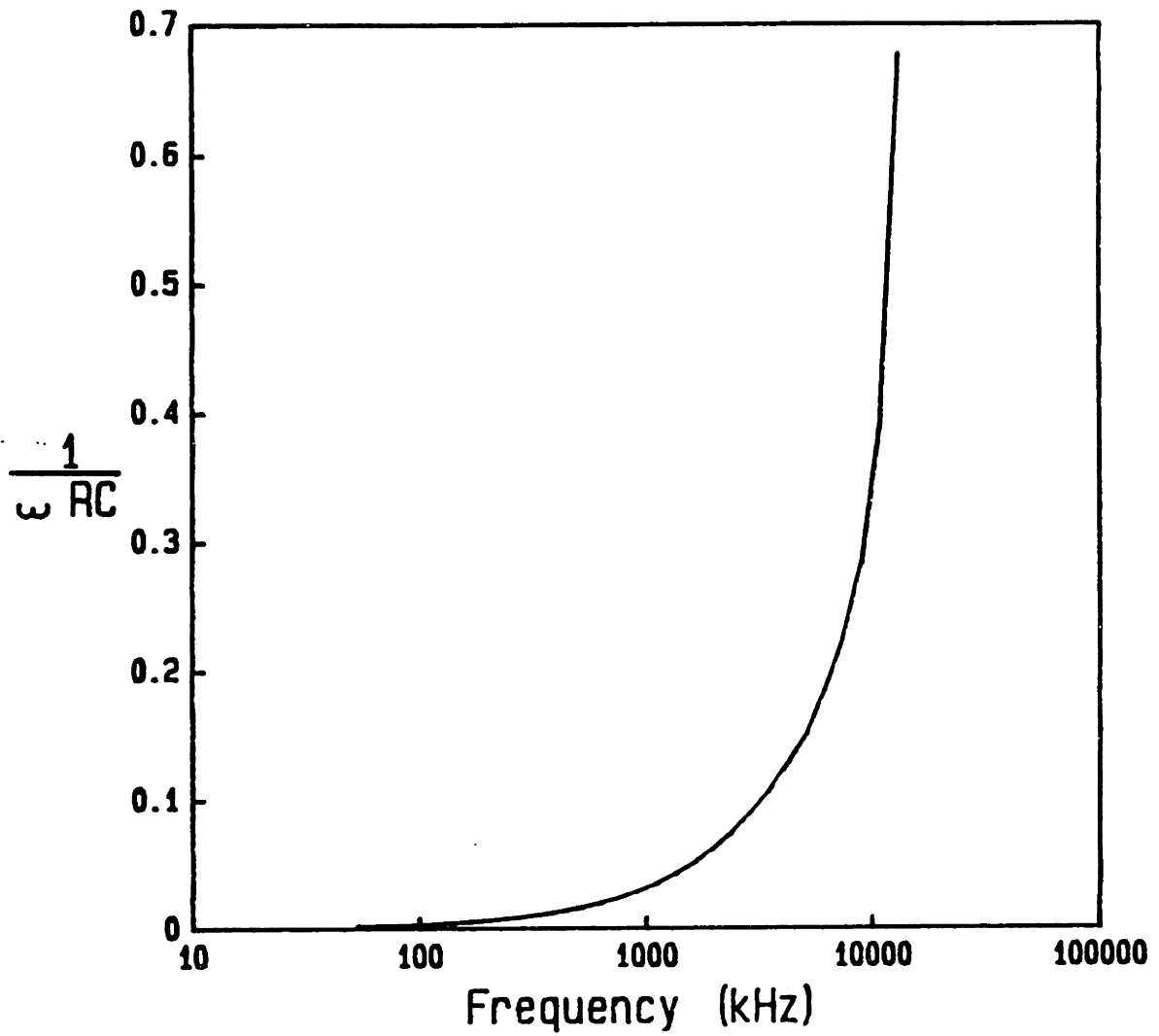


Figure 4.4.2  
Frequency dependence of loss factor for nominally pure tantalum  
fired for 1 hour at 300 C.

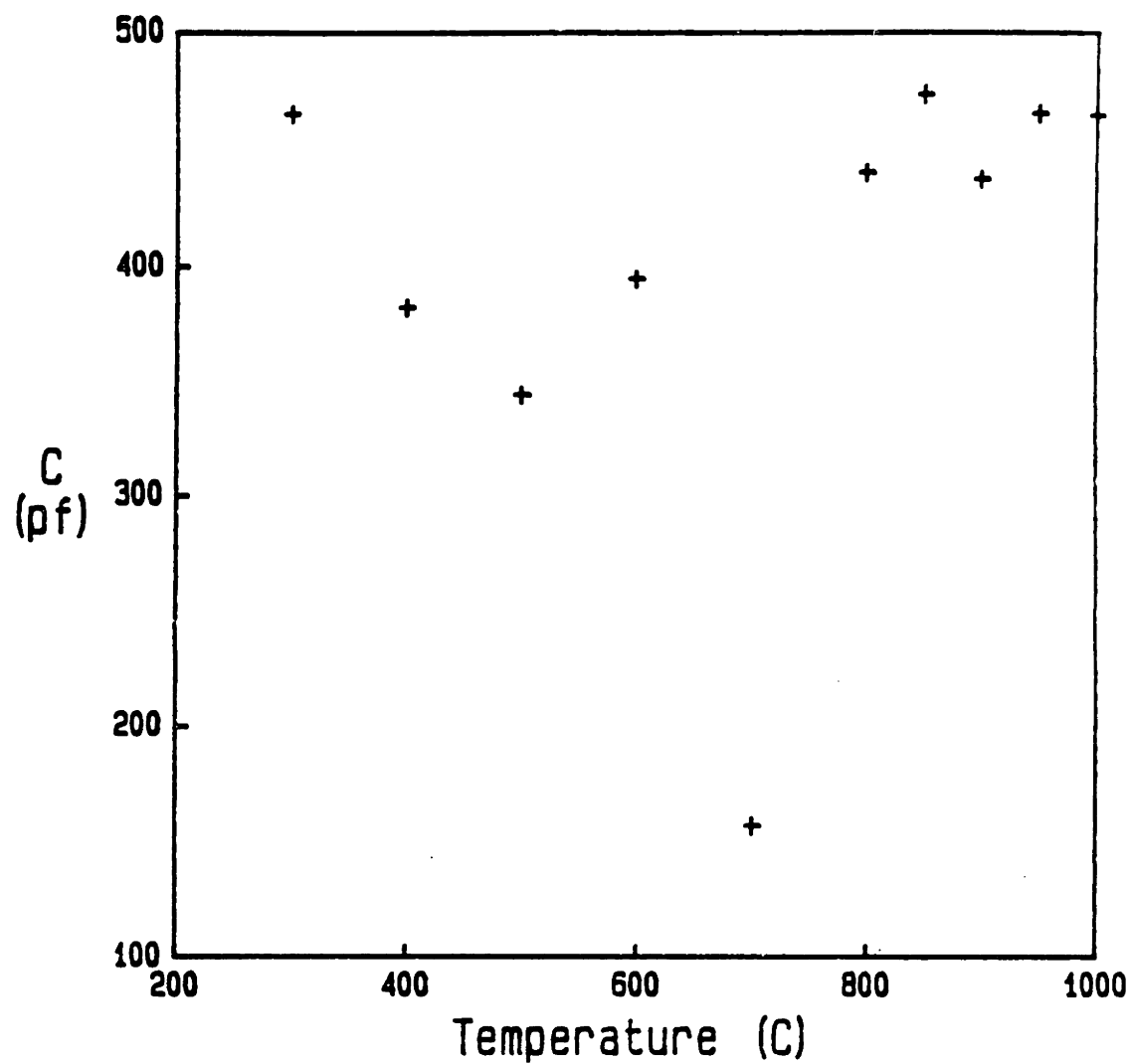


Figure 4.4.3  
Measured capacitance of tantalum gel films as a function of  
the firing temperature. All films were fired for 1 hour.



average of measurements of eight devices, this deviation can not be ascribed to a measurement error. The first step is to calculate the effect of the change in thickness of the film during densification. Combining the equation for capacitance (eq. 2.5.1) with the relationship between dielectric constant and volume of a second phase (eq. 2.6.2),

one obtains

$$C = \frac{E_0 A}{l} \frac{V_m k'_m \left( \frac{2}{3} + \frac{k'_d}{3k'_m} \right) + V_d k'_d}{V_m \left( \frac{2}{3} + \frac{k'_d}{3k'_m} \right) + V_d} \quad (4.4.1)$$

The structure after complete densification is, for our purpose, a single phase of thickness  $l_0$ . The volume of the this phase ( $V_m$ ), considered the matrix phase in this discussion, is the product of the thickness and the area of the capacitor

$$V_m = A l_0 \quad (4.4.2)$$

If one were to inject pores, the dispersed phase, into the matrix without removing any of the matrix volume, the volume of the composite would increase by the volume of the dispersed phase ( $V_d$ ). The volume of the dispersed phase could be calculated by subtracting the volume containing the pores to the volume of the non-porous structure, i.e.,

$$V_d = V - V_m \quad (4.4.3)$$

This volume is equivalent to the area of the capacitor multiplied by the change in thickness ( $\Delta l$ ), i.e.,

$$V_d = A \Delta l \quad (4.4.4)$$

For simlicity,  $x$  is defined as

$$x = \frac{3}{2} + \frac{k'_d}{3k'_m} \quad (4.4.5)$$

Substituting eqs. 4.4.2, 4.4.4 and 4.4.5 into equation 4.4.1, and if  $\Delta l$  is considered a fraction of  $l_0$ , ( $y l_0$ ), we find

$$C = \left( \frac{E_0 A}{l_0 (1 + y)} \right) \left( \frac{k'_m x + k'_d y}{x + y} \right) \quad (4.4.6)$$

If we now normalize this value by the capacitance of the non-porous

structure,  $C_o$ , we obtain

$$\frac{C}{C_o} = \left( \frac{1}{k'_m(1+y)} \right) \left( \frac{k'_m x + k'_d y}{x+y} \right) \quad (4.4.7)$$

We can use this equation to model the effect of included porosity on the measured capacitance as the system densifies, assuming that the dielectric constant of the matrix and dispersed materials do not change. Figure 4.4.4 shows that the measured capacitance should increase by a factor of two upon densification from a 45% porous state to a 9% porous state, as has been shown upon heating these films from 400 to 750 C.

As this phenomenon is not observed, the dielectric constant of the skeletal material must decrease appreciably between 300 and 700 C, as the measured capacitance is seen to decrease by a factor of 3, instead of increasing as predicted. Calculating the change in dielectric constant, based on the shrinkage model, one discovers that the dielectric constant of the skeletal material actually decreases by roughly a factor of 6 between 400 and 700 C. The factor of three increase in capacitance seen between 700 and 800 C cannot be entirely due to shrinkage effects, and may be related to the crystallization of the amorphous matrix.

One possible explanation for the decrease in the skeletal dielectric constant is intimately connected with the change in the fictive temperature of the amorphous phase as the "annealing" temperature is raised. The relaxation of the network will change the bond angle and bond length distributions within the glass, leading to a decrease in free volume and possibly the polarizability. Before relaxation, the structures may be highly polarizable, giving rise to the high dielectric constants observed. In contrast to this is data on the dielectric constant of glasses formed under pressure which indicate that the dielectric constant increases with the increase in density.

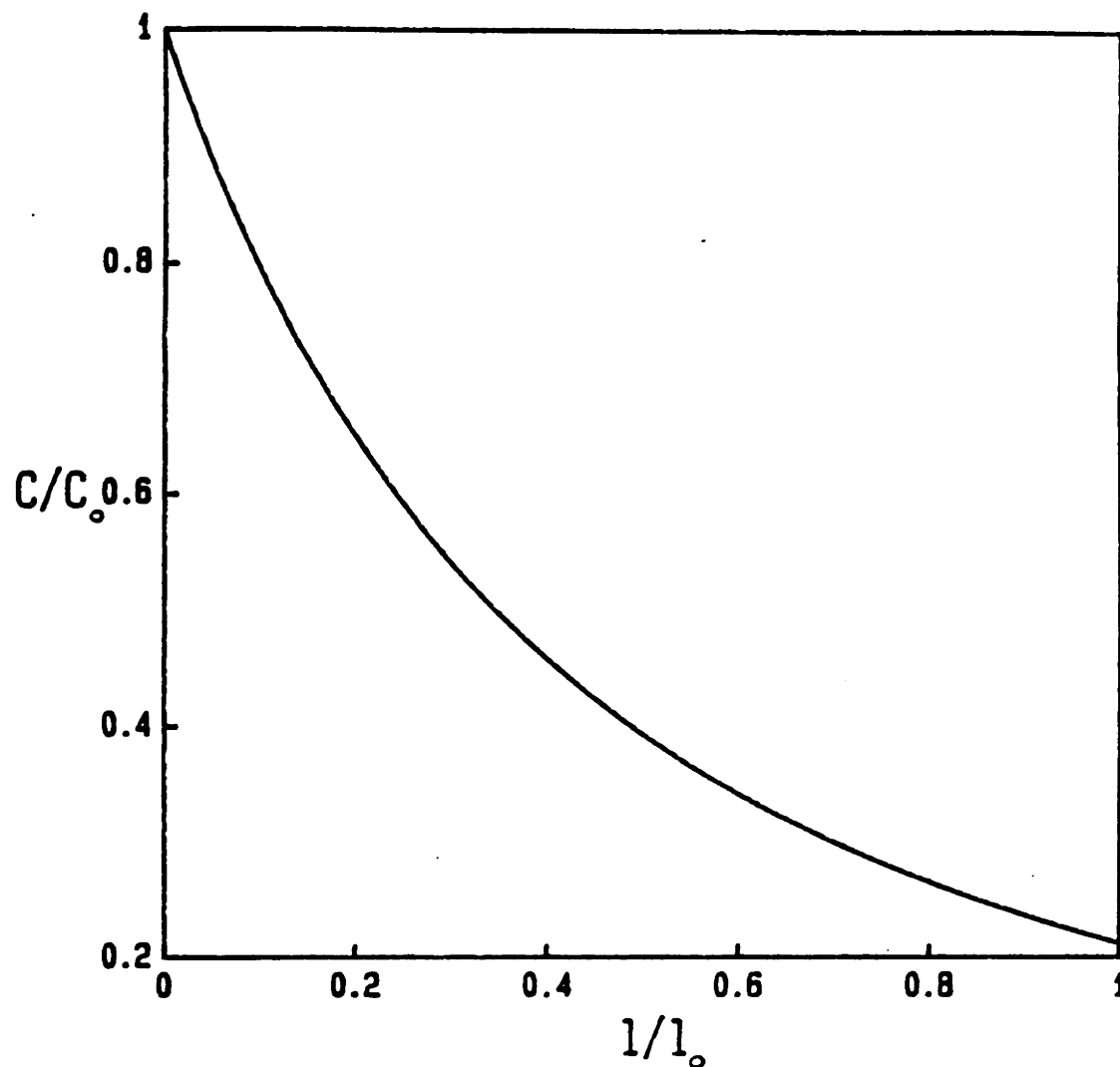


Figure 4.4.4

Model of capacitance as a function of shrinkage where densification occurs due to the elimination of spherical pores, and the dielectric constant of the skeletal material does not change. The capacitance and thickness of the device have been normalized by the capacitance of the fully dense material.

However, the latter data is probably due the increase in the density of polarizable ions as the density of the material increases, with little change having occurred in the bond lengths and angles. Very large changes in these distributions that may occur during the large changes in fictive temperatures possible in gel materials may overwhelm the density effect just mentioned. Clearly, however, there is not enough data on this phenomenon in gels to establish its cause at this time.

There is no discontinuity in the dielectric data as the film crystallizes. This is not surprising in light of the fact that neither the density, the dielectric constant nor the refractive index of anodic and vapor deposited films have been reported to change appreciably upon crystallization.

Unfortunately, while it may be desired to have a film of very high dielectric constant, films fired to temperatures below 600 C were prone to breakdown at relatively low bias voltages. Figure 4.4.5 shows the fraction of devices that broke down at applied fields less than 4 megavolts per cm as a function of the firing temperature. These breakdowns are characterized by instantaneous decreases in the capacitance (fig. 4.4.6) and simultaneous increases in the leakage currents of the MIS devices (fig. 4.4.7). Capacitance-voltage scans of broken down devices show that the capacitance of these devices is less than it was at the same bias voltage before breakdown. Examination of the gate electrodes after they had broken down revealed no craters or other blemishes of the type reported elsewhere [84, e.g.].

The DC leakage current on devices made without the passivating silica layer was also measured (fig. 4.4.8, e.g.). For an average device fired for one hour at 800 C, the leakage current was  $1.45 \times 10^{-7}$  amps/mm<sup>2</sup> at an applied field of 0.7 megavolts per centimeter. The value

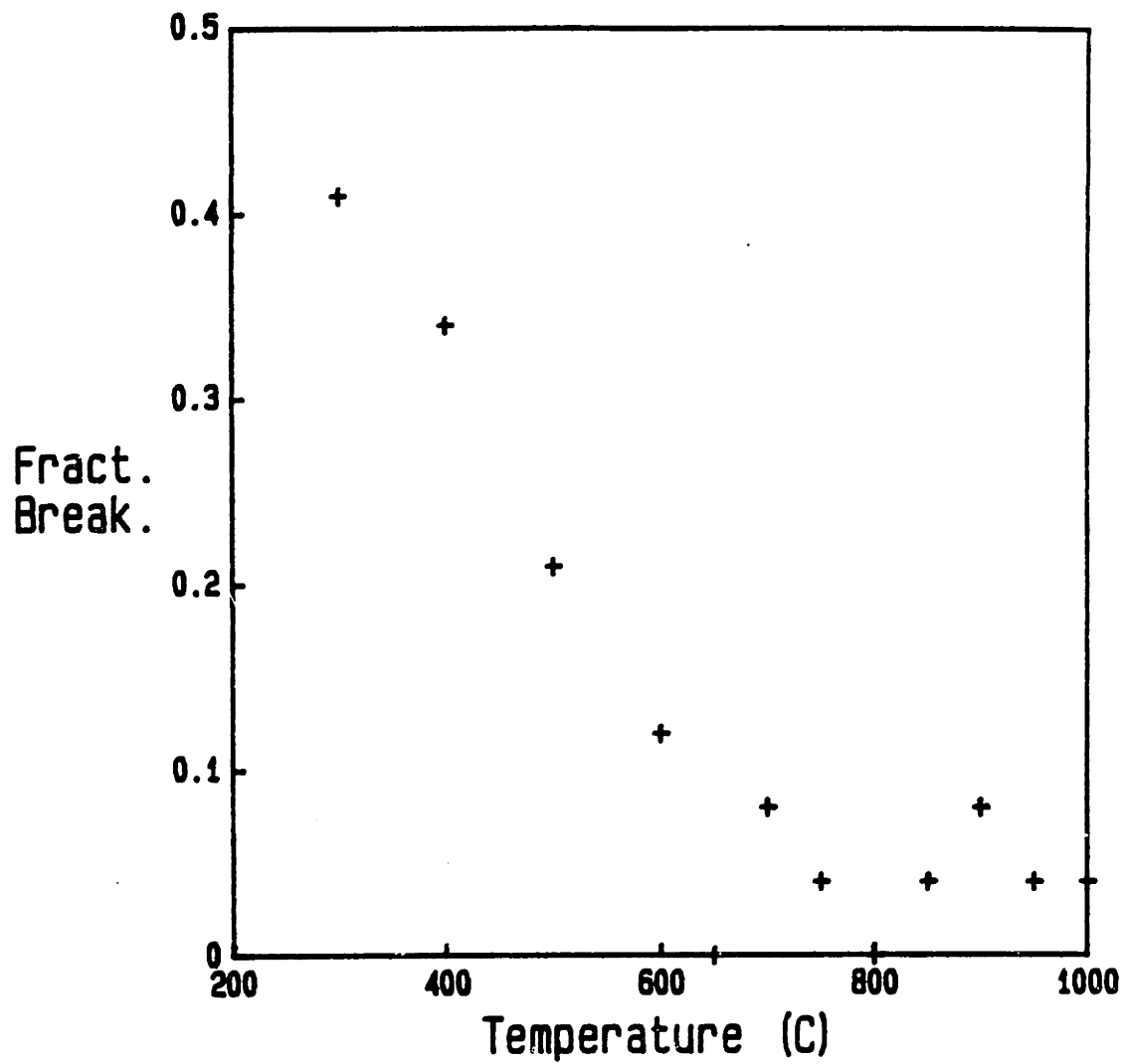


Figure 4.4.5  
Fraction of MIS devices that broke down at applied biases  
less than 4 MV/cm as a function of the firing temperature.  
all films were fired for 1 hour.

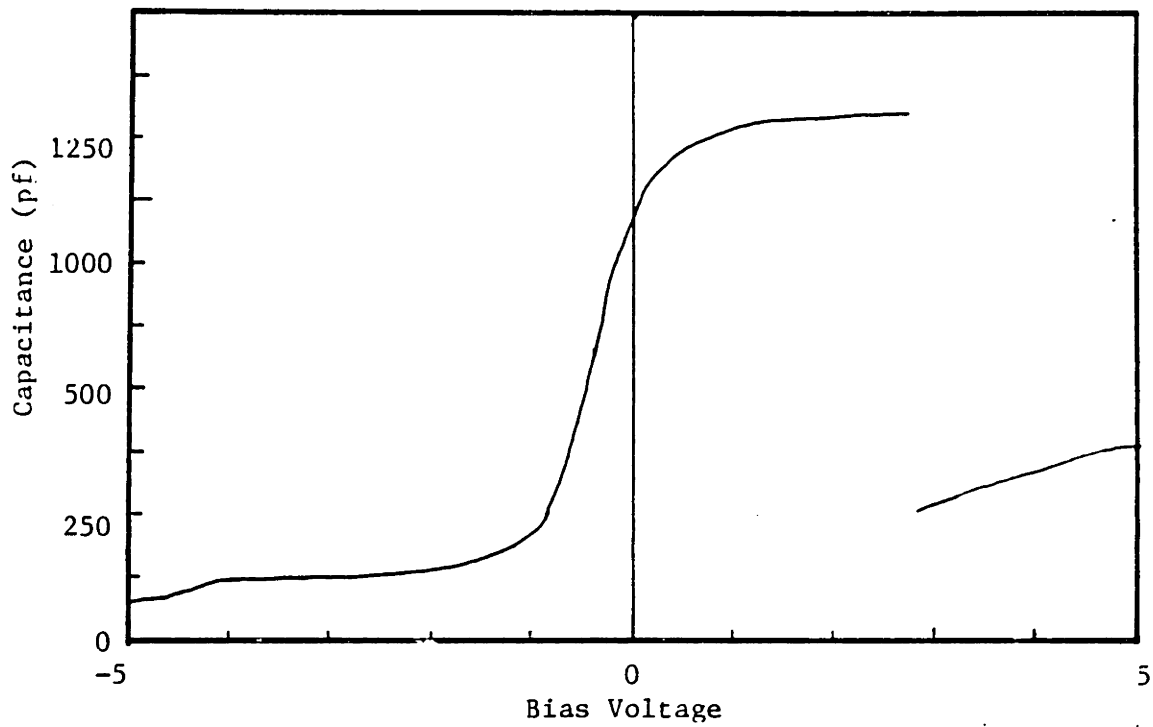


Figure 4.4.6  
Capacitance-voltage plot for device fired at 300 C for 1 hour.  
Breakdown is seen at 2 MV/cm.

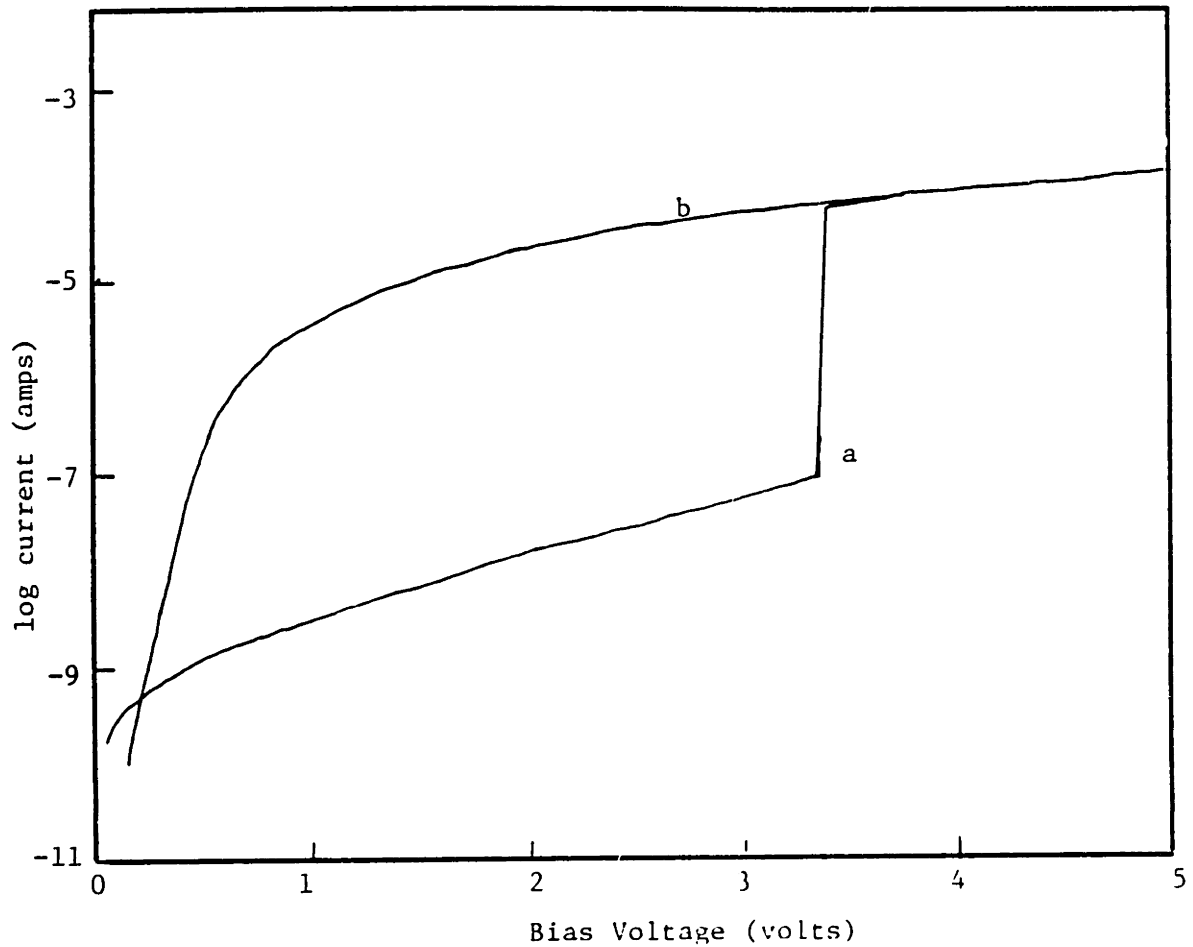


Figure 4.4.7  
Current-voltage plot for device fired at 300 C for one hour.  
First scan (a) shows breakdown at 2.5 MV/cm. Second scan (b)  
shows that the breakdown is irreversible.

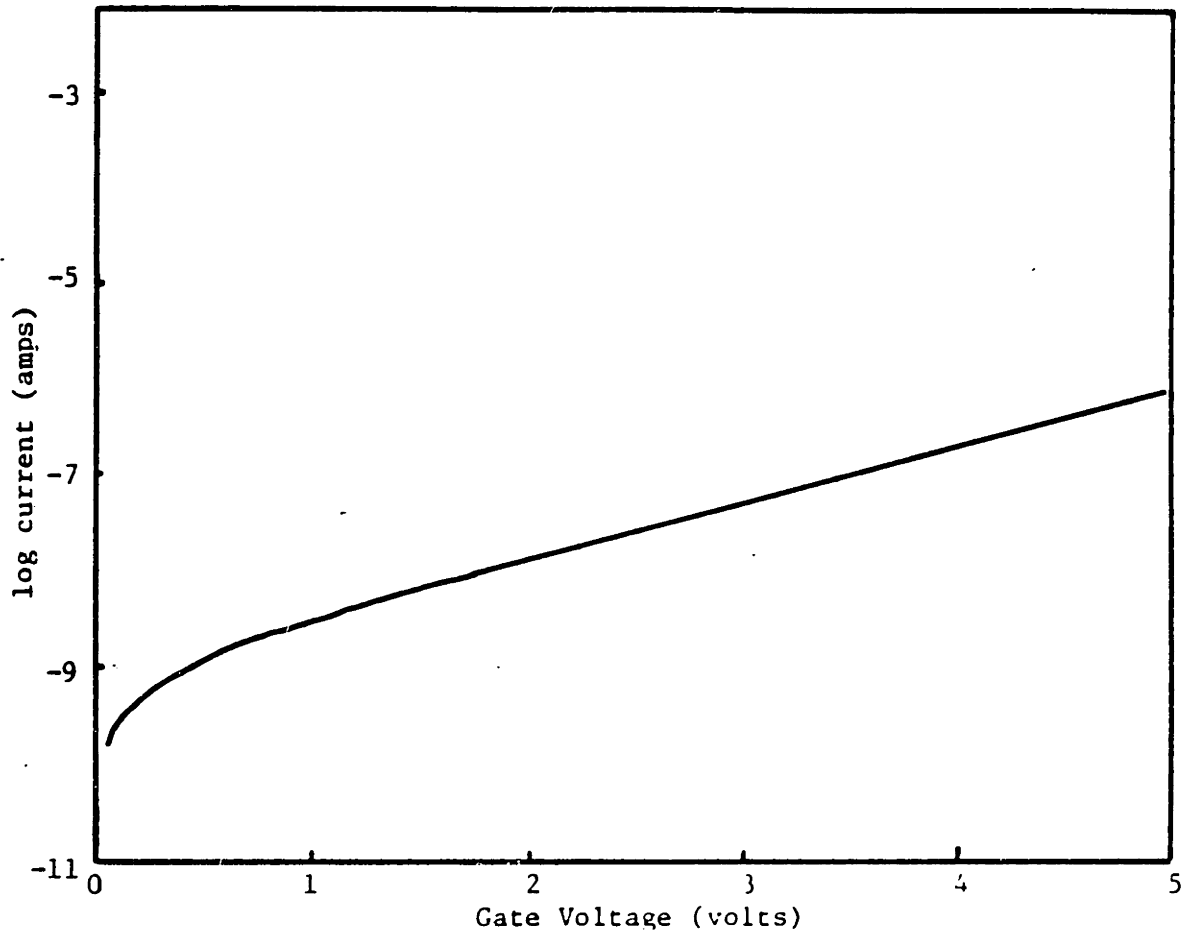


Figure 4.4.8  
Current-voltage plot for device fired at 300 C for one hour.  
No breakdown is observed.



reported for thermally oxidized tantalum MOS structures [16], is  $6 \times 10^{-7}$  amps/mm<sup>2</sup>. The value for gel derived tantalum is comparable to, and in fact the smaller of the other.

Tantalum films with additions of 9 cation percent of either titanium or zirconium were examined using the same techniques as the undoped films. Figure 4.4.9 shows that when normalized to the dielectric constant after firing at 300 C, the data for both compositions essentially follow the data on undoped samples. After firing to 800 C for one hour, the dielectric constants of the titania and zirconia containing films were  $43 \pm 6$  and  $27 \pm 4$ , respectively. While the spread in the data indicates that there is not a significant difference between the undoped and zirconium doped films, the addition of titanium increases the dielectric constant almost 50 percent.

A similar temperature dependence of the measured capacitance for doped as for nominally pure films was observed (fig. 4.4.10). This is strong evidence that that these properties are functions of the molecular structure of the material, and that the same structural processes, e.g. relaxation of free volume, are occurring in all of these compositions. As with the nominally pure films, there was no observed change in the dielectric constant upon crystallization, even though the resulting material is probably two phases (refer to thermal analysis on powders). There is currently no data available on the dielectric properties of the binary tantalate compounds with which to analyse the data for a two phase material. However, the data is intriguing in that two crystalline phases evolved from one amorphous phase with no change in the macroscopic dielectric constant.

In short, the dielectric constant (30) and leakage currents of nominally pure tantalum compares favorably with values reported in the

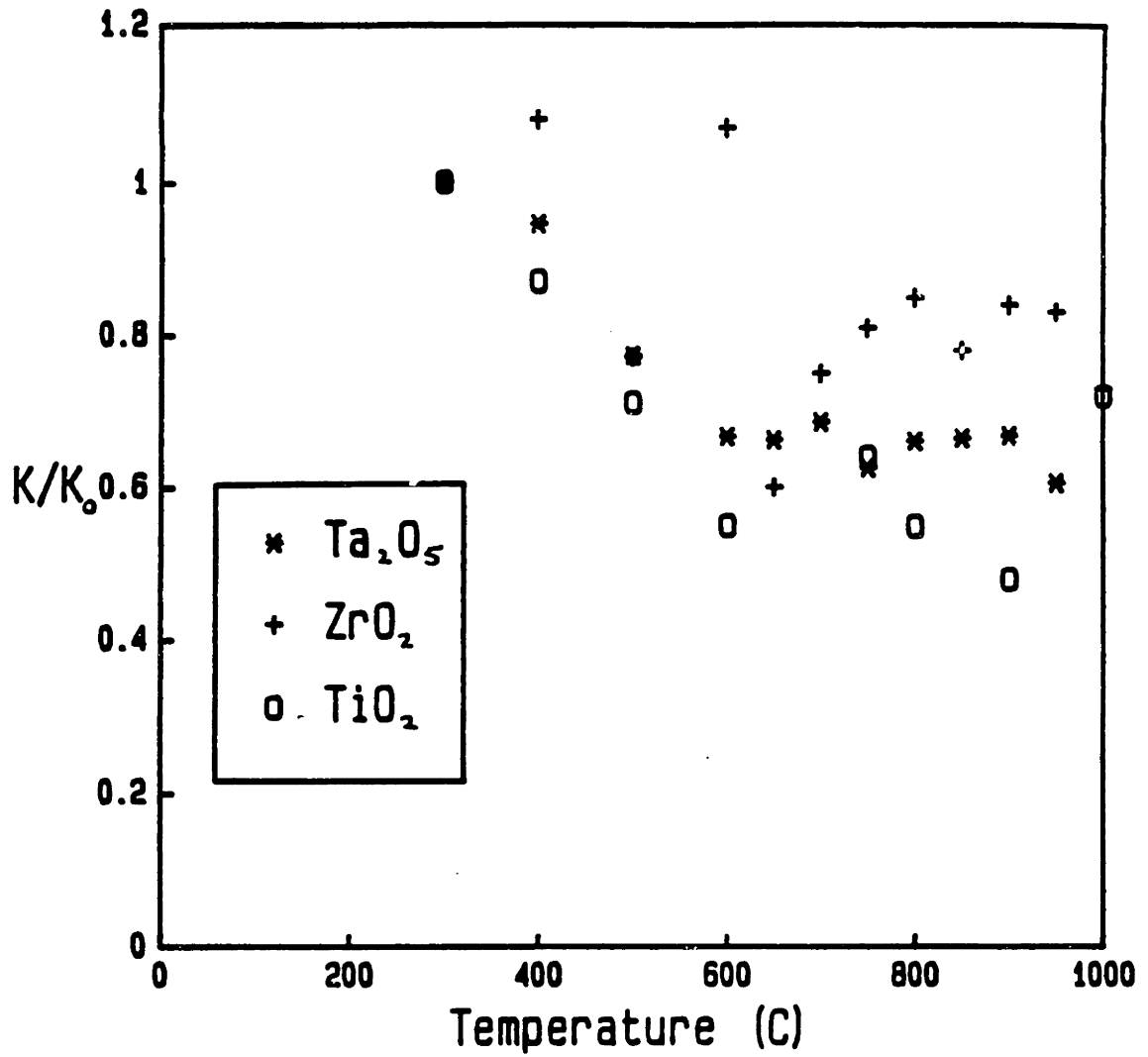


Figure 4.4.9

Dielectric constant of nominally pure tantala films and those containing 9% of either titania or zirconia. All data have been normalized by the dielectric constants of each composition at 300 C.

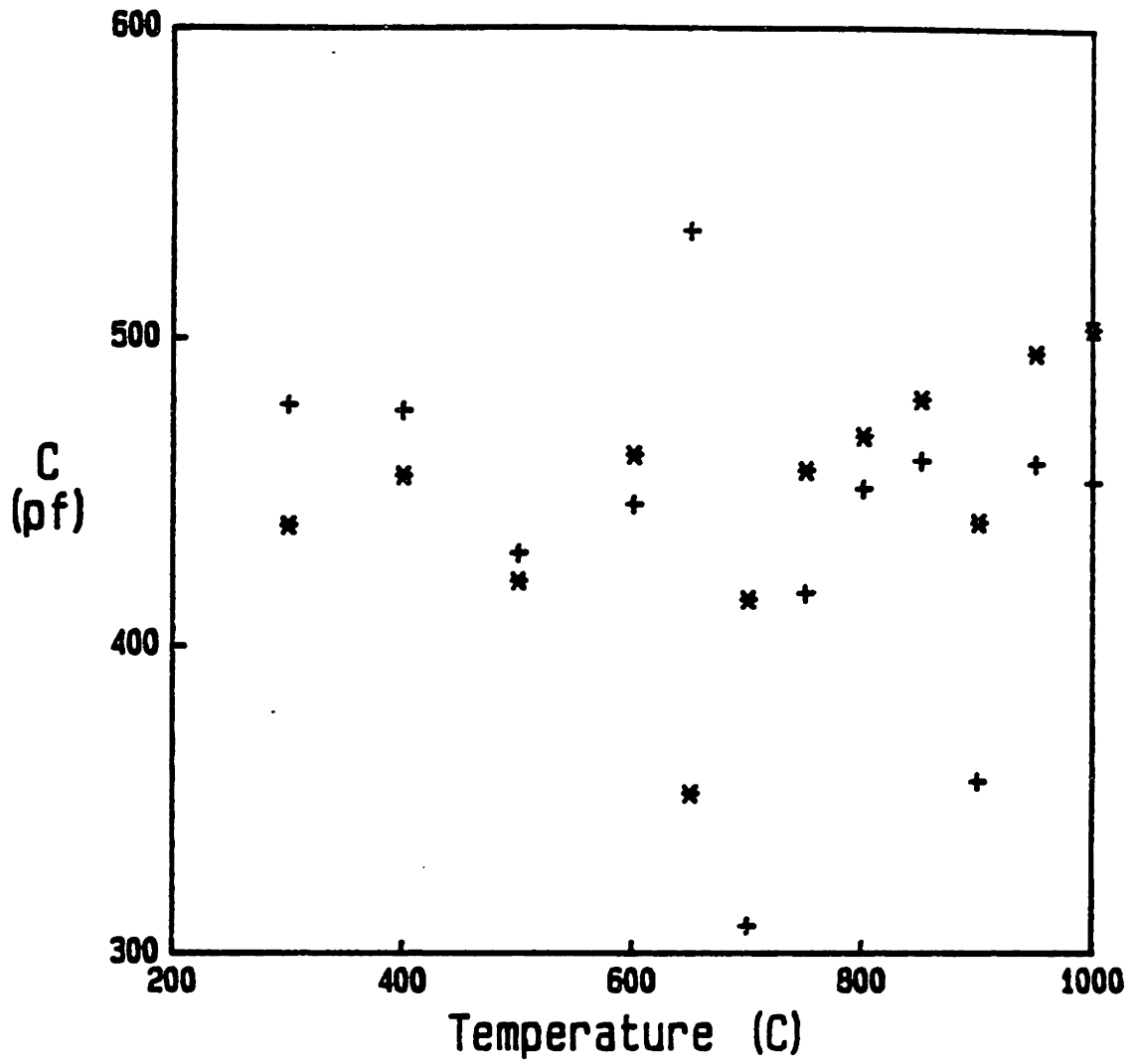


Figure 4.4.10  
Measured capacitance of tantalum gel films containing either  
9% titania or zirconia as a function of the firing  
temperature. All films were fired for 1 hour.

literature. The loss factor is a factor of 4.5 too high. Including titania in the films raises the dielectric constant to 46, whereas including zirconia does not make a large difference, if any.

#### 4.5. Chemical Passivation

As previously stated, this work was initiated after hearing of data suggesting that unfired sol-gel derived tantala films were adequate protection for aluminum substrates in the presence of wet chlorine. Attempting to reproduce this, copper foils were cleaned in dilute hydrogen peroxide, then dilute sulfuric acid and rinsed in deionized water. They were then dip-coated with tantalum ethoxide-based coating solutions, prepared as described earlier. The thicknesses of these films were not measured. Up to five layers were applied. Substrate protection was measured by floating both coated and uncoated foils next to each other on the surface of 0.5 molar sulfuric acid. Regardless of how many layers were applied, holes appeared in both coated and uncoated samples at identical times during the experiment. Most perforations occurred near the centers of the samples. If the model for adhesion presented earlier is valid, it would be difficult to wick the acid under the films to the centers of the samples instantaneously. This means that the acid was indeed probably penetrating the film.

Auger spectroscopy on the coated foil surfaces always revealed a copper signal, indicating that the substrate was indeed bare in some spots. These areas almost always corresponded to topographical defects in the foil such as sharp peaks, as identified using the SEM option on the instrument. The most likely explanation for this behavior is that

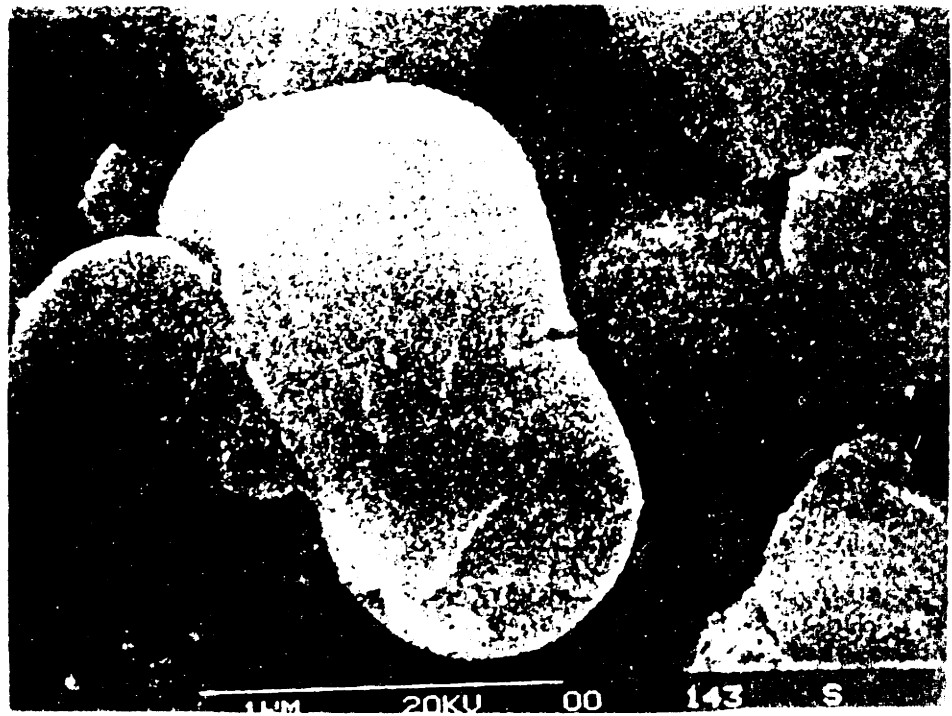
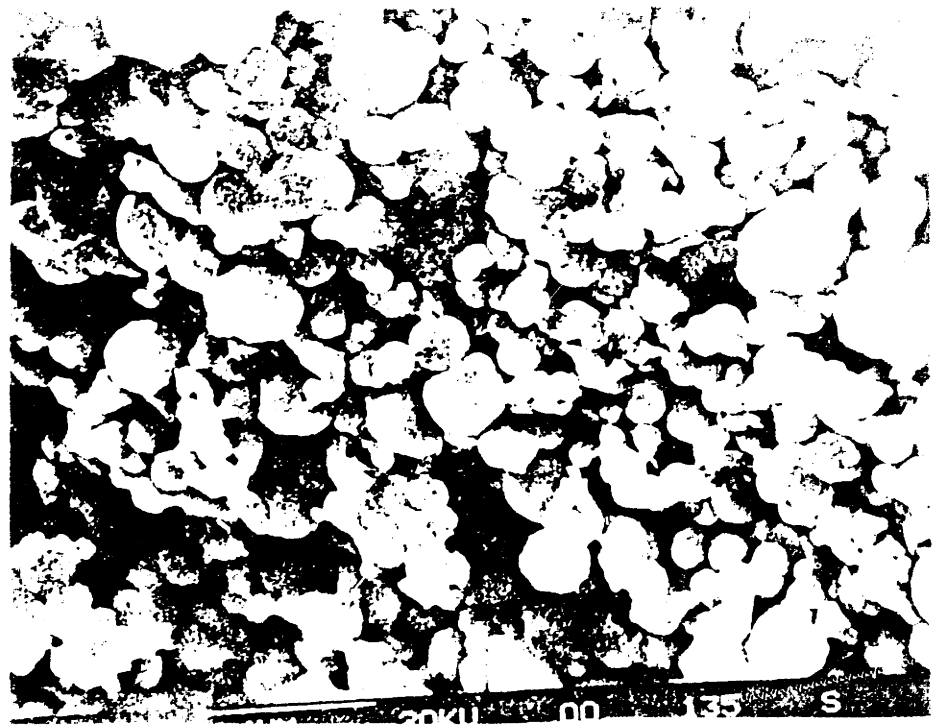
the cleaning procedure was not adequate to assure adequate wetting of the solution on all parts of the substrate.

Summarizing this section, the data presented here is inconclusive as to whether a barrier layer to chemical attack may be deposited from a tantalum ethoxide solution, as was demonstrated in a previous work [1].

#### 4.6. Powder Characterization

Thermogravimetric analysis (TGA) was performed on powders derived from the actual undoped tantala coating solutions in both oxygen and nitrogen at a heating rate of 10 C per minute. The powders as formed had a particle size of roughly 1 micron (fig. 4.6.1). Runs made in both atmospheres showed two major features - a large weight loss below 250 C, a slow continuous loss up to 400 C, and a smaller weight loss at 730 C (fig. 4.6.2). In addition, runs made in oxygen showed small weight gains between the temperatures 450 and 730 C. As results from both atmospheres are virtually indistinguishable on the scale of the figure, only the oxygen atmosphere firing is shown. The powder was dark grey after firing to 1000 C in nitrogen; but if fired subsequently to the same temperature in oxygen, it turned white. Powder originally fired to 1000 C in oxygen was white, and did not revert to the grey color if then fired in nitrogen. The total weight loss was independent of firing atmosphere to the accuracy of the measurement, indicating either that very small amounts of carbon or reduced tantalum caused the grey color, or that suboxides of tantalum may be volatilizing in the sample fired in nitrogen.

Differential thermal analysis (DTA) was also performed at a heating



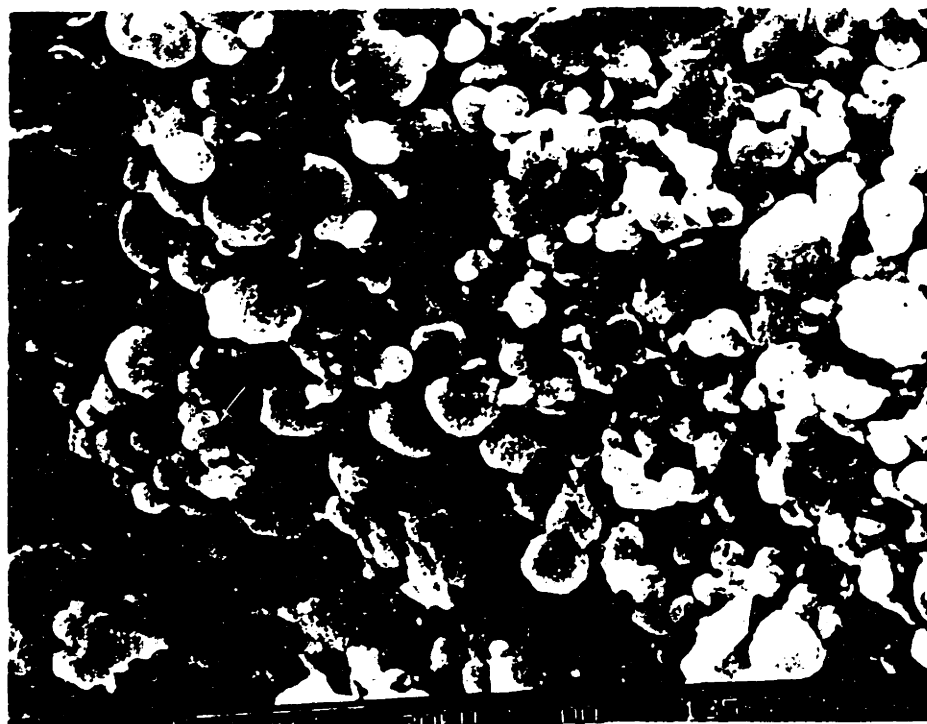


Figure 4.6.1  
Scanning electron micrograph of unfired tantalum gel powder.  
Scale bars are (a) 4 microns and (b) 1 micron.

INTENTIONAL DUPLICATE EXPOSURE

rate of 10 C per minute in both nitrogen and oxygen atmospheres. Both thermograms had two common features - a large broad endotherm between room temperature and 250 C, and a smaller sharp exotherm at 730 C in oxygen and 735 in nitrogen (fig. 4.6.3). In runs carried out in an oxygen atmosphere, however, there was an additional small exotherm between 250 and 400 C and a small broad exotherm between 600 and 700 C. Thermograms of samples fired in oxygen which were initially fired to 1000 C in nitrogen were indistinguishable from the second runs of samples fired both times in oxygen: both were featureless. As before, samples fired in nitrogen were grey, while those fired in oxygen were white.

Analysis of the effluent gasses by FTIR was performed while heating some samples under flowing oxygen in an alumina boat at the same heating rate as the previous DTA and TGA experiments. The first broad endotherm/weight loss corresponds to the evaporation of adsorbed ethanol (as indicated by the C-H vibration in fig. 4.6.4) and water (fig. 4.6.5). Between 200 and 300 C, the absorption in the fingerprint region between 800 and 1200  $\text{cm}^{-1}$  changes. Below 200 C, there are two distinct peaks, one centered at 900 and the other just below 1100  $\text{cm}^{-1}$  (fig. 4.6.6), identical to the published pattern for gas phase ethanol [85]. As the temperature is raised, a peak centered at 950  $\text{cm}^{-1}$  appears and quickly overpowers the other two (fig. 4.6.7). At the same time, a shoulder might be appearing in the high frequency side of the C-H stretch peak. These data indicate that some dehydration of the ethanol is occurring, catalysed by either the alumina boat or the tantalum oxide powder itself.

Two dehydration reactions have been shown in the literature [86]. The first is the dehydration of the alcohol to ethylene and water.



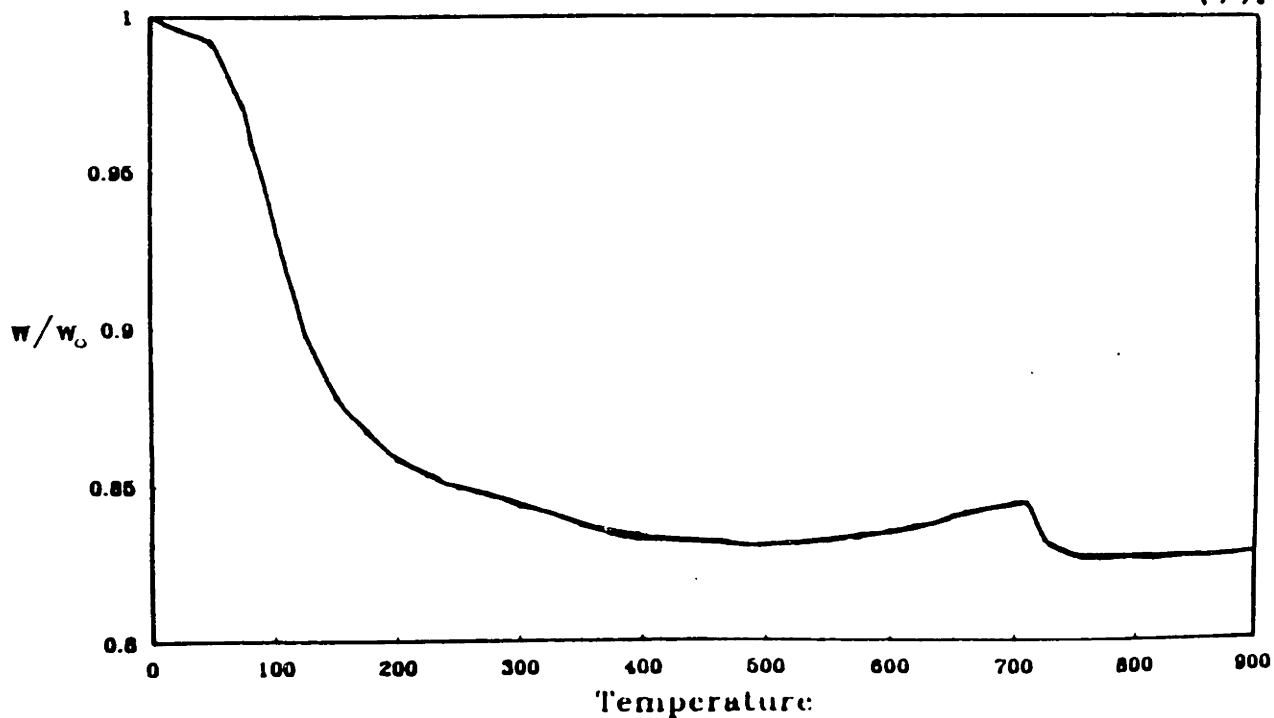


Figure 4.6.2  
 Thermogravimetric analysis of nominally pure tantalum gel powder.  
 The heating rate was 10 C/min in an oxygen atmosphere.

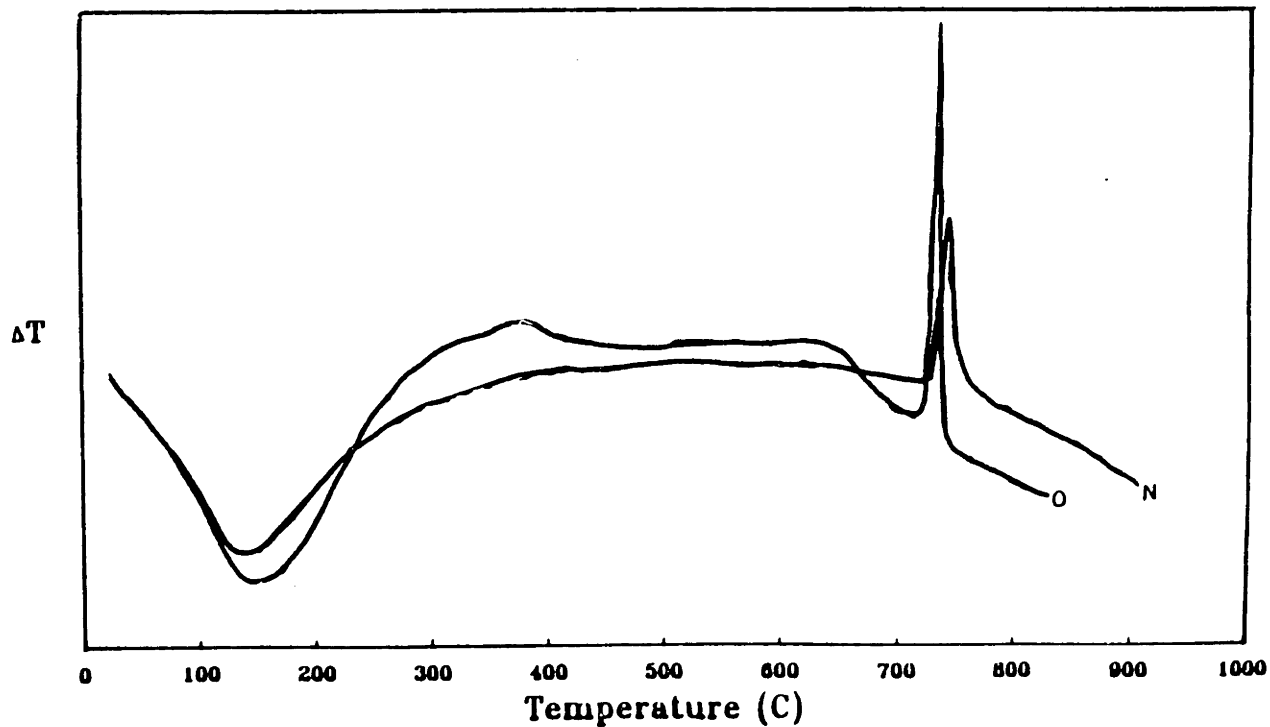


Figure 4.6.3  
 Differential thermal analysis of nominally pure tantalum gel powder. The heating rate was 10 C/min in an atmosphere of (O) oxygen or (N) nitrogen.

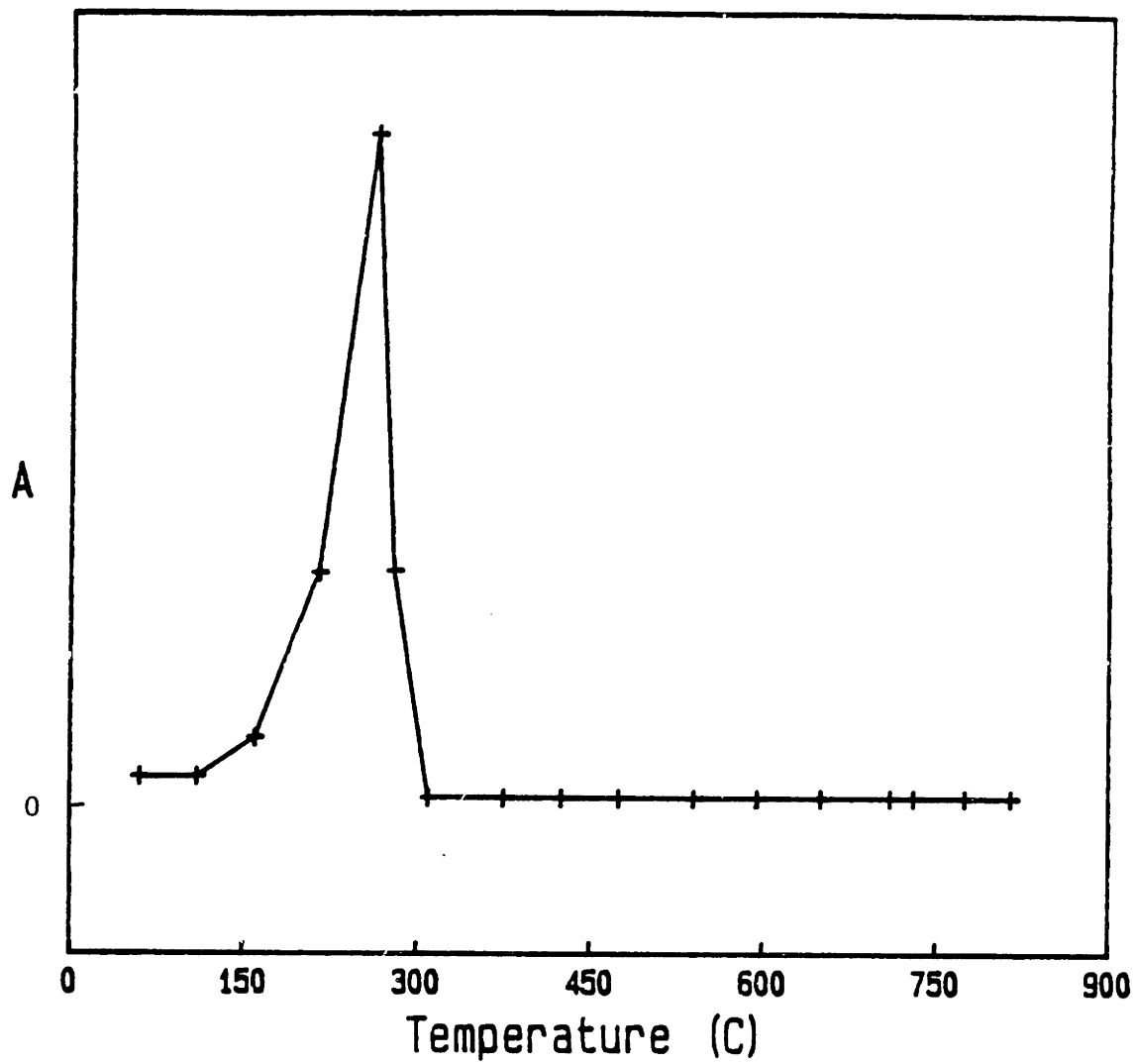


Figure 4.6.4  
Absorption of C-H stretch in effluent gases as measured using  
FTIR spectroscopy as a function of sample temperature.

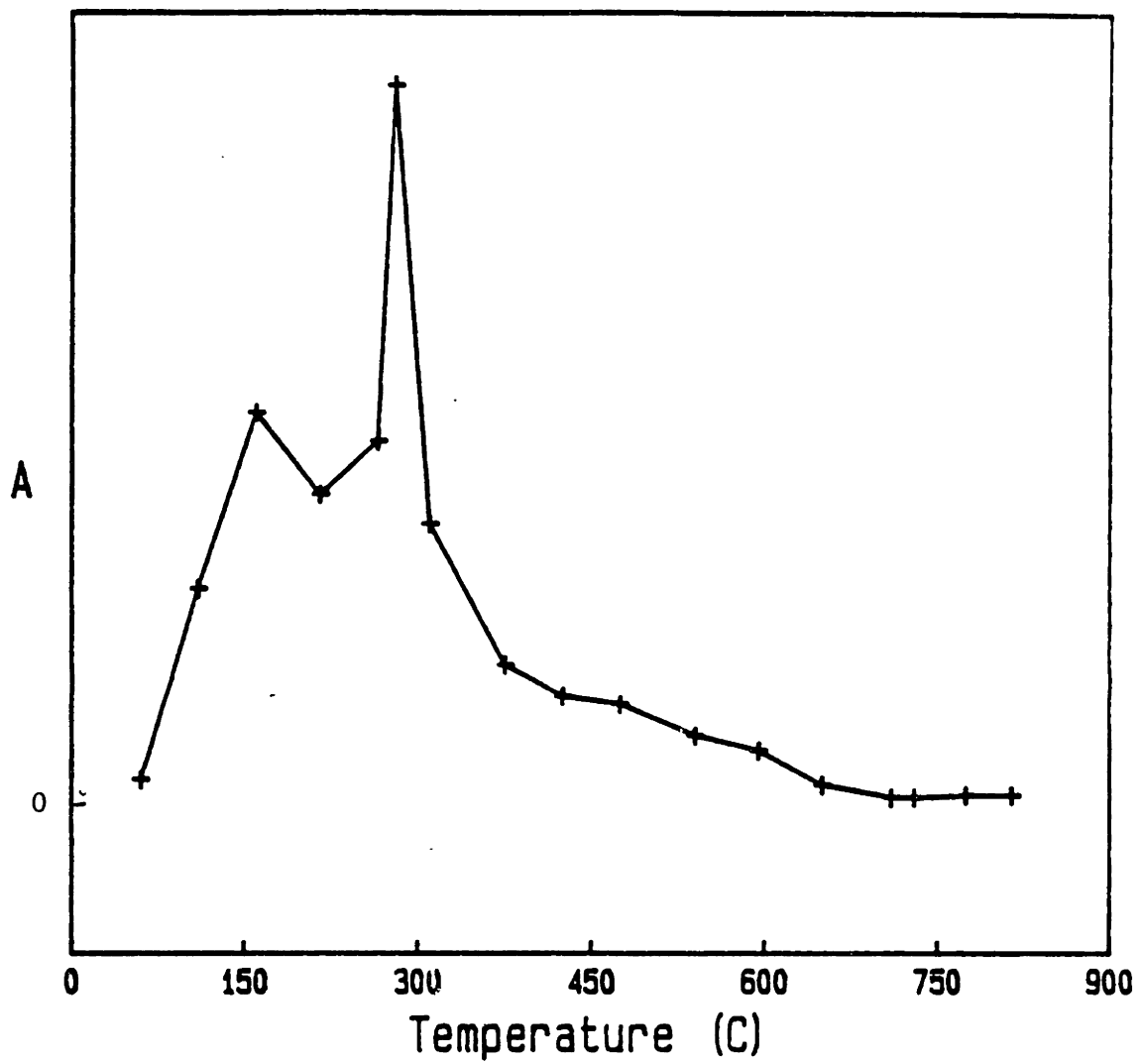


Figure 4.6.5  
Absorption of free H<sub>2</sub>O in effluent gases as measured using FTIR spectroscopy as a function of sample temperature.

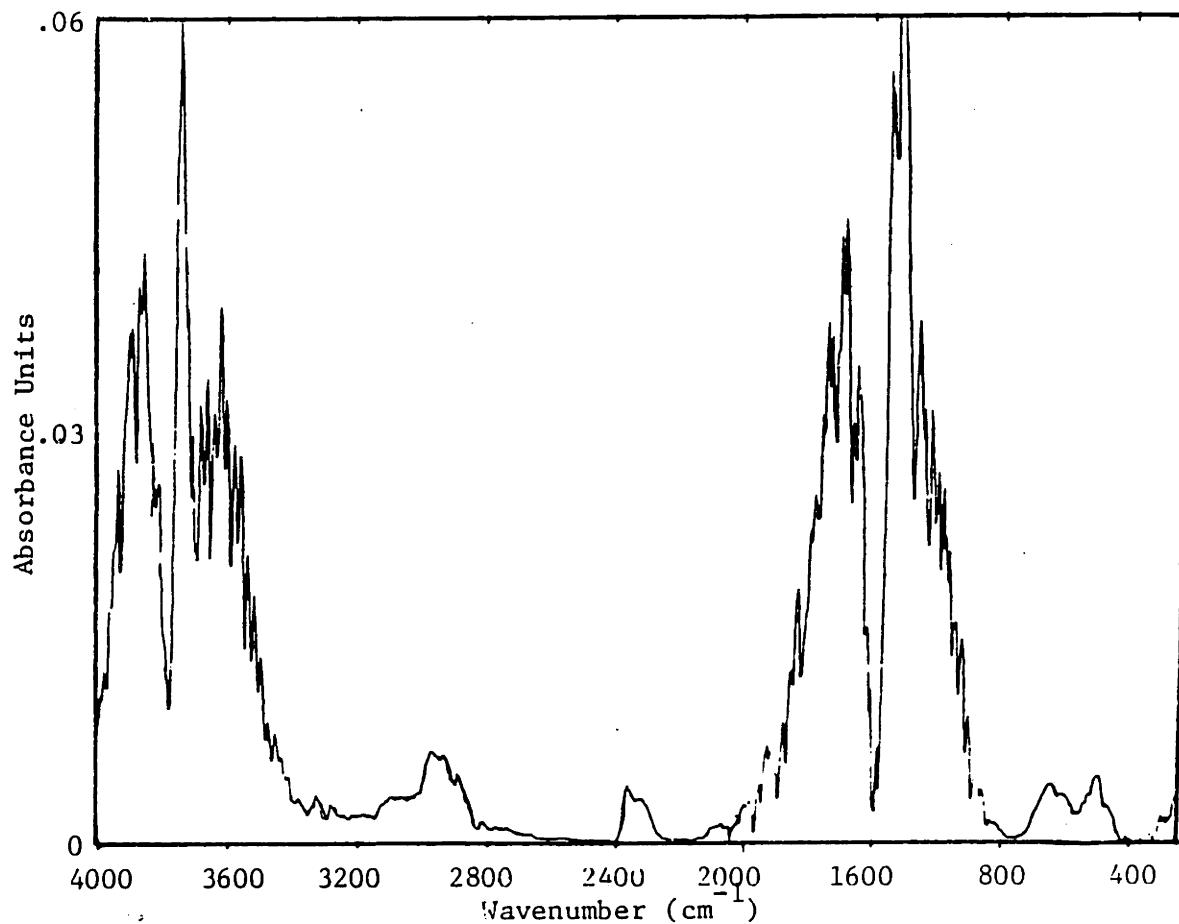


Figure 4.6.6  
Absorption vs. wavenumber spectrum obtained during FTIR analysis  
of effluent gases for a sample temperature of 200 C.

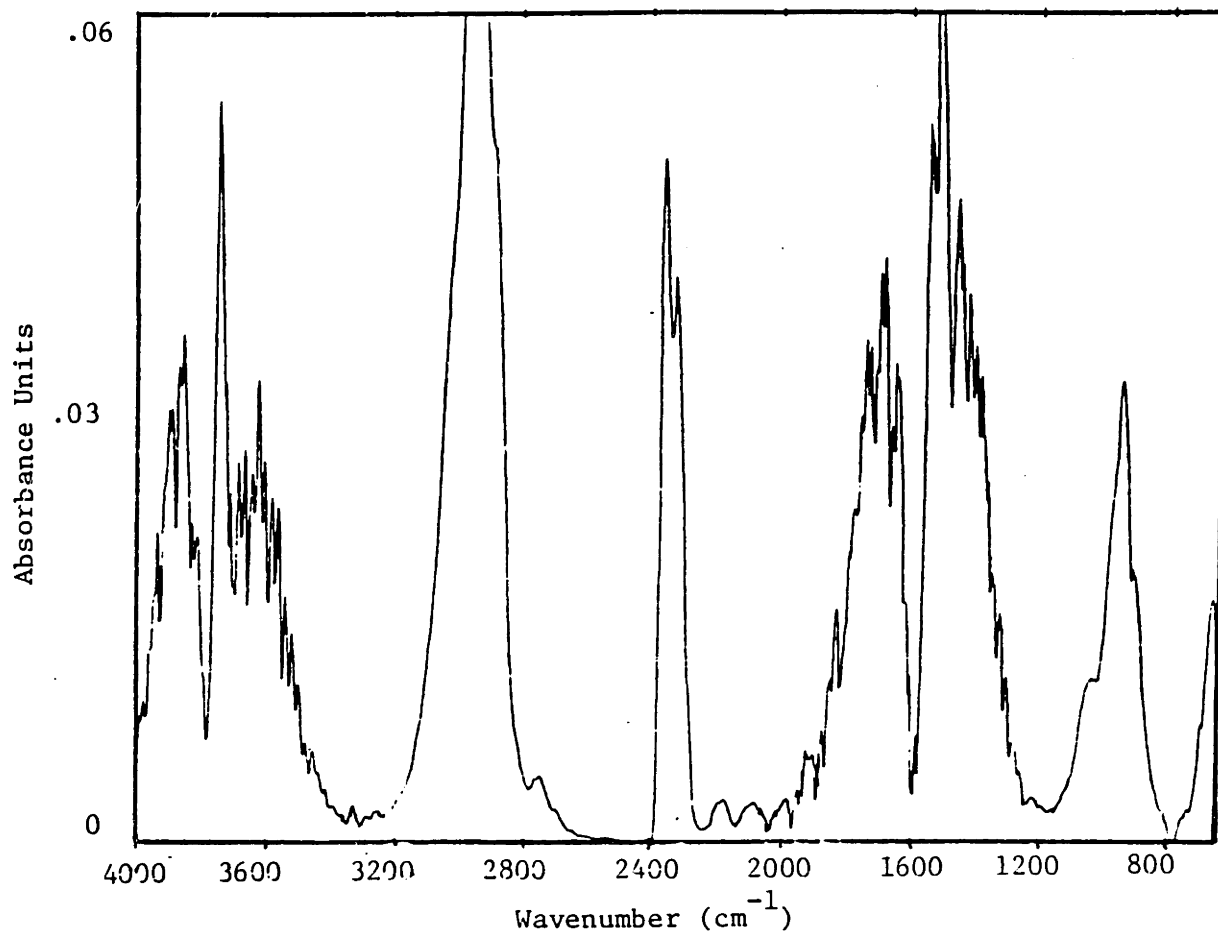


Figure 4.6.7  
Absorption vs. wavenumber spectrum obtained during FTIR analysis  
of effluent gases for a sample temperature of 300 C.

Homogeneously in the gas phase, this reaction takes place above 500 C. However, this reaction has been shown to occur at temperatures as low as 275 C over thoria; and alumina has been shown to catalyze this reaction as well. The second reaction is the formation of diethylether, which has been shown to occur at 120 C over some acidic ion exchange resins. The gas phase spectra of diethylether shows a strong absorption at  $1130\text{ cm}^{-1}$ , and a weaker one at  $1080\text{ cm}^{-1}$  [85]. Ethylene, on the other hand, has a strong absorption at  $940\text{ cm}^{-1}$ . It would also result in the formation of a shoulder in the aliphatic C-H stretch peak at roughly  $2500\text{ cm}^{-1}$ . This matches the data quite well. Therefore, the ethylene is forming either in the powder or when the gas comes in contact with the alumina boat. The former is more plausible due to the vast difference in surface area between the boat and the powder; and much surface would be required to catalyze the reaction to this extent. At 300 C, the absorption due to the C-H bond stretch disappears completely to be replaced by water and carbon dioxide absorption (fig. 4.6.8), which gradually decrease in magnitude until 400 C. Between 400 and 600 C, the effluent gases contain small amounts of both water and carbon dioxide. However, at roughly 650 C a moderate amount of carbon dioxide is given off, decaying until roughly 730 C where the amount given off increases by more than a factor of 10. The concentration of  $\text{CO}_2$  was so high in all of the samples run that the transmittance was reduced to zero, making the calculation of relative concentration impossible. The value shown in the figure for this temperature is a minimum possible value. The implications of these results will be discussed after the presentation of TGA data.

X-ray powder diffraction analysis of powders heated in either oxygen or nitrogen at 10 degrees per minute to 650 C and immediately

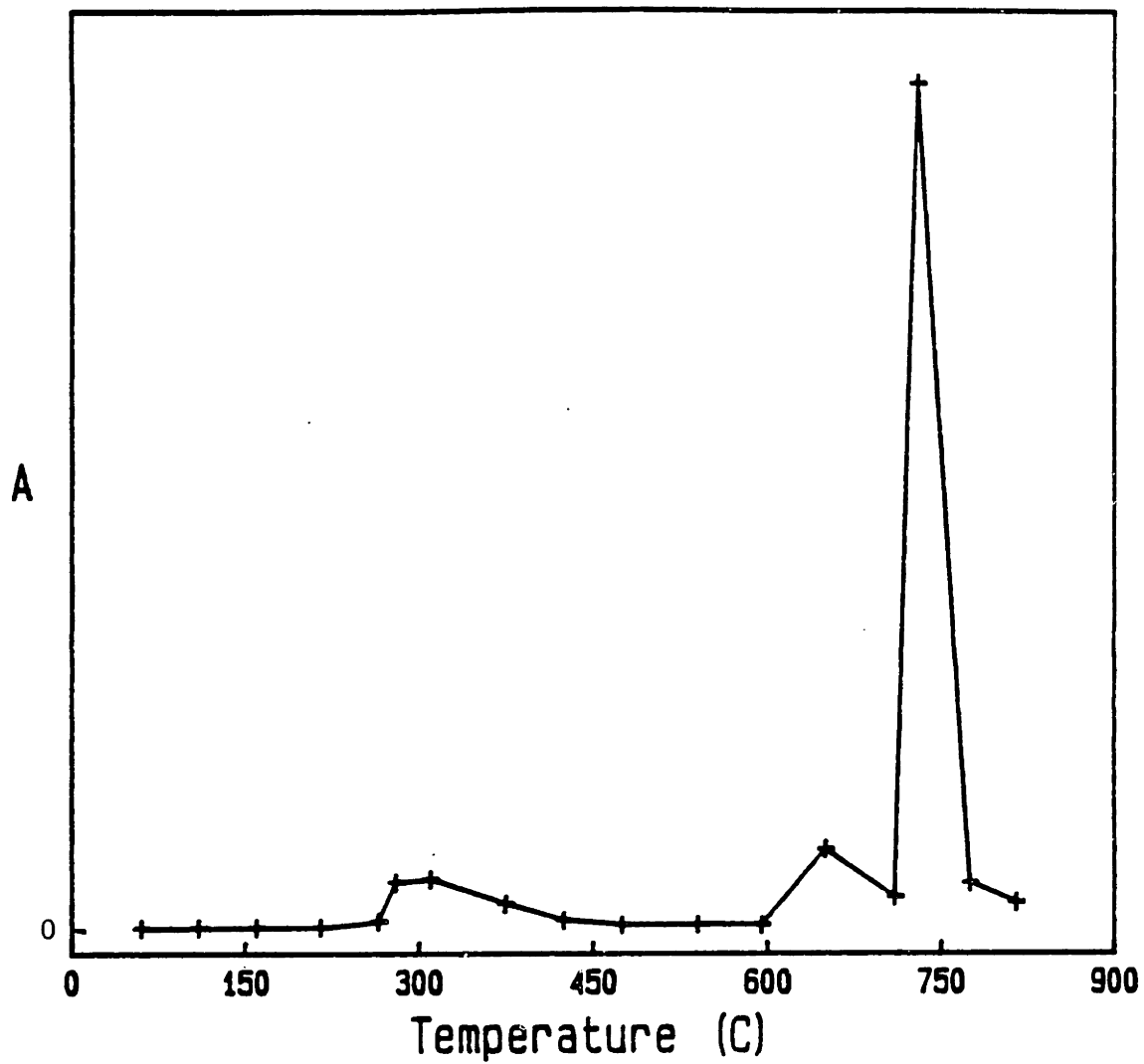


Figure 4.6.3  
Absorption of CO<sub>2</sub> in effluent gases as measured using  
FTIR spectroscopy as a function of sample temperature.

cooled reveal no crystallinity (fig. 4.6.9). When compared to samples heated to 800 C, it is revealed that crystallization occurs between these two temperatures. The diffraction pattern from the powder heated to the higher temperature was that of pure beta-tantalum oxide. Crystallization is an exothermic process, and was shown to occur in both nitrogen and oxygen atmospheres. The only exotherm evident in the nitrogen atmosphere DTA data is that at 730 C. Therefore this exotherm must correspond to crystallization.

Thermal analysis was also performed on tantalum oxide powders containing between 5 and 50 cation percent of several second oxide components. As in the single component samples, the DTA traces showed large endotherms below 250 C followed by small exotherms if heated in oxygen. However, the large sharp exotherm at elevated temperatures was seen to shift between 708 and 820 C. The exact temperature of this exotherm depends greatly on the composition of the powder (table 4.6.1). X-ray diffraction analysis of samples heated to just below and just above these exotherm temperatures showed that the sharp exotherms clearly accompanied crystallization. Not surprisingly, the multicomponent samples displayed the diffraction patterns of the corresponding binary tantalate in addition to the beta tantalate, with the exception of the alumina doped samples. This is due to the very low solubility of the second component oxides in tantalum oxide, and the formation of superstructure phases as mentioned earlier. The results obtained in this study agree completely with the published phase diagrams as to which phases should be present.



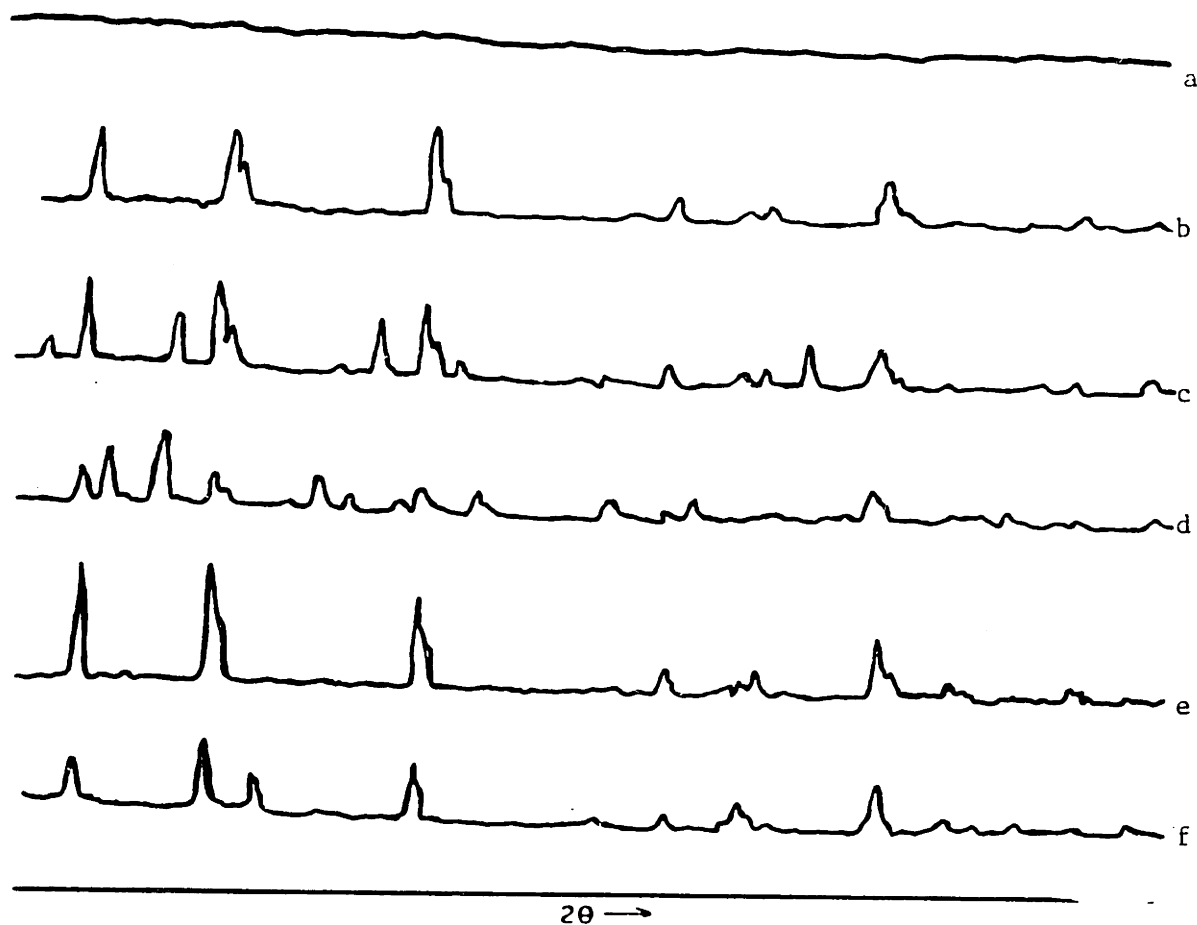


Figure 4.6.9

X-ray powder diffraction patterns for (a) nominally pure tantalum gel powder fired to 650 C at 10 C/min then rapidly cooled, (b) nominally pure tantalum gel powder fired to 300 in same fashion as (a), (c) gel containing 9% magnesia fired as (b), (d) gel containing 9% titania fired as (b), (e) gel containing 9% alumina fired as (b), gel containing 9% zirconia fired to 900 in same fashion as (b).

Table 4.6.1.

DTA data on temperatures of crystallization exotherms  
in degrees C as a function of powder composition.

	5%	9%	Binary
Undoped	736		
Alumina	771	822	none (50%)
Magnesia	758.	786	738 (33%)
Titania	744	763	771 (33%)
Zirconia		838	708 (33%)

In all cases the crystallization exotherms were quite sharp (fig. 4.6.10). Therefore, because inhomogeneities in the powder composition are expected to cause crystallization over a range of temperatures, the sharpness of the crystallization exotherms indicates that the powders were quite uniform in composition throughout.

The temperature of crystallization of multicomponent systems has been shown to change the 730 C value that was observed for the single component oxide powder. Crystallization is a two step process, and depends upon both processes occurring - nucleation and growth. The temperature at which these individual steps occur is effected by the nucleation and growth rates of the specific phases crystallizing and the viscosity of the glass. As soon as a second cation is added to the system, the phases identified after crystallization change, as mentioned earlier [11]. Therefore, one might expect the crystallization temperature to change. However, in a two phase field of the phase diagram, phases present do not change, only their relative amounts. Therefore, the change in crystallization temperature must be due to a change in the viscosity of the glass.

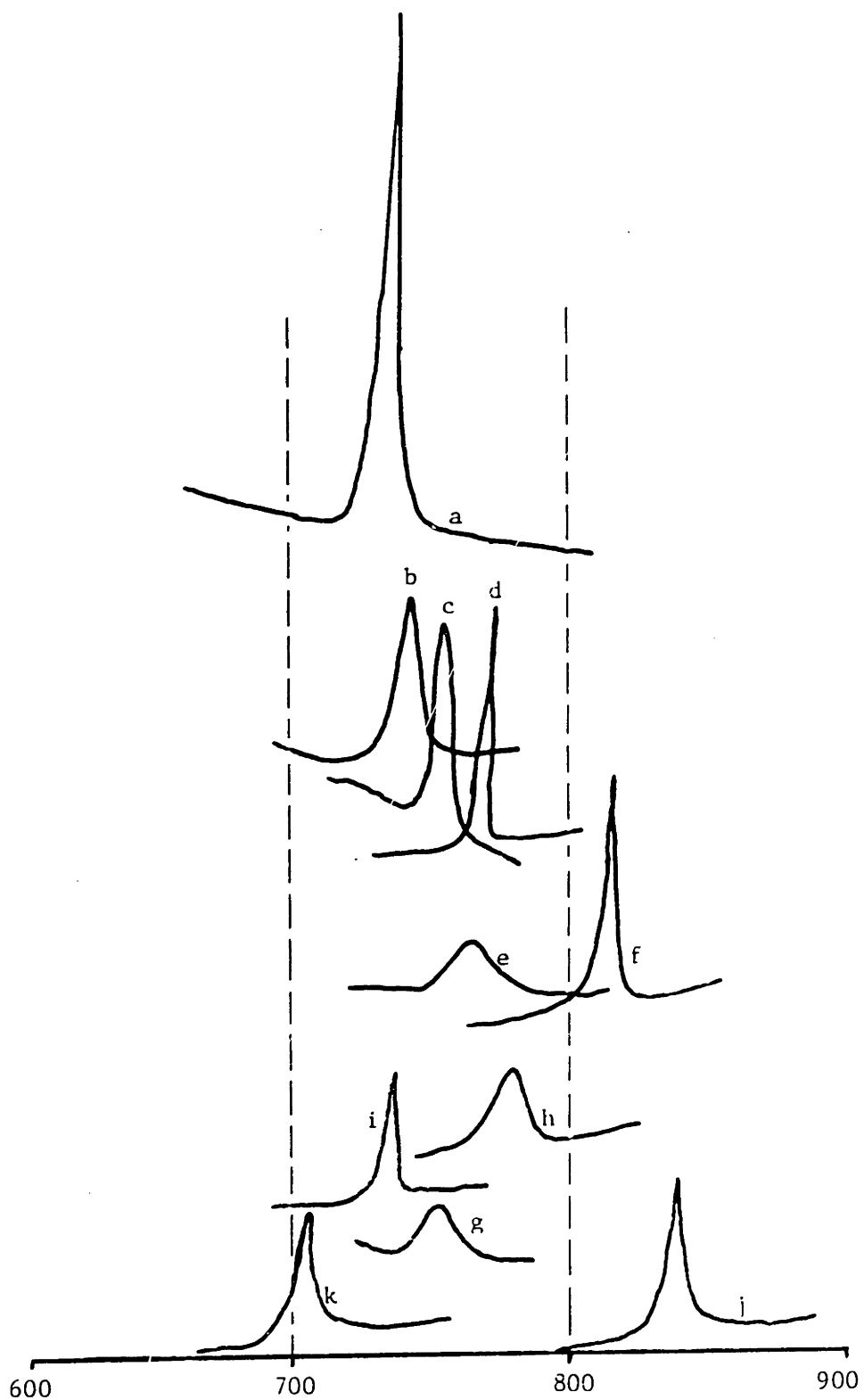


Figure 4.6.10

Crystallization exotherms observed in the DTA at a heating rate of 10 C/min in oxygen for (a) nominally pure tantalum gel, and gels containing (b) 5% titania, (c) 9% titania, (d) 33% titania, (e) 5% alumina, (f) 9% alumina, (g) 5% magnesia, (h) 10% magnesia, (i) 33% magnesia, (j) 9% zirconia, and (k) 33% zirconia.

The TGA traces of the multicomponent oxides fired in oxygen were quite similar to that of the undoped tantala. All showed a large initial weight loss below 250, continuing more slowly until between 470 and 630 C, depending upon the actual composition. Between these temperatures and the onset of a sharp high temperature weight loss, all samples were seen to gain weight. As with the DTA data, however, the highest temperature feature, in this case the sharp weight loss just mentioned, was seen to shift between 736 and 845 C, depending upon the composition (table 4.6.2).

Table 4.6.2.

TGA data on weight loss (W) and temperatures (T) corresponding to the ends of the weight change regions. Weight loss is given in percent of the original weight. Temperature is in degrees C.

	Initial loss		Oxidation		Crystallization	
	W	T	W	T	W	T
Undoped	-16.9	515	1.3	722	-1.6	739
Alumina, 5%	-18.0	525	1.1	730	-2.5	788
9%	-17.4	550	1.1	760	-0.9	815
50%	-28.8	630	0.1	715	none	none
Magnesia, 5%	-17.0	520	1.4	730	-2.8	767
9%	-17.3	555	0.9	750	-0.4	787
33%	-23.5	575	0.1	740	-0.1	785
Titania, 5%	-16.9	470	1.4	700	-2.1	743
33%	-21.9	425	0.5	605	-1.0	774
Zirconia, 5%	-18.9	575	0.6	710	-1.7	764
9%	-16.8	515	0.9	730	-0.3	845
33%	-28.3	535	0.2	690	-0.2	736

The processes occurring at various temperatures during heating become clear upon assimilation of all of the thermal analysis data. Both thermograms of samples fired in oxygen and those fired in nitrogen show the large endotherm below 300 C, indicative that the process occurring is anerobic. In addition, the major fraction of all the weight lost upon firing is lost over this temperature range. From the species

present in the effluent gas, we can clearly establish that evaporation of adsorbed species and additional condensation are taking place. The exotherm immediately following this endotherm is only present in thermograms of powders fired in an oxygen atmosphere, and corresponds to the first appearance of carbon dioxide, an increase in the water concentration and the disappearance of hydrocarbons from the effluent gases in the FTIR study. This evidence strongly suggests the oxidation of those hydrocarbons still evaporating from the powder.

The broad shallow exotherm just prior to crystallization is also only present in the runs performed in oxygen, and corresponds to the second burst of carbon dioxide as seen in the FTIR. This feature is also probably due to the oxidation of carbonaceous species, but this time the reactant species are non-volatile. This description can be justifiably applied to carbon (amorphous or graphitic) present on the surface of the powder grains. It also applies to carbon dissolved in, or present in discrete precipitates within, the powder grains. The mechanism responsible for the oxidation of carbon inside the powder grains is probably diffusion of one of the species, and assume this species to be oxygen for arguments sake. If we assume spherical powder grains, no porosity within the grains, the diffusivity of oxygen in the oxide to be independent of time and the concentration of oxygen in the matrix, good convection in the gas phase, a uniform distribution of reactant within the powder grain, and the boundary at which the reaction takes place is sharp and moves toward the center of the particle as the reaction progresses, one may use the solution to the classic shrinking-core moving boundary problem. The extent to which these assumptions are valid may be arguable, but this serves as an already solved example to

calculate the concentration of reaction products in the effluent gases. The amount of reactant, e.g. carbon, that remains within the grain is a function of time,

$$\frac{t}{\tau} = 1 - 3(1 - X_B)^2 + 2(1 - X_B) \quad (4.6.1)$$

where  $\frac{t}{\tau}$  is defined as the time of reaction normalized by the time when the particle is depleted of the reactant, and  $X$  is the fractional amount of material remaining in the particle. Plotting the amount of reactant remaining against the time normalized with the time at completion, one generates figure 4.6.11. The amount of reaction product that one expects to detect in the effluent gas is the negative of the change in the amount of reactant remaining in the particle with time, i.e.,

$$\left( \right)_{\text{effluent}} = - \frac{dX}{dt} \quad (4.6.2)$$

When this derivative is plotted against the normalized time, one obtains figure 4.6.12.

One first notices that the initial concentration of products in the effluent gas is predicted to be very high and then die quickly away. The rate of decrease will be determined by the diffusion coefficient at the temperature of interest. While this particular curve was generated using the analysis above, the overall form of a high initial concentration of products in the gas phase which decreases as the experiment progresses, is general to the case where diffusion of reaction products out of the particles is rate limiting. This form is also representative of the a scheme where the chemical reaction in the particle is rate limiting. An alternate explanation is this peak discussed above is due to the oxidation of carbon coating the outside of the particles. Either of these mechanisms seems equally valid.

The experimental results do not indicate that the concentration of

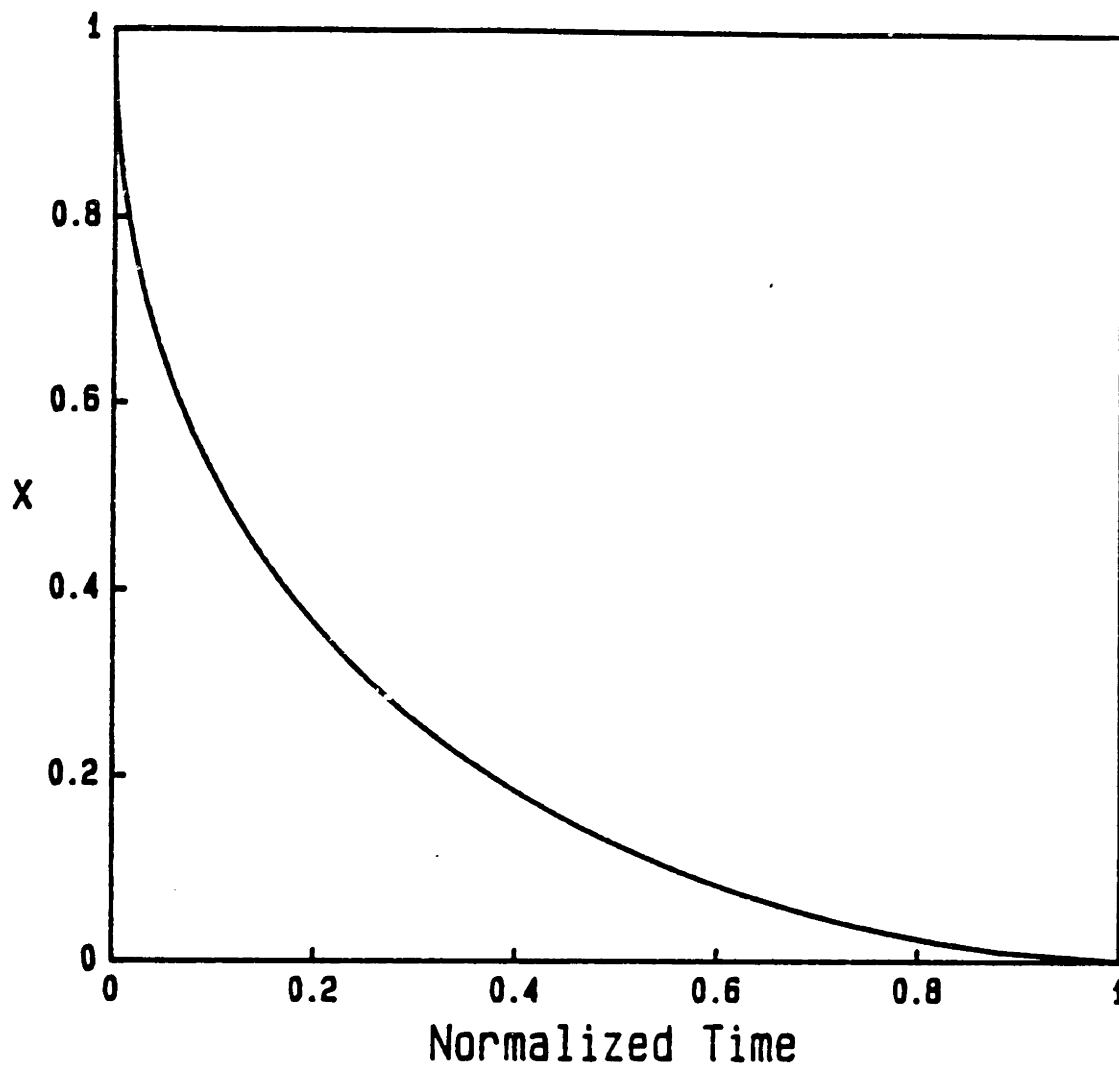


Figure 4.6.11

Model of diffusion controlled reaction in a spherical particle.  $X$  is the amount of B remaining in the particle normalized to the original amount. The time is normalized to the time until completion of the reaction.

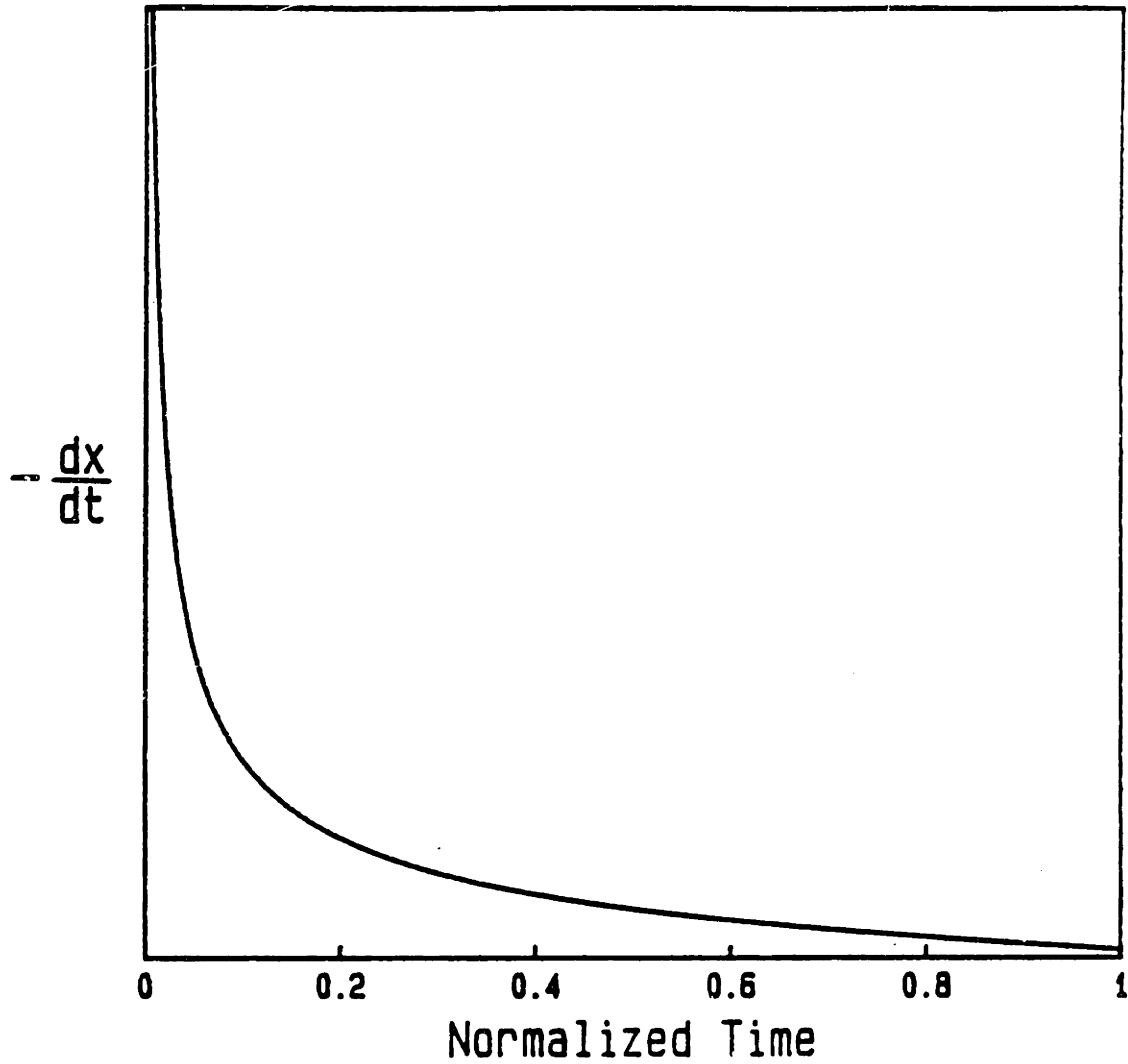


Figure 4.6.12

Model of diffusion controlled reaction in a spherical particle.  $-\frac{dx}{dt}$  is the amount of B expected in the effluent gases during the reaction. The time is normalized to the time until completion of the reaction.



reaction products in the effluent gases is reduced as quickly as predicted by any of the above models. This can be accounted for in several ways. First, the reaction products must be transported through a crucible of powder before being swept away by the flowing oxygen. Secondly, the powder grains are probably porous, accelerating the rate at which oxygen can be supplied to the reaction sites and the rate at which the reaction products can be removed. In addition, the model presented above implicitly assumed that the rate of diffusion is not a function of time. As the temperature is being raised at a constant rate in the experiment, the diffusion coefficient is also increasing. This serves to shorten the time at which depletion of the reactant is complete, hence increasing the concentration of reaction products in the effluent gas at later times in the experiment. In addition, having carbon in the network may produce an amorphous oxycarbide phase. If such a phase were to form, it would gain weight as it fully oxidizes between 450 C and the crystallization temperature. This would account for the weight gains upon heating in oxygen, as eluded to earlier.

The final feature in the DTA data correlates very well with events also seen in the TGA and FTIR experiments. It was noted that the temperature of the crystallization exotherms corresponded closely to the temperature at which this small weight loss occurred for all compositions except two (fig. 4.6.13). This in turn corresponded to the largest CO<sub>2</sub> concentration in the effluent gasses upon heating the undoped powder as determined by FTIR analysis. The most plausible explanation for this is that the carbonaceous species (carbon, CO<sub>2</sub> and CO, e.g.) dissolved in the oxide network or contained in pores are rejected at the crystallization front and eventually purged from the

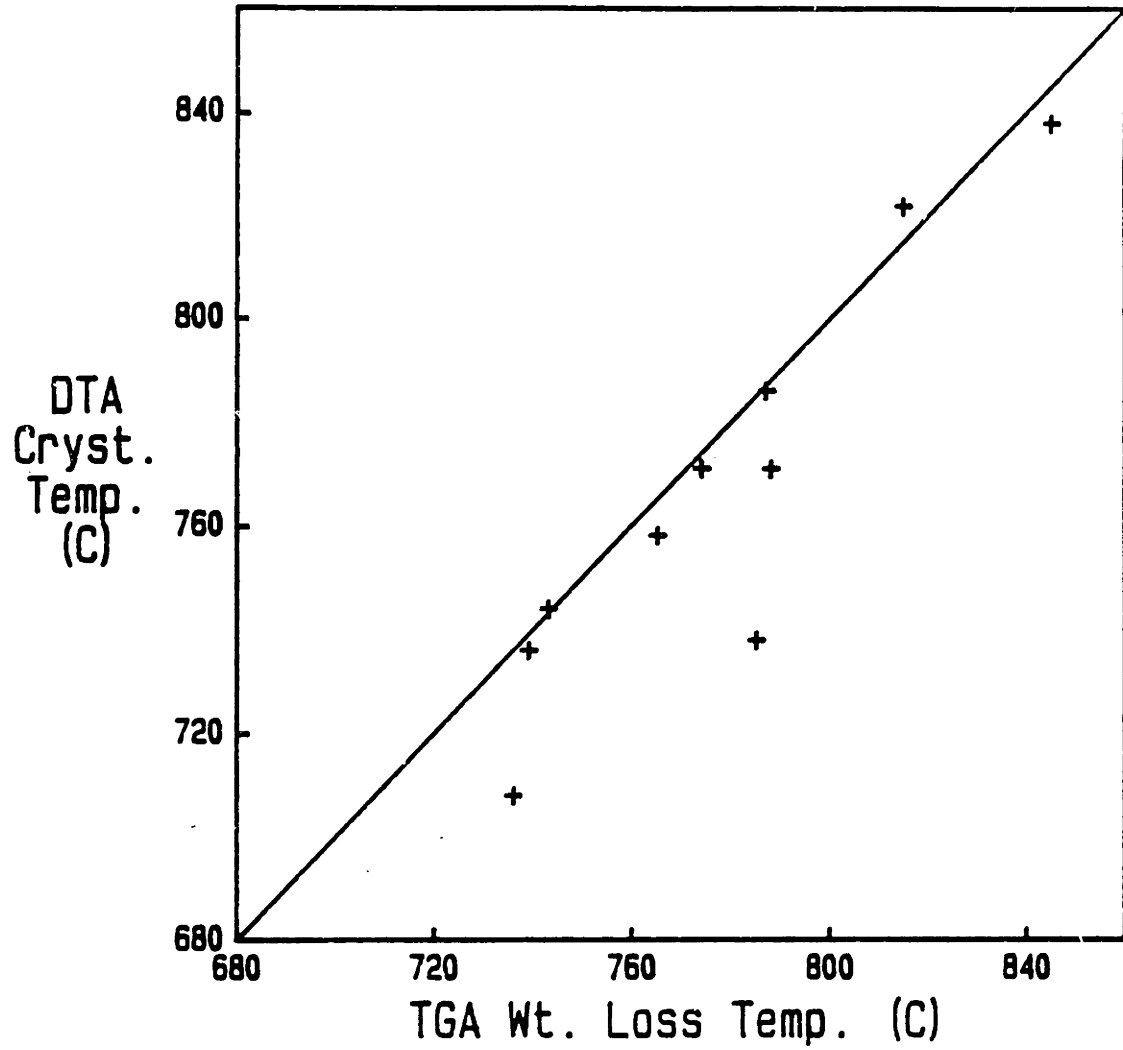


Figure 4.6.13  
Correlation plot of DTA crystallization temperature and high temperature TGA weight loss for all compositions studied. Line represents case of identical crystallization and weight loss temperatures.

powder grains as they crystallize completely. The rejected material fully oxidizes upon exposure to pure oxygen at elevated temperatures. This mechanism also accounts for the slight delay in the crystallization of the nominally pure powder. When fired in nitrogen the increased amount of carbonaceous species remaining in the oxide must be ejected at the crystallization front, making crystallization slower than when the atmosphere is oxidizing.

An additional look at table 4.6.2 shows that the presence of a large amount of the second cation in the powder generally results in an increase in the weight lost due to evaporation and initial condensation (column labeled "initial loss"), and that the temperature at which these processes are complete varies as well. This result is most striking in the samples corresponding to the binary tantalate compositions (those labeled 33 and 50%). This indicates that the second component is either less labile to hydrolysis than is tantala, or contributes to the production of structures that are less condensed than those of the undoped powder. Either of these mechanisms will lead to more residual organics and hydroxyl groups being present in the powder. While there is no hard kinetic data for the hydrolysis and condensation rates for titanium and tantalum, both are very fast. This makes the argument based on the amount of condensation in doped and undoped films the more plausible model of the two.

A second component also tends to reduce the amount of weight that is gained upon oxidation of the amorphous carbon containing phase, and decreases the amount of weight lost during crystallization. Because all of the second components studied are of a lower valence than tantalum, their addition in large quantities should make the amorphous network

less dense, and hence more permeable to oxygen. This will cause less reduction of the components of the network, and hence less weight gain upon reoxidation. In addition, less residual carbon will be trapped within the network to be ejected upon crystallization, or more of the second phase is available for the carbon to be segregated to.

As a final piece of data in this section, DTA and TGA were also run on 9% titania in tantalum powder that had been precipitated after mixing with acetylacetonate. The diketone was added to the alkoxides after the ethanol and before the hydrolysing solution (see procedure above). The ratio of AcAc to tantalum ethoxide was 2, and the degree of hydrolysis before exposure to atmospheric humidity was 3.

TGA results from this powder fired in oxygen were similar in form to the 5% titania run mentioned earlier. The same total weight was lost after firing to 900 C. This time, however, there were two separate weight loss events, one as before due to evaporation of solvent and water, and a second accounting for one third of the total weight loss centered at 375 C. This was followed by a slow gain in weight until the high temperature weight loss occurred at 650 C. DTA results showed complementary features, one endotherm followed by two exotherms centered at 175, 230, and 382 C, respectively, with the crystallization exotherm occurring at 646 C. One should note that this composition crystallized roughly 100 C lower than would have been expected for the powder had it not contained the complexing agent.

The additional feature, the 375 C weight loss was probably due to evaporation or decomposition of the AcAc complex. The exotherm in the DTA is due to its oxidation. The reason for the low crystallization temperature is at this point unknown.

But perhaps the most unusual feature of this particular composition, is that if fired to 1050 C under nitrogen it does not crystallize. The DTA shows the two endotherms that one would expect, and nothing else. A second firing under nitrogen to the same temperature still does not result in crystallization. However, if the atmosphere is then changed to oxygen, two broad exotherms are seen, the first at 440 C, appearing as a shoulder on the larger peak centered at 500 C. No additional analysis was made of this system, nor will I speculate as to the mechanisms involved.

To summarize this section, thermal analysis of nominally pure, as well as doped tantala, indicates that they are quite homogenous. There are three major regimes of behavior: the first is due to evaporation of solvent and adsorbed water, and then additional condensation. The second is where significant oxidation of the network occurs, leading to a gain in weight. The third is crystallization, which is accompanied by the ejection of carbonaceous material at the crystallization front. The addition of a second cation changed the temperature of crystallization, and after crystallization, all two component systems were made up of two phases, as expected.

#### 4.7. Sintering of Pellets

In addition to thermal analysis, the pure tantala gel-derived powder was pressed uniaxially into pellets which were then isostatically pressed to 40 ksi. After pressing, the pellets had a density of 3.62 g/cm<sup>3</sup>, or just over 44 percent of the theoretical density of tantala.

Densification was monitored in a dilatometer as the temperature was raised at a rate of 10 degrees per minute. The calculations below were made based on the change in height of the cylindrical pellet. It was assumed that the ratio of the height to the radius of the pellet did not change during the course of the experiment. This was verified after the completion of the experiment. Shrinkage was initially quite rapid, gradually slowing to reach a maximum density of 63.5% of theoretical at 660 C (fig. 4.7.1). The pellet then began to expand, reaching a local minimum in the density of 59.7% of theoretical at 720 C. The pellet then shrank rapidly and suddenly at 725, decreasing only slowly afterwards to the maximum temperature of the experiment of 1000 C. The final density of the pellet was only 61.3 percent of theoretical density.

SEM of a fracture surface of the fired pellet is shown in figure 4.7.2. The powder looks essentially unchanged after firing to 1000 C, with little necking and sintering having occurred. Therefore, a vast majority of the observed densification must take place as the individual particles themselves shrink.

The initial densification occurs at the same temperatures that a great deal of water and ethanol are being expelled, so additional condensation in addition to the evaporation of adsorbed species is likely to be occurring. As with the supported film results cited earlier, however, the temperature range over which this occurs cannot account for the large change in volume observed at temperatures greater than 400 C. The structure must, therefore, be relaxing significantly at low temperatures.

If we were to consider this relaxation similar to those that occur

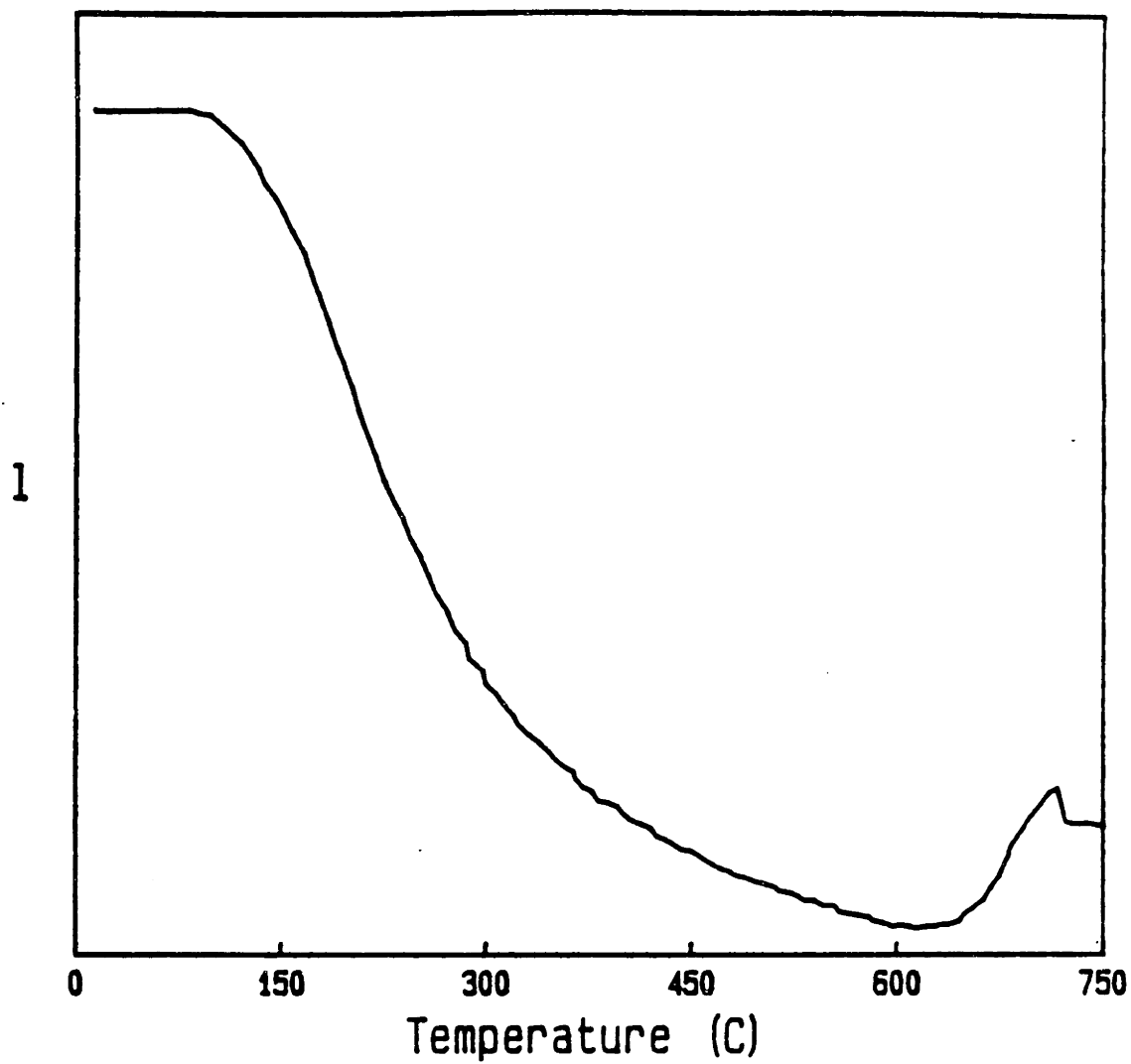


Figure 4.7.1  
Length of pressed pellet as a function of the temperature  
in the dilatometer.

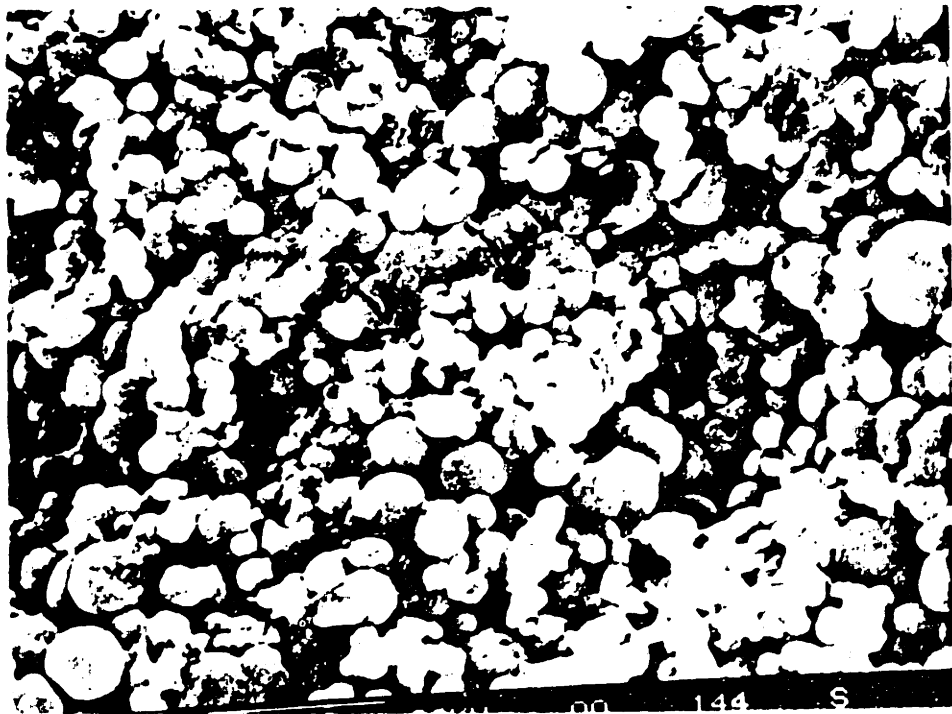
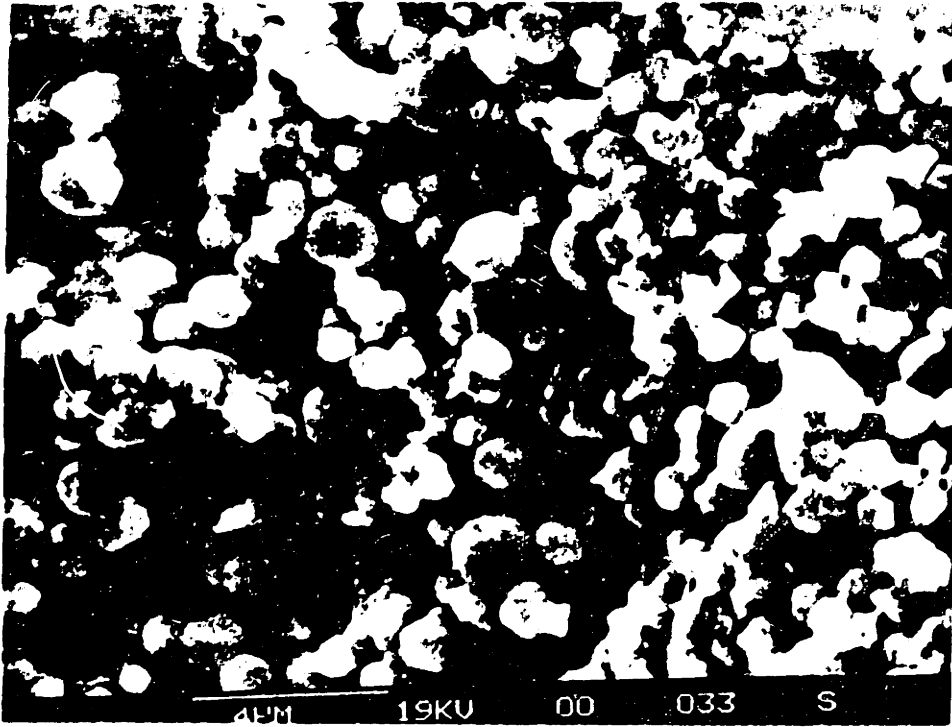


Figure 4.7.2  
Scanning electron micrograph of fracture surface of pressed pellet after being fired to 1000 C in the dilatometer.  
Scale bars are 4 microns



in inorganic and organic glasses in the vicinities of their respective glass transition temperatures, several questions come to mind. First, why might this glass be able to relax at a temperature so far below its supposed glass transition? For the answer to this, we must examine the role of the fictive temperature on relaxation rates. Work of Tool [87] originally suggested that the rate of relaxation at a given temperature should increase if the structure (i.e., fictive temperature) were farther from the equilibrium structure at that temperature due to an increase in the thermodynamic driving force that is the driving force for relaxation. Because these materials are formed at room temperature, where a minimal amount of relaxation can take place, these gel-derived glasses should have fictive temperatures that are quite high, hence inducing a very large driving force for relaxation.

Secondly, where might we expect the glass transition temperature to occur in these systems? As mentioned earlier, using the two-thirds melting point rule-of-thumb we calculate 1400 K, or roughly 1100 C. The 400 C densification, observed here, would indicate a  $T_g$  at roughly one third of the melting point of the crystalline material. Some of this discrepancy might be accounted for if we realize that the two-thirds-rule assumes that the glass is the same composition as the crystal, a blatantly false assumption in this case. Here we have an exceedingly wet glass that is full of carbonaceous species. In silicates, water reduces the glass viscosity. Carbon monoxide and carbon dioxide dissolved in the network may act as plasticizers. On the other hand, small amounts of carbon in the network have been shown to greatly increase the viscosity of silicates [88].

As attractive as these arguments may sound, there is another major

sticking point to explain before structural relaxation can be cited as the cause of the low temperature densification. Experiments described earlier show that, within the accuracy of the measurement tool, the amount of densification is independent of time at temperatures greater than 450 C for periods between 1 and 24 hours. As structural relaxation models generally assume a distribution of relaxation times, they predict the relaxation to slow after the initial burst. While this is observed for temperatures below 450 C, they do not predict the complete stop after an initial relaxation as observed for temperatures above 450 C. It has been shown, however, that films fired for one hour at 600 C begin to crystallize. This may fully explain the lack of densification for films fired at long times at 450 C as well.

The increase in length between 660 and 720 C calculates to an expansion of  $8 \times 10^{-4}$  per degree K, too high to be thermal expansion. As stated earlier, the mechanism responsible for this observation must occur within the individual particles. This temperature corresponds to the region of a large slug of  $\text{CO}_2$  being evolved as observed in the FTIR study. This de-densification, therefore, may be due to bloating of the individual particles during the evolution of carbon monoxide and carbon dioxide within them forming the pores as seen in the TEM work on unconstrained films. It should be stressed that any volatile species which escape from the particles will easily escape from the pressed pellet due to the negligible amount of inter-particle sintering that has occurred. The sharp decrease in length immediately following this bloating must be due either to the crystallization transformation resulting in an increase in density of the skeletal material, crystallization resulting in the ejection of pores from the grains as



The Libraries  
Massachusetts Institute of Technology  
Cambridge, Massachusetts 02139

Institute Archives and Special Collections  
Room 14N-118  
(617) 253-5688

This is the most complete text of the  
thesis available. The following page(s)  
were not included in the copy of the  
thesis deposited in the Institute Archives  
by the author:

*Page 172*

the transformation front approaches the particle boundaries, or to sintering just before crystallization. This first explanation runs contrary to the the literature on densities of amorphous and crystalline tantalum films produced using methods other than solution chemistry, where changes in density upon crystallization are not observed. However, just because it has not been observed for other preparation conditions is no reason to completely rule it out in this case. The suggestion of appreciable sintering should give rise to more intergranular necking than is observed. Finally, the ejection of pore volume filled with carbonaceous species upon crystallization is consistent with the evolution of  $\text{CO}_2$  observed at these temperatures, and therefore seems the best alternative.

The possibility of bloating of the individual particles may solve the problem of the lack of a time dependence in the densification behavior of the films. If the films were to begin to bloat and actually expand, as is suggested by the data, the relaxation behavior of the skeletal material might not be visible. However, one might not expect such a high final density if this were the case. However, this is perhaps the best explanation of the absence of time dependence in the densification behavior.

The contrast between the densification behavior of the films and that of the pellets is striking. The films shrank to 44% of their original volume, leaving perhaps only 8 to 9% of the final volume as closed pores. The weight after firing the films is 17.5% less than it was beforehand, and to calculate the initial film density we must take this into account. The volume after densification ( $V_f$ ) is then related to the volume prior ( $V_i$ ) by

$$V_i = \frac{V_f}{.44} \quad (4.7.1)$$

The weight of the film before and after firing, will be defined as  $W_i$  and  $W_f$ , respectively. Using the TGA data on the undoped powders, these quantities are related by

$$W_i = \frac{W_f}{.825} \quad (4.7.2)$$

The densities before and after firing will be defined using the same subscript scheme. Substituting the relations in equations 4.7.1 and 4.7.2 into an expression for the density of the film before firing, one finds

$$\rho_i = \frac{W_f}{.825} \frac{V_f^{-1}}{0.44} \quad (4.7.3)$$

or the initial density is 53% of the final density. Using the refractive index data for the final density, one calculates an initial density of 49% of theoretical for tantala. As stated earlier, if one calculates an initial density based on the refractive index of crystalline tantala and the value obtained using ellipsometry of the unfired films, one arrives at a value of 41% of the theoretical density. One should realize, however, that the skeletal material is filled with an abundance of organics, water and hydroxyl groups, serving to reduce the average refractive index of the skeleton. This will serve to raise the density as calculated based solely on the refractive index results, making the agreement remarkable.

The pellet, on the other hand, was 44% dense before firing. If we assume a 60% packing density for spherical powder grains, each 49% of theoretical density as is the film, the compact would turn out to be 29% dense, a value much too low. However, using the same packing density as above and the measured density of the compact, we can calculate an estimate of the density of each particle, i.e.,

$$\rho_1 = \frac{0.44}{0.60} = 0.73 \quad (4.7.4)$$

This value (0.73) is much higher than either value calculated for the initial density of the film, even when the weight loss on firing is neglected. Based on these calculations, therefore, we can clearly state that the densities of the unfired films and particles are different.

If we now model the powder compact as a simple cubic arrangement of the unfired spherical grains (other models of the packing have no effect on this particular calculation), and impose the experimentally determined 38% decrease in volume, the sides of the cell will decrease 11% in length, if the shrinkage is equiaxial and no sintering between the spheres occurs. This corresponds to a 38% volume change for the each spherical grain. Translating this shrinkage, combined with the weight loss upon firing as done previously with respect to films, the density after firing is

$$\rho_1 = \frac{W_f}{.825} \frac{V_f^{-1}}{0.62} = 0.75 \quad (4.7.5)$$

or, the final density of each grain is 96% of theoretical.

Conversely, if the final density of the grains were assumed to be the same as that of the fired films, i.e., 92% dense, the initial density of each grain would be 0.75 times this value, or 69% dense. These values are quite close to measurements of actual samples where before and after firing the skeletal densities of the pellets were 65 and 93% of the theoretical density of tantala.

The result of these calculations and measurements is that the pore structure of the films does not resemble that of the individual particles before firing. In other words, the powder grains are not merely a different arrangement of the 2 nm particles that has been suggested for the structure of the films.

If the powder particles as precipitated are indeed more dense than the unfired films, these results run counter to those presented by Brinker [89]. In his analysis, if the species formed in solution are branched structures, the structure resulting from the removal of the solvent is a function of the sticking coefficient. If this coefficient is high, the oligomers in solution will react with one another when they come into close proximity. A low sticking coefficient would result in the oligomers being able to interpenetrate before they react, resulting in a more dense network. The premise on which most of this is based is that there is enough time during the removal of solvent for relatively dense structures to form.

How would this model be applied to tantalum ethoxide? First, in solutions with a low degree of hydrolysis, both hydrolysis and condensation are complete. This would indicate that in the absence of any more water, the species would be completely unreactive towards one another, i.e., they would have a low sticking coefficient. On the other hand, highly hydrolysed solutions might possibly result in species with hydroxyl groups bounding the oligomers. This would make them quite reactive toward each other, and hence a high sticking coefficient. Brinker's model would predict, based on this, that the highly hydrolysed solution should result in less dense structures. Based on only the densification data presented above, this appears not to be the case.

The other major variable in how the films and powders were produced, is the speed of the process. Perhaps the rapidity at which the solvent was removed using the spin coating process is more than enough to compensate for the low degree of hydrolysis for producing open structures.

A summary of this section shows that the individual powder particles densify upon heating, with little sintering occurring between the particles. The initial density of the particles is much higher than the film, and they densify almost completely upon firing. The observation of an expansion of the pellet has been ascribed to the bloating of the individual particles, as has the lack of a time dependence of the densification process.



## Chapter 5. Conclusions

As this work was motivated by the possibility that gel-derived tantala could be used as a dielectric material in VLSI applications, the most important result is that thin tantala films were made using a gel process, and their electronic properties were subsequently characterized. The measured dielectric constant is 30 for films fired to 800 C. The DC leakage current was  $1.45 \times 10^{-5}$  amps/cm<sup>2</sup> at an applied field of 0.7 MV/cm, comparable with values for tantalum oxide produced by thermal oxidation of tantalum metal. The same film has a dielectric loss factor of 0.032. It is possible to increase the dielectric constant of the films to 43 by adding 9% titania. While the dielectric constants and leakage currents make these materials quite attractive for use in integrated circuits, the loss factor makes it impossible to use them in their current form.

Perhaps the second most important conclusion is that based on the densification behavior of films and pellets, their microstructures cannot be the same before firing. Tantala powder granules generated in the described method are more dense prior to firing, contrary to recent proposals.

The oligomers in the coating solution are randomly branched structures, with many small, interconnected rings. Films of good quality are deposited by spin-coating these ethoxide-based solutions onto well-cleaned substrates in a dry environment. The thickness of the film is proportional to the solids content of the solution and inversely proportional to the square root of the spin speed. There was very

little variation in thickness as a function of the radial position on the wafer. Hydrolysis of previously spun on layers is necessary to prevent them from redissolving as subsequent layers are applied.

Electron microscopy reveals the unfired films to have smooth surfaces and uniform structures. Macroscopic (greater than 4 nm) pores are not observed. Upon heating, the films attain a 92% density at 800 C, if they are bonded to a substrate. If this is not the case, the films buckle and sinter into three dimensional networks. Densification is rapid, occurring within the first 15 minutes of the firing step.

Thermal analysis of powders of varying composition showed the crystallization temperature to be dependent on composition. The multicomponent powders made from double alkoxides were chemically quite homogeneous.

## Chapter 6. Future Work

In order to more fully explore this system in terms of its usefulness as a VLSI dielectric, a way must be found to overcome the relatively high dielectric loss factor. There are several possible sources for this affect in the amorphous state prior to crystallization, but the observation that it persists after crystallization indicates that the affect is not due to the skeletal material itself. Possible sources include inclusions, material trapped in pores or adsorbed on pore walls, and even grain boundaries. Some work on anorthite and cordierite indicates that residual carbonaceous species can be reduced by washing the still porous unfired powders in hydrogen peroxide. While the general idea may be useful to pursue, hydrogen peroxide itself is not the solution since it has been reported to attack tantalum. Another strong oxidizer may prove better. Another solution may also lie in a different firing schedule, or perhaps a different firing atmosphere.

The films described in this work may still contain some porosity. The magnitude of the porosity must be established by some direct means, not calculating a value based on the refractive index. If it is found that there is residual porosity, we must discover whether it is possible to sinter thin films of these compositions to full density before crystallization prevents further densification. The data presented on the prevention of crystallization in systems containing acetylacetonate in neutral atmospheres is intriguing, and may point to a possible solution. More work should be done on complexing agent-containing systems to determine the causes of the enhanced relaxation processes in

silicates, as well as the inhibition of crystallization in this system.

In more general terms, more work should go into finding out the differences between the structures of powders and films. It is clear from this study that the two are different upon formation. Because very thin films are difficult to study, a way should be found to correlate the behavior of films to that of powders, so that the responses of one may be predicted from the from measurements of the other. A better solution is the investigation of different measurement techniques that will adequately describe the structure and properties of thin films.

Chemical homogeneity on a nano-scale is one of the much touted benefits of the sol-gel process for making ceramics and ceramic precursors. However, up to this point we are able to point only to the indirect evidence of crystallization behavior during thermal analysis. Are gel-derived materials more homogenous than those produced using alternate methods? If they are, does the added homogeneity buy anything? How does processing effect homogeneity? Are double alkoxides indeed capable of the ultimately homogeneous body? Do double alkoxides stay together during hydrolysis and condensation? Again, a more direct measurement of the spacial distribution of elements in very thin films and powders must be investigated (perhaps Raman spectroscopy and neutron scattering) and used. Then correlations must be made between a given property and the degree of homogeneity. Only then will we know the answers to these questions.

## List of References

- 1 Lin, Y.C., Wellinghoff, S.T., in Electronic Packaging Material Science, edited by E.A. Geiss, K.-N. Tu and D.R. Uhlmann (Materials Research Society, Pittsburgh, 1895) 97.
- 2 JANAF Theromchemical Tables
- 3 Leslie, J.D., Knorr, K., J. Electrochem. Soc., 121 (1974) 263.
- 4 Charlesby, A., Pooling, J.J., Proc. Roy. Soc., A227 (1955) 434.
- 5 Kaplan, E., Balog, M., Frohman-Bentchkowsky, D., J. Electrochem. Soc., 123 (1976) 1570.
- 6 Knausenberger, W.H., Tauber, R.N., J. Electrochem. Soc., 120 (1973) 827.
- 7 Torrisi, A.F., J. Electrochem. Soc., 102 (1955) 176.
- 8 Vermilyea, D.A., Acta Met., 1 (1953) 282.
- 9 Samsonov, G.V., Plenum Press, N.Y., 1982.
- 10 Stephenson, N.C., Roth, R.S., Acta Cryst., B27 (1971) 1037.
- 11 Roth, R.S., Waring, J.L., Brower, W.S., J. Res. Nat. Bur. Stand., A, 74 (1970) 483.
- 12 McHale, A.E., Tuller, H.L., J. Am. Cer. Soc., 68 (1985) 646.
- 13 McHale, A.E., Tuller, H.L., J. Am. Cer. Soc., 68 (1985) 651.
- 14 Wilcox, P., J. Vacuum Sci. and Technol., 9 (1972) 74.
- 15 Ling, H.C., Yan, M.F., Rhodes, W.W., in Science of Ceramic Chemical Processing, edited by L.L. Hensch and D.R. Ulrich (Wiley Interscience, NY, 1986) 285.
- 16 Oehrlein, G.S., d'Heurle, F.M., Reisman A., J. Appl. Phys., 55 (1984) 3715.
- 17 Gerstenberg, D., J. Electrochem. Soc., 113 (1966) 1542.
- 18 Wang, C.C, Zaininger, K.H., Duffy, M.T., RCA Review, Dec. (1980) 728.
- 19 Povlovic, A.S., J. Chem. Phys., 40 (1964) 951.
- 20 Oehrlein, G.S., Reismann, A., J. Appl. Phys., 54 (1983) 6502.
- 21 Sasaki, Y., J. Phys. Chem. Solids, 13 (1960) 177.
- 22 Vermilyea, D.A., J. Electrochem. Soc., 102 (1955) 655.
- 23 Vermilyea, D.A., J. Electrochem. Soc., 104 (1957) 485.
- 24 Kimura, S., Nishioka, Y., Shintani, A., Mukai, K., J. Electrochem. Soc., 130 (1983) 2414.
- 25 Vermilyea, D.A., Acta Met., 6 (1958) 166.
- 26 Cathcart, J.V., Bakish, R., Norton, D.R., J. Electrochem. Soc., 107 (1960) 668.
- 27 Val, C., Croset, M., Velasco, G., in Chemical Abstracts, 81:55492q.
- 28 Bradley, D.C., Holloway, H., Can. J. Chem., 39 (1961) 1818.
- 29 Bradley, D.C., Wardlaw, W., Whitley, A., J. Chem. Soc., 1955, 726.
- 30 Bradley, D.C., Wardlaw, W., Whitley, A., J. Chem. Soc., 1956, 1139.
- 31 Bradley, D.C., Chakravati, B.N., Chaterjee, A.K., Wardlaw, W., Whitley, A., J. Chem. Soc., 1958, 99.
- 32 Bradley, D.C., Holloway, H., Can. J. Chem., 40 (1962) 62.
- 33 Bradley, D.C., Wardlaw, W., Whitley, A., J. Chem. Soc., 1956, 5.
- 34 Bradley, D.C., Mehrortra, R.C., Gaur, D.P., Metal Alkoxides, (Academic Press, London, 1978).
- 35 Bradley, D.C., Holloway, C.E., J. Chem. Soc. (A), 1968, 219.
- 36 Pfalzgraf, L.G., Reiss, J.G., Bull. Soc. Chim. France, 1968, 4348.
- 37 Reiss, J.G., Pfalzgraf, L.G., Bull. Soc. Chim. France, 1968, 2401.
- 38 Bradley, D.C., Holloway, C.E., J. Chem. Soc. (A), 1968, 1316.

- 39 Mehrotra, R.C., Kapoor, P.N., J. Less Common Metals, 7 (1964) 453.
- 40 Sommer, L.H., et. al. (7 others), J. Am. Chem. Soc., 83 (1961) 2210.
- 41 Schmidt, H., Scholze, H., Proc. NATO Summer School on Glass, Tenerife, 1984.
- 42 Pohl, E.R., Osterholz, F.D., Polymer Preprints, March-April (1984) 200.
- 43 Aelion, R., Loebel, A., Eirich, F., J. Am. Chem. Soc., 82 (1950) 5705.
- 44 Zelinski, B.J.J., Uhlmann, D.R., J. Phys. Chem. Solids., 45 (1985) 1069.
- 45 Doughty, D., private communication.
- 46 Sakka, S., Kamiya, K., J. Non-Cryst. Solids, 48 (1982) 31.
- 47 Zelinski, B.J.J., Fabes, B.D., Uhlmann, D.R., to appear in J. Non-Cryst. Solids.
- 48 Schmidt, H., private communication.
- 49 Florey, P.J., Principles of Polymer Chemistry, Cornell University Press, Ithaca, 1953.
- 50 Schroeder, H., Physics of Thin Films, 5 (1969) 87.
- 51 Brinker, C.J., Harrington, M.S., Solar Energy Materials, 5 (1981) 159.
- 52 Yoldas, B.E., Okeefe, T.W., Appl. Opt., 18 (1979) 3133.
- 53 Phillips, R.W., Dodds, J.W., Appl. Optics, 20 (1981) 40.
- 54 Yoldas, B.E., Appl. Opt., 21 (1982) 2980.
- 55 McGillis, D.A., in VLSI Technology, edited by S.M. Sze (McGraw-Hill, NY, 1983) 267.
- 56 Scherer, G.W., J. Non-Cryst. Solids, 87 (1986) 199.
- 57 Scherer, G.W., to appear in J. Non-Cryst. Solids.
- 58 Yoldas, B.E., J. Non-Cryst. Solids, 38+39 (1980) 81.
- 59 Yoldas, B.E., J. Mat. Sci., 14 (1979) 1843.
- 60 Zarzycki, J., Prassas, M., Phalippou, J., J. Mater. Sci., 17 (1982) 3371.
- 61 Hensch, L.L., in Science of Ceramic Chemical Processing, edited by L.L. Hensch and D.R. Ulrich (Wiley Interscience, NY, 1986) 52.
- 62 Hensch, L.L., Orcel, G., Nogues, J.L., in Better Ceramics Through Chemistry II, eds. C.J. Brinker, D.E. Clark, and D.R. Ulrich (Materials Research Society, Pittsburgh, 1986) 35.
- 63 Yoldas, B.E., Partlow, D.P., Appl. Opt., 23 (1984) 1418.
- 64 Singh, S., private communication.
- 65 Meiling, G., private communication.
- 66 Gulati, S.T., Hagy, H.E., J. Am. Cer. Soc., 61 (1978) 263.
- 67 Gulati, S.T., Hagy, H.E., J. Am. Cer. Soc., 61 (1978) 260.
- 68 Yamane, M., Aso, S., Okano, S., Sakaino, T., J. Mat. Sci., 14 (1979) 607.
- 69 Prassas, M., in Ultrastructure Processing of Ceramics, Glasses and Composites, eds. L.L. Hensch and D.R. Ulrich (Wiley Interscience, NY, 1984) 128.
- 70 Mukherjee, S.P., Lowdermilk, W.H., J. Non-Cryst. Solids, 48 (1982) 177.
- 71 Mukherjee, S.P., Debsikdar, J.C., Bull. Am. Cer. Soc., 62 (1983) 413.
- 72 Brinker, C.J., Mukherjee, S.P., J. Mater. Sci., 16 (1981) 1980.
- 73 Kondo, S., Fujiwara, F., J. Colloid Interface Sci., 53 (1976) 421.

- 74 Kingery, W.D., Bowen, H.K., Uhlmann, D.R., Introduction to Ceramics, (John Wiley and Sons, NY, 1976).
- 75 Uhlmann, D.R., Zelinski, B.J.J., Silverman, L.A., Warner, S.B., Fabes, B.D., Doyle, W.F., Science of Ceramic Chemical Processing, edited by L.L. Hensch and D.R. Ulrich (Wiley Interscience, NY, 1986) 173.
- 76 Scherer, G.W., J. Am. Cer. Soc., 60 (1977) 243.
- 77 Carman, L.A., Pantano, C.G., Science of Ceramic Chemical Processing, edited by L.L. Hensch and D.R. Ulrich (Wiley Interscience, NY, 1986) 187.
- 78 Fabes, B.D., Doyle, W.F., Silverman, L.A., Zelinski, B.J.J., Uhlmann, D.R., in Science of Ceramic Chemical Processing, edited by L.L. Hensch and D.R. Ulrich (Wiley Interscience, NY, 1986) 217.
- 79 Fabes, B.D., Doyle, W.F., Zelinski, B.J.J., Silverman, L.A., Uhlmann, D.R., J. Non-Cryst. Solids, 82 (1986) 349.
- 80 Brinker, C.J., Mukherjee, S.P., Thin Solid Films, 77 (1981) 141.
- 81 Yoldas, B.E., Partlow, D.P., Am. Cer. Soc. Bull., 59 (1980) 640.
- 82 Nicollian, E.H., Brews, J.R., MOS (Metal Oxide Semiconductor) Physics and Technology (Wiley Interscience, NY, 1982).
- 83 LaCourse, W.C., Kim, S., in Science of Ceramic Chemical Processing, edited by L.L. Hensch and D.R. Ulrich (Wiley Interscience, NY, 1986) 304.
- 84 Worthing, F.L., J. Electrochem. Soc., 115 (1968) 88.
- 85 Welti, D., Infrared Vapour Spectra (Haydon and Son, NY, 1970).
- 86 Knozinger, H., in The Chemistry of the Hydroxyl Group, edited by S. Patai (John Wiley and Sons, NY, 1971) 641.
- 87 Tool, A.Q., J. Res. Nat. Bur. Stand., 34 (1945) 199.
- 88 Elmer, T.H., Meissner, H.E., J. Am. Cer. Soc., 59 (1976) 206.
- 89 Brinker, C.J., to appear in The Design, Activation and Transformation of Organometallics into Common and Exotic Materials, NATO Proceedings, Cap d'Agde, France, September 1986.

## Biographical data

Lee Silverman was born on January 6, 1959, in Washington, D.C. He grew up in the suburbs of Washington, Boston, and Philadelphia. He attended MIT, receiving an S.B. in Materials Science and Engineering in February of 1981. His undergraduate thesis was titled "The Formation and Characterization of Nickel Sulfide Stones in Glass", and was done under the supervision of Prof. D.R. Uhlmann. He then moved to Corning N.Y., to work for Corning Glass Works on the development of processes for the manufacture of optical waveguides for long distance telecommunication. After working for two and a half years, he returned to MIT in September 1983, to work for Prof. Uhlmann on materials from gels.